UNIVERSITY OF Southampton

Preparation and Characterisation of an Aluminium-Conductive Polymer Battery in a Chloroaluminate Ionic Liquid for Future Energy Storage

By
Theresa Schoetz

A thesis submitted for the
Doctor of Philosophy

University of Southampton
Faculty of Engineering and Physical Sciences
Energy Technology

Southampton, 26 September 2019

UNIVERSITY OF Southampton

Research Thesis: Declaration of Authorship

Print name:	Theresa Schoetz

Title of thesis:	Preparation and Characterisation of an Aluminium-Conductive Polymer Battery in a Chloroaluminate Ionic Liquid for Future Energy Storage

I declare that this thesis and the work presented in it is my own and has been generated by me as the result of my own original research.

I confirm that:

This work was done wholly or mainly while in candidature for a research degree at this University;

Where any part of this thesis has previously been submitted for a degree or any other qualification at this University or any other institution, this has been clearly stated;

Where I have consulted the published work of others, this is always clearly attributed;

Where I have quoted from the work of others, the source is always given. With the exception of such quotations, this thesis is entirely my own work;

I have acknowledged all main sources of help;

Where the thesis is based on work done by myself jointly with others, I have made clear exactly what was done by others and what I have contributed myself;

Either none of this work has been published before submission, or parts of this work have been published as:

• T. Schoetz, M. Kurniawan, M. Stich, R. Peipmann, I. Efimov, A. Ispas, A. Bund, C. Ponce de Leon and M. Ueda (2018) Understanding the charge storage mechanism of conductive polymers as hybrid battery-capacitor material in ionic liquids by *in-situ* atomic force microscopy and electrochemical quartz crystal microbalance. *Journal of Materials Chemistry A* 6, 17787-17799.

• T. Schoetz, C. Ponce De Leon, A. Bund and M. Ueda (2018) Electro-polymerisation and characterisation of PEDOT in Lewis basic, neutral and acidic EMImCl-$AlCl_3$ ionic liquid. *Electrochimica Acta* 263, 176-183.

• T. Schoetz, C. Ponce De Leon, A. Bund and M. Ueda (2018) Electro-polymerisation of 3,4-ethylenedioxythiophene on reticulated vitreous carbon in imidazolium-based chloroaluminate ionic liquid as energy storage material. *Electrochemistry Communications* 89, 52-56.

• T. Schoetz, C. Ponce De Leon, A. Bund and M. Ueda (2017) Preparation and characterization of a rechargeable battery based on poly-(3,4-ethylenedioxythiophene) and aluminum in ionic liquids. *Journal of Solid State Electrochemistry* 21, 3237–3246.

• T. Schoetz, C. Ponce De Leon, A. Bund and M. Ueda (2017) State of the art of rechargeable aluminium batteries in non-aqueous systems: A perspective. *Journal of the Electrochemical Society* 164, A3499-A3502.

Signature:		Date:	26/09/2019

Acknowledgement

When I look back, this work started with an idea and a sketch on a piece of paper at the Hokkaido University, Japan. I am grateful for Professor Mikito Ueda, who enabled the early stage proof-of-concept study of the aluminium-conductive polymer battery and who was a valuable project partner throughout the whole time.

My mentor and supervisor Dr Carlos Ponce de Leon saw the potential in this project, always shared my visions and values as well as empowered my PhD candidature at the University of Southampton. I want to take the opportunity to thank him for all his hard work and help.

I appreciate the project funding provided by the International Consortium of Nanotechnologies of the Lloyd's Register Foundation (LRF-ICoN) and the Centre for Doctoral Training in Sustainable Infrastructure Systems (CDT-SIS).

The Electrochemistry and Electroplating group with Professor Andreas Bund, Dr Adriana Ispas and Dr Ralf Peipmann from Technische Universität Ilmenau, Germany supported this project unwaveringly as a collaborator and realised a six-month internship in their laboratories. Particularly helpful during this time was the accomplishment of the challenging in-operando atomic force microscopy and electrochemical quartz crystal microbalance measurements.

Furthermore, my colleagues Ben Craig and Oi Man Leung from the University of Southampton, Dr Michael Stich, Mario Kurniawan, René Böttcher and Dr Svetlozar Ivanov from Technische Universität Ilmenau contributed selflessly to the realisation of this work with a sense of commitment and perfection rarely found in research. I also had a great pleasure performing scanning electron microscopy measurements with Dr Rachel McKerracher and Dr Richard Pearce from the University of Southampton. I want to thank Dr Igor Efimov from the University of Leicester who taught me many aspects about electrochemistry and battery testing. Dr John Low from the University of Warwick, Professor Themis Prodromakis, Dr Denis Kramer and Dr Dmitry Bavykin from the University of Southampton provided profound guidance.

Last but foremost, I thank Dr Cornel-Constantin Lalau, who supported my work, and never stopped believing in me and my scientific ideas. Thank you.

Abstract

The aluminium battery is one of the very promising alternative battery chemistries for future energy storage, because of its sustainability, its performance due to the three electron redox reaction, and its high specific capacity due to the light weight of aluminium. The current approach uses aluminium anodes and graphite cathodes in non-aqueous electrolytes. Even though scientific progress has been made with this approach, the cathode reaction continues to limit the energy storage performance for future aluminium batteries that demand both high specific energy and high specific power. A new approach is the combination of aluminium anodes with conductive polymer cathodes. The novelty of these cathodes is that they behave both as a battery and as a capacitor, giving it more storage capability than previous aluminium battery systems.

In this work, the current role of alternative battery systems, beyond lithium-ion, is discussed followed by a proof-of-concept study of an aluminium-conductive polymer battery with ionic liquid electrolyte, wherein the conductive polymer poly(3,4-ethylenedioxythiophene) (PEDOT) was synthesised electrochemically in aqueous solution. This study demonstrated the feasibility of an aluminium-PEDOT battery with preliminary performance (specific energy and power) in the range of state-of-the-art rechargeable batteries but shows significant limitations regarding the conductive polymer electrode stability. Therefore, the key challenge of this work was the synthesis of stable and efficient conductive polymers by electropolymerisation in ionic liquids, which was linked with studies of the polymer's mechanistic behaviour depending on its state of charge. Thereby, the electrochemical and nanomechanical behaviour, as well as the polymer morphology, were investigated by cyclic voltammetry, electrochemical impedance spectroscopy, quartz crystal microbalance measurements, scanning electron and in-operando atomic force microscopy. A further research pillar was the reproduction of polymer properties from two-dimensional to three-dimensional substrates, which increase the active surface area per unit cathode volume, via electropolymerisation. The work was brought to its conclusion by performance testing of the aluminium-conductive polymer with the improved three-dimensional polymer cathodes. The final battery performance reached a substantial improvement in reversibility and stability, showing direct and meaningful progress, and proving the relevance of aluminium batteries for future energy storage.

Symbols and Abbreviations

AFM	Atomic force microscopy
Ag|AgCl	Silver-silver chloride reference electrode
Al|Al(III)	Aluminium reference electrode; trivalent aluminium compound
$Al_2Cl_7^-$	Heptachlorodialuminate anion
$AlCl_3$	Aluminium chloride
$AlCl_4^-$	Tetrachloroaluminate anion
AT	Cut of the quartz crystal
CC	Constant current
CCCV	Constant current-constant voltage
Cd-Ni	Cadmium-nickel battery
CE	Counter electrode
CV	Cyclic voltammetry
DMC	Dimethyl carbonate
DPA	Differential pulse amperometry
EC-AFM	Electrochemical atomic force microscopy
EDOT	3,4-Ethylenedioxythiophene
EEC	Electrode-electrolyte composite
EIS	Electrochemical Impedance spectroscopy
$EMIm^+$	1-Ethyl-3-methylimidazolium cation
EMImCl	1-Ethyl-3-methylimidazolium chloride
EMImCl-$AlCl_3$	1-Ethyl-3-methylimidazolium chloride aluminium chloride ionic liquid
EQCM	Electrochemical quartz crystal microbalance
ESM	Energy storage material
IL	Ionic liquid
Li-ion	Lithium-ion battery
LSV	Linear sweep voltammetry
Ni-metal-hydride	Nickel-metal-hydride battery
OCP	Open circuit potential
PAn	Polyaniline
Pb-acid	Lead-acid battery

PEDOT	Poly(3,4-ethylenedioxythiophene)
PPy	Polypyrrole
PTFE	Polytetrafluoroethylene
RE	Reference electrode
RNPV	Reverse normal pulse voltammetry
RVC	Reticulated vitreous carbon
SEM	Scanning electron microscopy
SHE	Standard hydrogen electrode
V-redox-flow	Vanadium-redox-flow battery
VC	Vitreous carbon
WE	Working electrode
X^-	Anion species

A	Area
b	Sauerbrey correction factor
C, Q	Capacity
c	Concentration
E	Electrode potential
E_0	Standard potential
E_{spec}	Specific energy
F	Faraday constant (96485 As mol^{-1})
f	Resonance frequency
f_0	Resonance frequency of the unloaded quartz
f_s	Resonance frequency of the quartz in fluid
G	Shear modulus
G*	Complex shear modulus
G’	Storage modulus, real part of the shear modulus
G“	Loss modulus, imaginary part of the shear modulus
h	Film thickness
h_f	Film thickness of the polymer
h_{fSB}	Film thickness of the polymer, calculated using the Sauerbrey equation
h_{rl}	Film thickness for a rigid layer

I	Electric current
i	Imaginary unit ($i = \sqrt{-1}$)
Im	Imaginary part
Im(Z)	Imaginary part impedance
j	Current density
K^2	Electromechanical coupling factor for the quartz (≈0,00774)
L	Inductivity
m_i	Mass of component i
M	Coupling factor
M_i	Molar mass of component i
N	Amount of $AlCl_3$
n	Amount of substance
N_h	Fundamental frequency
P_{spec}	Specific energy
Q_i	Capacity, Transferred amount of charges of component i
Q_{spec}	Specific capacity
R	Resistance
Re	Real part
Re(Z)	Real part impedance
T	Temperature, absolute
t	Time
V	Volume
v	Scan rate
w	Damping
w_0	Damping of the unloaded quartz
w_s	Damping of the quartz in fluid
X_l	Reactance of the electrolyte
x	Inter polymer chain distance
z	Number of transferred electrons
Z	Impedance, Phase
Z_f, Z_s	Surface impedance
Z_{fSB}^{m}	Mechanical impedance of the electrolyte, calculated by Sauerbrey

Z_l	Impedance of films in electrolyte
Z_Q, Z_q	Characteristic impedance of the quartz (884880.6 g $cm^{-2}s^{-1}$)
Z_{tr}	Impedance of films with trapped electrolyte
α	Degree of anion insertion
Δf	(Resonance-)frequency change
Δw	Damping change
η_l	Kinematic viscosity of the ionic liquid
κ	Electric conductivity
μ_Q, μ_q	Shear modulus of the quartz ($2{,}957 \cdot 10^{11}$ g cms^{-2})
ρ_i	Density of component i
ρ_f	Density of the polymer film ($\rho_f \approx \rho_{PEDOT} \approx \rho_{EDOT}$; 1,334 g cm^{-3})
ρ_l	Density of the electrolyte (1.2985 g cm^{-3})
ρ_Q, ρ_q	Density of the quartz (2,648 g cm^{-3})
ρ_{rl}	Density for a rigid layer
χ	Molar ratio
ω	Radial frequency

Table of Contents

Acknowledgement ..... **I**

Abstract ..... **III**

Symbols and Abbreviations ..... **IV**

1 Introduction and Broader Context **1**

1.1 State-of-the-Art and Perspectives of Aluminium-Based Batteries 3

1.1.1 Conventional Aluminium-Based Batteries with Aqueous Electrolyte 3

1.1.2 Charge Storage Materials in Rechargeable Aluminium Batteries 4

1.1.3 Battery Systems Based on Aluminium and a Conductive Polymer 5

2 Research Aim and Idea **8**

2.1 The Aluminium-Conductive Polymer Battery Concept 8

3 Theoretical Background **11**

3.1 Conductive Polymers 11

3.1.1 Hybrid Battery-Capacitor Concept 13

3.2 Ionic Liquids 15

3.2.1 Aluminium Deposition in Chloroaluminate Ionic Liquid 16

4 Experimental Methods **18**

4.1 Ionic Liquid Preparation 18

4.2 Conductive Polymer Synthesis 20

4.2.1 Polymerisation in Aqueous Solution 20

4.2.2 Polymerisation in Chloroaluminate Ionic Liquid 21

4.2.2.1 Polymerisation on Planar Vitreous Carbon 21

4.2.2.2 Polymerisation on Reticulated Vitreous Carbon 21

4.3 Electrode Characterisations 21

4.3.1 Conductive Polymer Electrode Characterisation 22

4.3.1.1 Cyclic Voltammetry 22

4.3.1.2 Electrochemical Quartz Crystal Microbalance Measurements 22
4.3.1.2.1 Determination of the Shear Modulus 24
4.3.1.3 Electrochemical Impedance Spectroscopy 27
4.3.1.4 Scanning Electron Microscopy 27
4.3.1.5 In-Operando Atomic Force Microscopy 28
4.3.2 Aluminium Electrode Characterisation 29
4.3.2.1 Cyclic Voltammetry 29
4.3.2.2 Scanning Electron Microscopy 30
4.3.2.3 In-Operando Atomic Force Microscopy 30
4.4 Evaluation of the Proof-of-Concept Study 30
4.5 Battery Design and Characterisation 31
4.5.1 Battery Charging and Discharging 33
4.5.2 Determination of the Battery Characteristic Values 33
4.5.2.1 Considered Active Mass 34
5 Results and Discussion 36
5.1 Proof-of-Concept 36
5.1.1 Preliminary Battery Evaluation 36
5.2 Improvements of the Conductive Polymer Electrode 38
5.2.1 Synthesis of PEDOT Electrodes in Ionic Liquid 38
5.2.1.1 Polymerisation in Lewis Acidic Ionic Liquid 39
5.2.1.2 Polymerisation in Lewis Basic Ionic Liquid 41
5.2.1.3 Polymerisation in Lewis Neutral Ionic Liquid 42
5.2.2 Synthesis of PEDOT on 3D Substrates in Ionic Liquid 44
5.3 Electrode Characterisation in Ionic Liquid 48
5.3.1 Characterisation of PEDOT in Ionic Liquid 48
5.3.1.1 Formation of Anion Insertion and Removal Sites 51

5.3.1.2 Stability of PEDOT in Ionic Liquid 54
5.3.1.3 Comparison of PEDOT on 2D and 3D Vitreous Carbon 55
5.3.1.4 Characteristics of PEDOT Depending on the State of Charge 56
5.3.1.4.1 Viscoelastic Changes 57
5.3.1.4.2 Morphological Changes 62
5.3.1.4.3 Impedance Response 65
5.3.1.4.3.1 Discussion of the Nyquist Plot 65
5.3.1.4.3.2 Discussion of the Bode Plot 66
5.3.1.4.4 Suggested Model of PEDOT Depending on the State of Charge 68
5.3.2 Aluminium Deposition and Dissolution 71
5.3.2.1 Influence of Lewis Acidity on Aluminium Deposition 73
5.4 Determination of Battery Characteristics 76
5.4.1 Charge Rate 78
5.4.2 Discharge Rate 79
5.4.3 Cycle Stability 80
5.4.4 Battery Characteristic Values 83
5.5 Next Step for Performance Improvement 86
6 Conclusions 88
7 Perspective and Trends in Battery Research 92
8 Appendix 98
8.1 Script of the Algorithm for the Calculation of the Shear Modulus 98
8.2 In-Operando Atomic Force Microscopy Movie of PEDOT 111
References IX
List of Figures XIX
List of Tables XXV

1 Introduction and Broader Context

In this chapter paragraphs, figures and tables were published and reproduced with permission of Springer Berlin Heidelberg [1] and The Electrochemical Society [2].

Nowadays, on the one hand, energy storage devices require sustainable, safe and low-cost materials. On the other hand, battery materials need to provide performance, quantified by specific energy and power. Lithium-based batteries have a monopoly on specific energy performance (~200 Wh kg^{-1} and ~300 W kg^{-1} [3]). Advances in lithium-ion battery performance have contributed to their vast application in portable energy storage technologies. Improvements were reached by reducing the geometric dimensions of active materials, the formation of composite materials, doping and functionalisation, change of the particle morphology, the formation of coatings or shells around the active materials and modifications of the electrolyte [4–8]. Particular future enhancements and changes to lithium-based batteries are promised by lithium-sulphur and lithium-air batteries. Lithium-sulphur batteries replace the cobalt, manganese, nickel or aluminium components of lithium-ion batteries with light-weight and cheap sulphur and the intercalation electrode - the graphite - with metallic lithium, improving the ratio of weight and performance. It is assumed that lithium-sulphur batteries might reach a specific energy of 500 Wh kg^{-1}. Lithium-air batteries have a theoretical specific energy up to 1000 Wh kg^{-1}. However, next to battery performance, one factor is becoming a more important issue these days: sustainability. Flammability, difficult recycling and limited availability of lithium and other constituents such as nickel and cobalt raise severe issues in terms of safety, cost-effectiveness and future sustainability (Figure 1). Therefore, the focus needs to be on moving beyond lithium-based energy storage technologies and future-viable materials. [1,2]

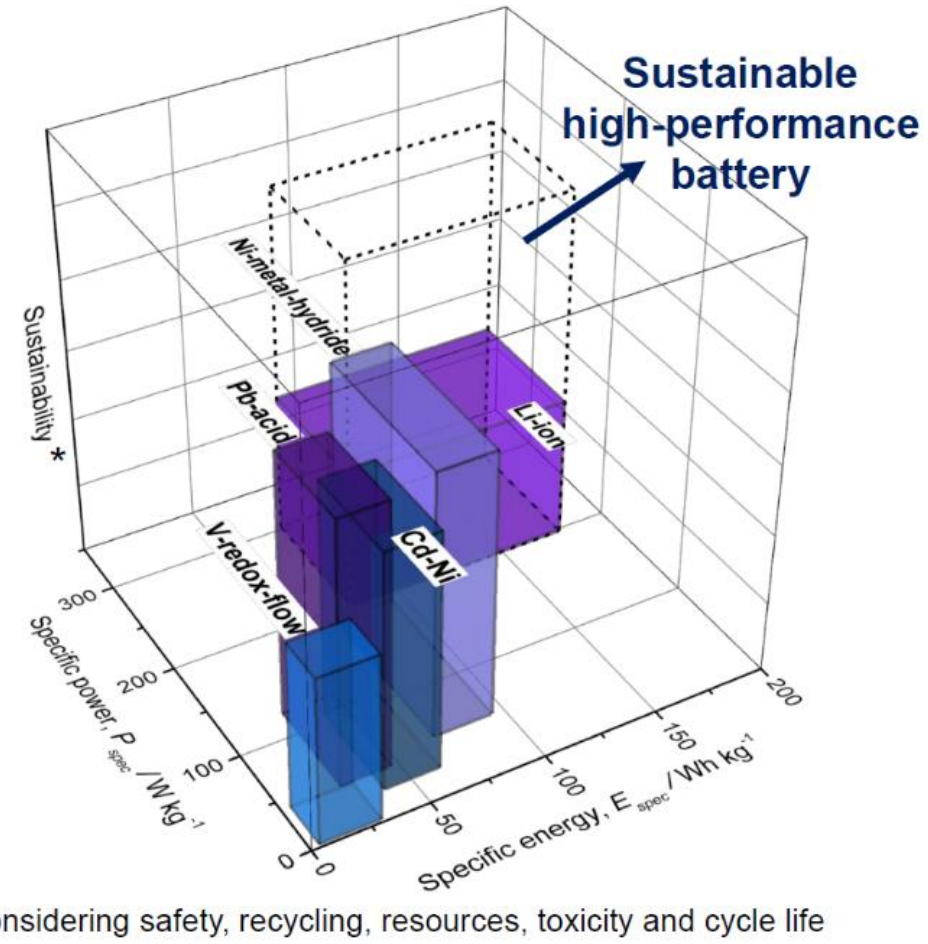

Figure 1: Specific power and energy of state-of-the-art rechargeable batteries vanadium-redox-flow (V-redox-flow), lead-acid (Pb-acid), cadmium-nickel (Cd-Ni), nickel-metal-hydride (Ni-metal-hydride) and lithium-ion (Li-ion) batteries in relation to sustainability [3]. [2]

A new approach to balance battery performance and sustainability has been taken by the development of alternative batteries based on highly abundant, highly recyclable, non-toxic, cost-effective, light-weight and safe electrode materials such as aluminium, magnesium or sodium. Less attention has been directed to the use of light-weight aluminium-based batteries in non-aqueous systems, even though aluminium has lower cost, is more abundant and is safer than lithium. Furthermore, its specific capacity of 2980 mAh g^{-1} and volumetric capacity of 8040 mAh cm^{-3} are similar to lithium [2,9]. The number of studies on rechargeable aluminium-based batteries in non-aqueous systems has increased 10-fold in the last decade. Therefore, it seems appropriate and timely to review the state-of-the-art and the implementation of novel ideas and approaches made for rechargeable high-performance aluminium-based batteries and reflect on the perspectives, challenges and limitations that these relatively new systems face. [2]

1.1 State-of-the-Art and Perspectives of Aluminium-Based Batteries

A novel aluminium battery system was described in 1988 with aluminium and graphite as the negative and positive electrodes respectively, in a Lewis acidic chloroaluminate ionic liquid at room temperature [2,10]. Chloroaluminate anions intercalated into the graphite electrode reaching 64 Wh kg^{-1} specific energy at 1.7 V discharge potential over 150 cycles and 80-90 % coulombic efficiency [10]. The same idea was taken up several years later by various research groups [9,11–13] using different oxides, sulphides and zeolites as intercalation electrodes [14–21]. More recently the introduction of conductive polymers as the positive electrode represents a further development with great potential for a rechargeable aluminium hybrid battery-capacitor energy storage system [1,22]. [2]

1.1.1 Conventional Aluminium-Based Batteries with Aqueous Electrolyte

A number of primary battery compositions like Al-MnO_2, Al-AgO, Al-H_2O_2, Al-S, Al-FeCN and Al-NiOOH [23] in aqueous electrolyte have been reported. Al-air batteries are characterised by low cost, sustainability and high theoretical specific energies 8100 Wh kg^{-1} [24], which are higher than the theoretical values of some lithium-ion batteries (~600 Wh kg^{-1}) [3]. The theoretical specific energy does not consider the weight of the oxygen electroactive species for the positive gas diffusion electrode because the battery utilises oxygen from the atmosphere [25]. In practice, aluminium-air batteries based on aqueous systems are still characterised by the slow kinetics of the oxygen reduction reaction, even if the aluminium alloy used, which is highly active. In addition, the use of air from the environment seems to be problematic due to the presence of nitrogen and carbon dioxide that could passivate the gas diffusion electrode catalyst. Furthermore, the parasitic corrosion and passivation of the aluminium electrode, except in very high concentrated alkaline electrolytes, lowers the cell potential and consequently the battery performance [26,27]. In general, the use of aqueous electrolytes enables only primary aluminium batteries because the aluminium re-deposition occurs at a more negative potential (-1.66 V *vs.* SHE [26]) than the hydrogen evolution. Secondary aluminium-based batteries are only possible in non-aqueous electrolytes with larger electrochemical stability window. [2]

1.1.2 Charge Storage Materials in Rechargeable Aluminium Batteries

Ionic liquid electrolytes can improve the stability and life-time of batteries compared to aqueous or organic solvents [14,28,29]. Proof-of-concept studies demonstrate that the performance of rechargeable aluminium batteries with an ionic liquid electrolyte can improve by introducing an active charge storage material as the positive electrode. Charge storage materials can reversibly intercalate or insert aluminium-anion species of the ionic liquid electrolyte like 1-ethyl-3-methylimidazolium chloride (EMImCl-$AlCl_3$) or 1,3-di-n-butylimidazolium bromide (BImBr-$AlCl_3$). Typical positive electrodes include porous and three-dimensional materials like graphite [9,11–13], zeolites [30], oxides [15–19,31], sulphides [20,32] and sulphur [21] (Table 1). Another type of positive electrode material is conductive polymers [1,22,33], which also store anions to compensate for the positive charges created during the oxidation of the polymer backbone. The aluminium battery systems with graphite, zeolites, sulphides and oxides show high reversibility, cycle stability, constant electrochemical behaviour and coulombic efficiencies >95 %. Aluminium batteries with oxides as the positive electrode show a very high specific discharge capacity. However, oxide, sulphide and zeolite-templated carbon electrodes have low cell potentials and rapidly decreasing discharge plateaus, which makes it difficult to define the specific energy and power. In addition, the oxides have a strong electrostatic interaction with the inserting anions, which complicates the reversible insertion process. Porous three-dimensional graphitic-foam [12] and pyrolytic graphite [9] electrodes are also promising. At the graphitic foam positive electrode, the $AlCl_4^-$ ions are intercalated and de-intercalated between the graphite layers while the metallic aluminium electrode oxidises to $Al_2Cl_7^-$ during the discharge cycle and is reduced back to aluminium during the charge cycle. This type of battery shows a high discharge cell potential of ~2 V and its specific energy (40 Wh kg^{-1}) is comparable to lead-acid and nickel-metal hydride batteries, which is less than half of the specific energy of high-performance batteries like lithium-ion (≥ 180 Wh kg^{-1} [3]). When using graphite electrodes, there is a partial irreversible intercalation of anions, especially during the initial charge and discharge cycles. After the first cycles, the capacity remains stable without a significant drop in performance. It is assumed that an activation process and adaption of the graphite structure takes place within the first cycles causing partial irreversibility [12]. [2]

1.1.3 Battery Systems Based on Aluminium and a Conductive Polymer

Conductive polymers like polythiophene, polypyrrole and polyaniline can theoretically store a higher amount of charge while simultaneously acting as a capacitor and battery [1]. These hybrid battery-capacitors combine the oxidation/reduction faradaic process of the conductive polymer and the non-faradaic behaviour by anion insertion/removal into the polymer. The non-faradaic charge stored depends on the thickness and porosity of the conductive polymer and is, therefore, an important parameter of the material. Hybrid battery-capacitors are potential positive electrode materials for high-performance batteries, which require high capacities and cell potentials. The use of conductive polymers as anion intercalation materials has already been demonstrated in lithium-ion batteries showing high coulombic efficiencies of up to 99 % and high specific energy in the range of 280-420 Wh kg^{-1} [1]. There are only two prior studies of conductive polymers coupled with aluminium, as the positive and negative electrodes respectively; one using the ionic liquid 1-ethyl-3-methylimidazolium chloride (EMImCl-$AlCl_3$) [22] and the other using 1-butylpyridinium chloride (BPCl-$AlCl_3$). These show a specific energy between 44-46 Wh kg^{-1} (Table 1). [2]

Table 1: Battery components (positive/negative electrodes and electrolyte) and characteristic battery values (measured average cell potential E, specific capacity Q_{spec} and energy E_{spec}) for rechargeable aluminium batteries with a charge-storage material as positive electrode. [2]

Positive electrode	Negative electrode	Electrolyte	*E*/ V	Q_{spec}/ Ah kg^{-1}	E_{spec}/ Wh kg^{-1}	Reference
Graphite	Al foil	Lewis acidic EMImCl-$AlCl_3$	1.7 to 2.0	70 to 148	40 to 64	[9–13]
Zeolite-templated carbon	Al foil	Lewis acidic EMImCl-$AlCl_3$	Sloping plateau 1.5	n/a	64	[30]

Positive electrode	Negative electrode	Electrolyte	*E*/ V	Q_{spec}/ Ah kg^{-1}	E_{spec}/ Wh kg^{-1}	Reference
Oxides, sulphides	Al foil and plate	Lewis acidic BMImCl- and EMImCl-$AlCl_3$	Sloping plateau 0.7 to 0.5	46 to 273	40 to 90	[15–20,31,32]
PPy on glassy carbon	Al foil	Lewis acidic EMImCl-$AlCl_3$	Sloping plateau ≥1.0	30 to 100	46	[22]
PEDOT on glassy carbon	Al foil	Lewis acidic EMImCl-$AlCl_3$	Slightly sloping plateau ≥1.0	30 to 100	44	[22]
PAn on platinum	Al rod	Lewis acidic BPCl-$AlCl_3$ and EMImCl-$AlCl_3$	≤1.6	45 to 68	n/a	[33]

The synthesis path of the conductive polymer influences the cycle stability of the battery. Conductive polymer films prepared chemically with a binder, show lower cycle stability and reversibility than those synthesised at constant current or potential on vitreous carbon [22]. In addition, the polymerisation media, aqueous or non-aqueous, has a significant influence on reversibility and degradation. The films synthesised in aqueous electrolytes can suffer damage if a small amount of water remains in the structure because the hygroscopic chloroaluminate ionic liquid can form hydrochloric acid during cycling, which could cause detachment of the film from the substrate. A better approach is the direct synthesis of the conductive polymers in chloroaluminate ionic liquids [22]. The films show higher reversibility

and higher mechanical stability than those prepared in aqueous solutions or conventional organic solvents like acetonitrile [34,35]. The surface structure of an electropolymerised polythiophene film on a planar vitreous carbon substrate appears as granular agglomerated structures both in aqueous and ionic liquid electrolytes. Quartz crystal microbalance studies consistently show that a mixture of anionic species of the ionic liquid is inserted into the conductive polymer during electropolymerisation and cycling. Larger anion species like $AlCl_4^-$ and $Al_2Cl_7^-$ could have a significant influence on the capacity and stability of the conductive polymer because they could remain trapped in the polymer structure if the pores are too small, and impede the reversible shuttling of the insertion anions. It is also reported that the conductive polymer is affected by swelling due to the size of the anions of the chloroaluminate ionic liquid [1,22,31,33]. The swollen polymer films could offer higher porosity and ability to accommodate bulky anions. Moreover, three-dimensional conductive polymer electrodes with a high surface area are suggested to create more space as well as higher numbers of anion insertion sites and accommodate more anions, which will increase the capacity and the specific power of the battery system [1]. [2]

2 Research Aim and Idea

This work aims to demonstrate a new battery concept beyond lithium-ion combining values of safety, sustainability and performance in a single battery system. An initial proof-of-concept study of an aluminium-conductive polymer battery shows the feasibility of the proposed battery concept and discusses preliminary performance in terms of specific energy and power as well as limitations. The identified shortcomings are addressed and improved, particularly by understanding mechanistic behaviour of the conductive polymer electrode interaction with the ionic liquid electrolyte. The fundamental understanding enables the performance-orientated synthesis of conductive polymer electrodes, which are tested finally in battery test cells. The determined battery characteristic behaviour and values are critically classified and compared with state-of-the-art rechargeable battery systems. Suggestions for further improvements and modifications are made.

In this chapter paragraphs, figures and equations were published and reproduced with permission of Springer Berlin Heidelberg [1] and The Royal Society of Chemistry [36].

2.1 The Aluminium-Conductive Polymer Battery Concept

The battery proposed in this work is composed of a metallic aluminium electrode (anode, negative electrode) and a conductive polymer (cathode, positive electrode) in an imidazolium-based chloroaluminate ionic liquid electrolyte (Figure 2). The battery operates by reversible deposition (charge) and dissolution (discharge) of aluminium (Equation 1) at the negative electrode. This is possible in a Lewis acidic chloroaluminate ionic liquid that contains heptachlorodialuminate ions ($Al_2Cl_7^-$) [37–42]. [1]

Anode reaction (negative electrode): Aluminium deposition and dissolution:

$$4Al_2Cl_7^- + 3e^- \underset{\text{discharge}}{\overset{\text{charge}}{\rightleftharpoons}} Al + 7AlCl_4^- \qquad (1)$$

At the positive electrode, the conductive polymer undergoes a redox reaction like a battery (Equation 2), generating positively charged sites at a certain number of monomer units in the polymer during the oxidation (charge). When the polymer is reduced (discharge), the charged

sites return to their neutral state. The unique characteristic of the conductive polymer is that in parallel to this redox reaction, the charged centres generated are compensated by anions X^- ($Al_2Cl_7^-$ or $AlCl_4^-$) from the electrolyte which are inserted and incorporated into the nano/micro-porous polymer structure as electrical charges [43–45]. The anions are reversibly removed when the polymer is discharged again. [36]

The number of inserted anions which compensate a positive charge per monomer unit is determined by the generated and accessible charged sites in the polymer, increasing with the state of charge. The number of inserted anions per monomer unit is described as the degree of anion insertion α (α = 0 to 1) [46–48]. If the polymer is completely discharged, the degree of insertion is α = 0 and no anions are inserted. A degree of insertion α = 1 indicates that every monomer unit compensates an anion. The polymer would then be fully charged. [1,36]

Cathode reaction (positive electrode): Conductive polymer oxidation/anion insertion and reduction/anion removal:

$$\mathrm{MonomerUnit}_\alpha + X^- \underset{\text{discharge}}{\overset{\text{charge}}{\rightleftharpoons}} [\mathrm{MonomerUnit}]_\alpha X + e^- \qquad (2)$$

The overall reaction of the aluminium-conductive polymer battery (Equation 3):

$$3\,\mathrm{MonomerUnit}_\alpha + 3X^- + 4Al_2Cl_7^- \underset{\text{discharge}}{\overset{\text{charge}}{\rightleftharpoons}} 3[\mathrm{MonomerUnit}]_\alpha X + Al + 7AlCl_4^- \qquad (3)$$

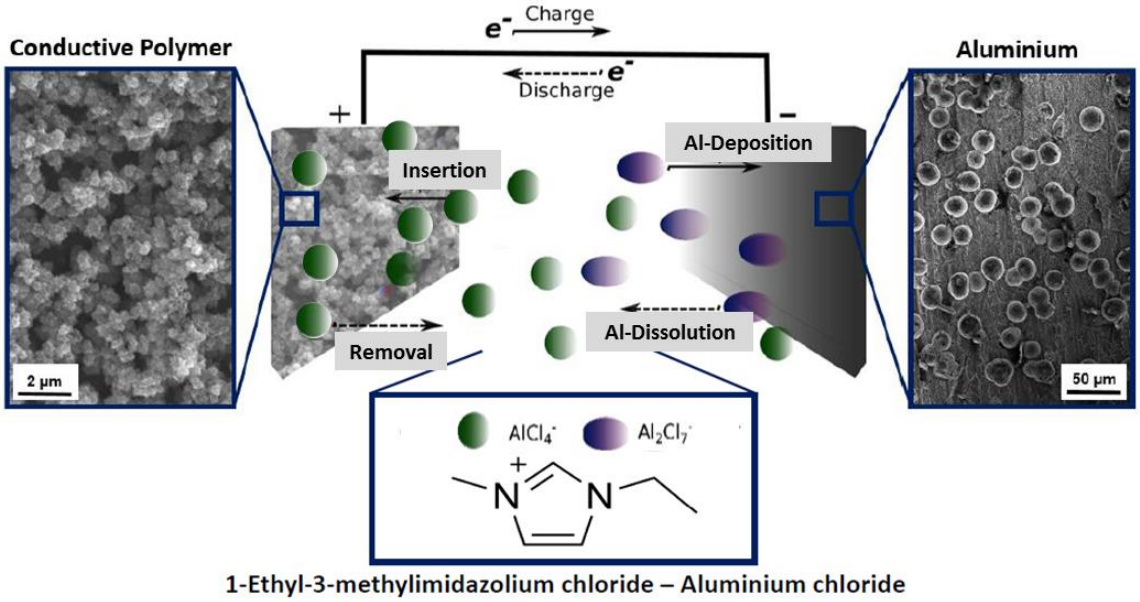

Figure 2: Schematic illustration of a rechargeable aluminium-conductive polymer battery with chloroaluminate ionic liquid electrolyte. [adapted from 1]

3 Theoretical Background

The three main components of the aluminium-conductive polymer battery are the metal aluminium anode, PEDOT cathode and imidazolium-based chloroaluminate ionic liquid electrolyte EMImCl-$AlCl_3$. The deposition/dissolution of aluminium in a Lewis acidic electrolyte is already a well-studied reaction, whereas the interaction between PEDOT and EMImCl-$AlCl_3$ and the charge storage mechanism at the cathode are not yet completely understood but significantly affect the performance of the whole battery system. The following chapter discusses the main characteristic, the suggested charge storage model and half-cell reactions in ionic liquid both for the aluminium and PEDOT electrode.

In this chapter paragraphs and equations were published and reproduced with permission of The Electrochemical Society [2] and The Royal Society of Chemistry [36].

3.1 Conductive Polymers

Conductive polymers such as poly-(3,4-ethylenedioxythiophene) (PEDOT) (Figure 3) offer the advantageous characteristics of conventional polymers, including their light-weight, low-cost and stability in most media, but also their high metal-like conductivity in the range of 100 to 1000 S cm^{-1} [49,50]. Conducting polymers can exist in different electronic states, depending on the state of charge. In the uncharged state, they are intrinsically insulating and non-conductive. When the polymer is charged/oxidised, electrons are removed from its delocalised π-electron system without changing other bonds in the chains, holding the polymer together [51]. It is assumed that the conduction and valence band overlap with an increasing state of charge, increasing the conductivity [49,51]. In addition, an inter charge transfer is also expected caused by electron hopping between the polymer chains.

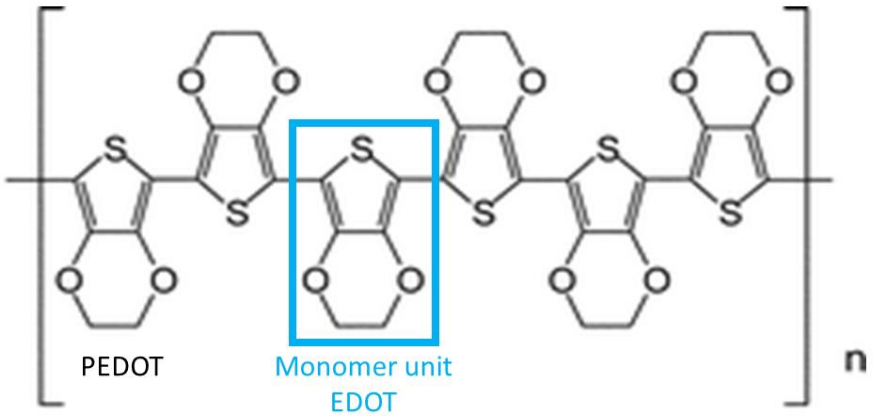

Figure 3: Structure of poly-(3,4-ethylenedioxythiophene) (PEDOT) with highlighted monomer unit 3,4-ethylenedioxythiophene (EDOT).

A thin film of the conducting polymer on a conductive substrate can be synthesised electrochemically by a constant current or potential electropolymerisation or cyclic voltammetry from a solution containing the monomer. The electropolymerisation can be divided into three steps starting with the formation of very short polymer chains in the electrolyte; followed by the nucleation on the conductive substrate and polymer growth [49,51]. The polymer properties such a morphology, structure, conductivity, stability depend on polymerisation method, media including anion species, temperature, polymerisation potential and the substrate. The polymerisation at constant current or potential causes a continuous growth of the polymer on its substrate. Low electropolymerisation potentials lead to short polymer chains (~16 monomer units), high potential lead to longer chains (≥32 monomer units), and very high potentials can form a cross-linked chain network [49]. In contrast to the continuous polymer growth at constant current or potential, the growth is periodically interrupted when electropolymerised using cyclic voltammetry. During the anodic cycle, the polymerisation occurs, and at the same time, the polymer is oxidised gradually with increasing potential. Simultaneously, anions from the electrolyte are inserted into the polymer film. During the cathodic cycle, the polymer is reduced, and anions are removed from the polymer. The polymer does not dissolve during reduction. With every polymerisation cycle, the current density increases due to added active mass. The electropolymerisation by cyclic voltammetry, scanning through a potential window and switching between insulating and charged state, leads to a mixture of polymer chains with different length. The polymer films appear more homogeneous and have a higher adhesion to their substrates than films obtained with

constant potential or current [49]. The film stability is also influenced by the polymerisation electrolyte. Polymer films can be synthesised in an aqueous solution, organic media such as acetonitrile and ionic liquids. Conductive polymers obtained in ionic liquids seem to have a good stability even in the highly charged state because of the low nucleophilicity of ionic liquids, leading to a lower affinity of highly charged polymer and ionic liquid.

3.1.1 Hybrid Battery-Capacitor Concept

Batteries have higher specific energies in comparison to capacitors, but capacitors usually have a higher specific power. In order to simultaneously improve the specific energy and power of an energy storage system, the advantages of battery and capacitor characteristics need to be combined. Battery and capacitor properties can be linked with electrodes with different storage mechanisms [36]. The main storage mechanisms are based on faradaic charge storage, which is typical for a battery, and also non-faradaic or capacitive charge storage by electrostatic interactions at the electrode double layer vicinity or pseudo-capacitive charge storage [52,53]. Pseudo-capacitive charge storage refers to a surface-bound redox-system, contributing to the total capacitance of the system [53]. The combination of these storage characteristics determines the operation principle of asymmetric batteries or capacitors and hybrid-battery-capacitors [53,54]. Asymmetric charge storage systems combine an electrode with faradaic and (pseudo-)capacitive charge storage mechanism, respectively. In such systems, the electrode with the faradaic charge storage mechanism delivers high specific energy and the electrode with a capacitive charge storage mechanism provides a high specific power [52]. Whereas asymmetric charge storage refers to a whole system, hybrid-battery-capacitors describe electrode materials with faradaic and capacitive charge storage mechanism [54,55]. Conductive polymers such as PEDOT are hybrid battery-capacitor materials because faradaic and non-faradaic charge transfer occurs interdependently while charging and discharging. It is assumed that PEDOT undergoes two main charge transfer steps (Figure 4). [36]

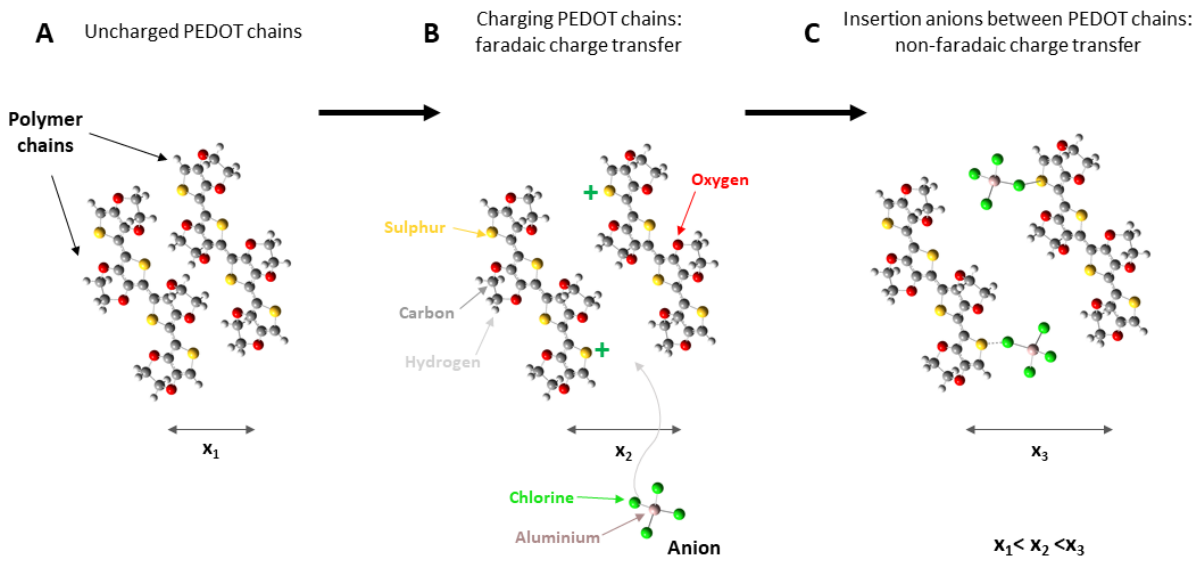

Figure 4: Illustration of two PEDOT chains (A) in the uncharged state, (B) during charging/oxidation and (C) in a fully charged state. The interchain distance x increases during charging of PEDOT (faradaic charge transfer) and insertion of anions (non-faradaic charge transfer).

PEDOT chains, with an interchain distance x_1, are in a neutral state of charge and non-conductive when uncharged (Figure 4 A). When PEDOT is charged/oxidised, positive charges are generated at specific monomer units (Figure 4 B). The generated positive charges are not located statically at a single atom of the polymer chain as PEDOT is a delocalised π-electron system. The oxidation of PEDOT is the faradaic (battery-like) reaction. If positive charges are generated in the vicinity of each other and at facing polymer chains, the chains are pushed away from each other because of repulsive forces between positively charged sites, increasing the interchain distance x_2. Consequently, tunnels are formed between the polymer chains enabling the insertion of anions and formation of a double layer along the polymer chains. The anion insertion and compensation of positively charged sites are associated with the non-faradaic charge transfer (capacitive charge transfer). The inserted anions, especially tetrahedral $AlCl_4^-$, create transport paths and stretch the interchain distance x_3 based on their anion radius. PEDOT is fully charged when all positively charged sites are compensated by inserted anions (Figure 4 C). At this stage, the polymer should be stretched to its maximum, appearing as a swollen polymer morphology. At very high anodic potentials an over-oxidation of the polymer can occur and lead to a degradation of the conductive polymer due to the

nucleophilic attack of the electrolyte [2,34]. When PEDOT is reduced/discharged, the charge transfer process is reversed. PEDOT loses its positive charged sites, inserted anions are removed subsequently as well as the double layer, and the polymer chain distances decrease again [56,57]. [2]

3.2 Ionic Liquids

The development of batteries with high cell potentials and capacity, providing high specific energy and power as well as excellent cycle life requires non-aqueous electrolytes which have a wide potential stability window, good conductivity and enable highly reversible electrode reactions while avoiding unwanted side reactions. Ionic liquids seem to fulfil these requirements for next-generation battery electrolytes, not least by their high electrochemical potential stability window from 4.5 V to 6 V. Some ionic liquids also attract attention as "green solvents" [58,59] as they are non-toxic, non-flammable, recyclable and even biodegradable [60]. Furthermore, ionic liquids are almost non-volatile in comparison to organic solvents, releasing no potential toxic-gases or decomposition products. The term "green" needs to be considered relatively. An electrolyte cannot be fully environmentally friendly and safe, but instead, it can be more "green" in comparison to other solvents such as organic electrolytes [61–63].

Ionic liquids are liquid salts, consisting exclusively of weakly coordinated ions that are liquid below 100 °C or even at room temperature [58,64–66]. At least one ion has a delocalised charge, and one component is organic, preventing the formation of stable crystal lattices at room temperature [67]. It is assumed that ion clusters are formed rather than ion pairs, which exist only for a very short time following a random motion [65,68,69]. The characteristics of each ionic liquid, such as electrochemical stability window, conductivity, viscosity and melting point, depend on the anion and cation composition [67,70,71]. The most common ionic liquids appearing in energy storage technologies are based on the imidazolium, pyrrolidinium and piperidinium cations in combination with tetrafluoroborate (BF_4^-), hexafluorophosphate (PF_6^-), bis(trifluoromethylsulfonyl)imide ($TFSI^-$) or halogenide (Cl^-, Br^-, F^-, I^-) anions. Numerous cation-anion combinations are possible. To date, there are over 300 commercial ionic liquids electrolytes available [72,73].

3.2.1 Aluminium Deposition in Chloroaluminate Ionic Liquid

One of the first generation ionic liquids contained tetrahedral aluminium anions and planar heterocyclic imidazolium cations (Figure 5) [67], such as a binary mixture of 1-ethyl-3-methylimidazolium chloride-aluminium chloride (EMImCl-$AlCl_3$, Figure 5). When the two solid components mixed together, they melt to a liquid in which all ionic species are fully dissociated. It means that all ionic species are able to take part in a batteries charge and discharge reaction actively. Chloroaluminate ionic liquids are highly hygroscopic, decomposing under an exothermic reaction to hydrochloric acid when exposed to moisture [68,74]. Therefore, they need to be handled in an inert atmosphere like argon or nitrogen with water levels below 100 ppm. The Lewis acidity of the ionic liquid depends on the molar ratio of $AlCl_3$ to EMImCl, determining properties such as viscosity, conductivity and potential stability window [60]. A mixture of more than 50 mol-% $AlCl_3$ is considered as Lewis acidic, while those with a 1:1 (50 mol-% EMImCl to 50 mol-% $AlCl_3$) composition are Lewis neutral and less than 50 mol-% are Lewis basic. Each composition contains a different predominant anion species. Lewis acidic liquids are characterised by $Al_2Cl_7^-$, neutral by $AlCl_4^-$ and basic by Cl^- anions (Figure 5) [64,75,76].

Figure 5: Structure of the cation $EMIm^+$ and the anions $Al_2Cl_7^-$, $AlCl_4^-$ and Cl^-.

The deposition of metallic aluminium from an EMImCl-$AlCl_3$ ionic liquid is only possible in a Lewis acidic composition in which the $Al_2Cl_7^-$ anion can be reduced (~-0.2 V *vs.* Al|Al(III)) (Equation 1) [64,76]. During the deposition, $Al_2Cl_7^-$ is depleted and $AlCl_4^-$ is formed, which means a shift in Lewis acidity towards Lewis neutral. The deposition from a Lewis neutral or basic composition is not possible as the $EMIm^+$ cation is decomposed before the reduction potential

of $AlCl_4^-$ (≤-2.0 V *vs.* Al|Al(III)) [74]. The aluminium deposition in Lewis acidic EMImCl-$AlCl_3$ ionic liquid forms nanocrystalline deposits [64]. Dendrite growth can only be observed at very high current densities ≥100 mA cm^{-2} caused by the depletion of $Al_2Cl_7^-$ and the subsequent localised change of Lewis acidity [76], causing preferential deposition on parts of the electrode surface protruding further into the electrolyte. Furthermore, a passivation layer of aluminium oxide is not formed in a dry chloroaluminate ionic liquid, showing high reversibility and coulombic efficiency of aluminium deposition/dissolution ≥80 % [77].

4 Experimental Methods

In this chapter paragraphs, figures, tables and equations were published and reproduced with permission of Springer Berlin Heidelberg [1], The Electrochemical Society [2], Elsevier [48], Elsevier [45] and The Royal Society of Chemistry [36].

4.1 Ionic Liquid Preparation

Lewis acidic, neutral and basic imidazolium-based ionic liquids were prepared using the components; 1-ethyl-3-methylimidazolium chloride (EMImCl; Merck, purity ≥98 %, water ≤1.0 %) and aluminium chloride ($AlCl_3$; Alfa Aesar, anhydrous, ultra-dry, packed in glass ampule under argon gas, metal basis 99.99 %). The Lewis acidity of the ionic liquid was controlled by the molar ratio of EMImCl to $AlCl_3$ (Table 2). [48]

Table 2: Molar ratio χ and mass m of EMImCl to $AlCl_3$ for 25 mL EMImCl-$AlCl_3$ ionic liquids with different Lewis acidity and dominant anion species, respectively [64, 48].

χ(EMImCl) / mol-%	χ($AlCl_3$) / mol-%	m(EMImCl) / g	m($AlCl_3$) / g	Lewis acidity	Predominant anions in ionic liquid
33.3	66.7	12.0	21.9	acidic	$Al_2Cl_7^-$, $AlCl_4^-$
50	50	16.6	15.1	neutral	$AlCl_4^-$
66.7	33.3	20.8	9.4	basic	$AlCl_4^-$, Cl^-

The components EMImCl and $AlCl_3$ were dried before use in a vacuum oven at 60 °C for 24 h and subsequently transferred into a glove box (MBraun, Workstations UNIlab Plus/Pro - SP/DP) with a nitrogen atmosphere (≤0.5 ppm water and ≤0.5 ppm oxygen). [48]

The amount of $AlCl_3$ m_A (Equation 4) and EMImCl m_E (Equation 5) for the synthesis of a Lewis acidic, neutral and basic ionic liquid was calculated based on the molar ratio χ, molar mass M of $AlCl_3$ and EMImCl and density ρ as well as volume V of the binary solution. [48]

$$m_A = \frac{\chi_A \cdot M_A \cdot \rho \cdot V}{\chi_A \cdot M_A + \chi_E \cdot M_E} \quad (4)$$

$$m_E=(\rho \cdot V)-m_A \quad (5)$$

The density of the solution ρ (Equation 6) was calculated by using the reported density ρ_a and corrected by a temperature dependent density coefficient ρ_b at 30 °C (Table 3) [78]. [48]

$$\rho=\rho_a+\rho_b \cdot (T-60) \quad (6)$$

Table 3: Density of EMImCl-$AlCl_3$ ionic liquid mixture ρ depending on the acidity at 30 °C [78]. [48]

Lewis acidity	$\rho_b \cdot 10^{-4}$ / g cm^{-3} °C^{-1}	ρ_a / g cm^{-3}	P / g cm^{-3}
acidic	9.17666	1.3567	1.36
neutral	8.0268	1.2660	1.27
basic	6.8555	1.2089	1.21

The calculated amounts of EMImCl and $AlCl_3$ were weighed inside the glove box with a scale (Ohaus, ± 0.001 g) and transferred into a clean dry beaker. The ionic liquid was prepared by adding $AlCl_3$ slowly to EMImCl during continuous stirring and cooling in a Peltier controlled cooling device with ceramic-coated beads (Techne, Bibby Scientific, N° ICE, 0-40 °C) (Figure 6 A). The ionic liquid reached temperatures between 20 °C to 40 °C during the mixing. Afterwards, the solution was transferred into a glass bottle and stirred for another 24 h, resulting in translucent yellowish solutions (Figure 6 B). The electropolymerisation solutions were prepared using the previously synthesised Lewis acidic, neutral and basic ionic liquids and 0.1 mol dm^{-3} 3,4-ethylenedioxythiophene (EDOT; Alfa Aesar, purity 97 %), which had previously been dried in vacuum at 60 °C for 24 h. The Lewis basic, neutral and acidic solutions resulted in a light yellow, red-brown and dark brown colour, respectively (Figure 6 C). [48]

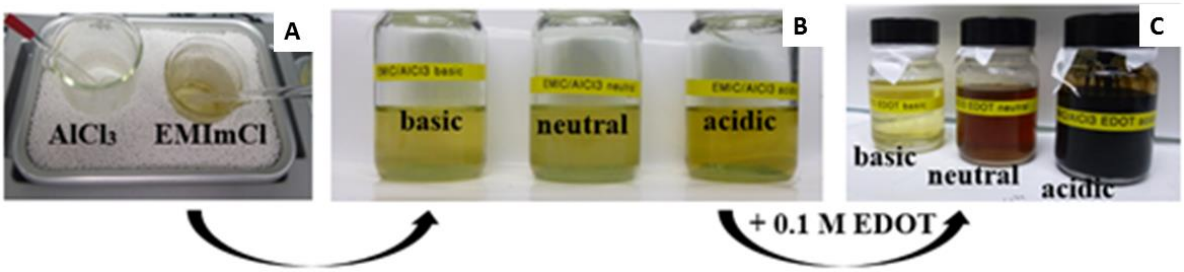

Figure 6: (A) Synthesis of EMImCl-$AlCl_3$ ionic liquid in a cooling bath. (B) Resulting Lewis basic, neutral and acidic solution. (C) Addition of 0.1 mol dm^{-3} EDOT and resulting Lewis basic, neutral and acidic solutions for electropolymerisation. [48]

4.2 Conductive Polymer Synthesis

PEDOT was synthesised by electropolymerisation in order to control the anion insertion into the conductive polymer, which depends on the applied potential. PEDOT films were initially synthesised in aqueous solution (Paragraph 4.2.1) for the proof-of-concept study of an aluminium-PEDOT battery. Later on, PEDOT was electropolymerised in chloroaluminate ionic liquid electrolyte (Paragraph 4.2.2) which is similar to the electrolyte used in the battery. The polymerisation in the chloroaluminate ionic liquids was carried out on both two- and three-dimensional substrates (Paragraph 4.2.2.1 and 4.2.2.2).

4.2.1 Polymerisation in Aqueous Solution

The monomer EDOT (>98.0 %) and potassium chloride (>99.5 %) were supplied by Wako Chemicals. The chloride ions from the potassium chloride are the insertion anions during the electropolymerisation. The PEDOT electrodes were prepared in a three-electrode cell at 28 °C and ambient atmosphere in an aqueous solution containing 0.01 mol dm^{-3} EDOT and 0.1 mol dm^{-3} KCl. EDOT was potentiostatically electropolymerised at 1.2 V *vs.* Ag|AgCl for 30 min on a planar vitreous carbon working electrode (4.5 cm^2). A platinum plate electrode (0.5 cm^2) was used as counter electrode and silver/silver chloride as reference electrode (Ag|AgCl/ 3 mol dm^{-3}, 0.197 V *vs.* SHE). The inter-electrode distance between the working and counter electrode was 1 cm. The reference electrode was connected by a salt bridge filled with agar powder (Wako, jelly strength 400 ~ 600 g cm^{-2}) over a Haber-Luggin capillary tube with the cell. The distance between the tip of the capillary and the working electrode was 0.3 cm. The cell potential was controlled with a potentiostat (BioLogic SP-240), using the commercial

software package EC-LAB (version 10.32). After the deposition, the PEDOT films were rinsed with deionised water and dried in vacuum for at least three days. [1]

4.2.2 Polymerisation in Chloroaluminate Ionic Liquid

The monomer EDOT was electropolymerised on both planar vitreous carbon (VC; Micro-to-Nano, 0.8 cm^2) and on three-dimensional reticulated vitreous carbon (RVC; Duocel, ERG Aerospace, 1.4 cm^2) working electrodes in imidazolium-based chloroaluminate ionic liquids in a nitrogen atmosphere (≤0.5 ppm water and ≤0.5 ppm oxygen). The electropolymerisations were performed in a PTFE-cell with the working electrode facing a planar vitreous carbon counter electrode (Micro-to-Nano, 0.8 cm^2) at an inter electrode-distance of 2 mm. The cell was equipped with an aluminium-tip reference electrode (<1 mm) located very close to the working electrode (~0.5 mm). The tip of the reference electrode was polished with very fine abrasive paper in nitrogen in order to remove oxides at the aluminium surface. [45,48]

4.2.2.1 Polymerisation on Planar Vitreous Carbon

The electropolymerisation of PEDOT on planar vitreous carbon was performed by cyclic voltammetry from -0.5 V to 2.5 V *vs.* Al|Al(III) in EMImCl-$AlCl_3$ with 0.1 mol dm^{-3} EDOT (Alfa Aesar; 97 %) at 100 mV s^{-1}, over 20 cycles at 25 °C [48]. Lewis acidic, neutral and basic ionic liquid electrolytes each containing 0.1 mol dm^{-3} EDOT were tested as polymerisation solution.
The polymer surface was rinsed with monomer-free EMImCl-$AlCl_3$ (corresponding Lewis acidity) after the polymerisation to remove residual monomer from the surface. [48]

4.2.2.2 Polymerisation on Reticulated Vitreous Carbon

EDOT was polymerised on reticulated vitreous carbon by three methods: cyclic voltammetry from -0.5 to 2.5 V *vs.* Al|Al(III) at 100 mV s^{-1}, differential pulse amperometry (DPA) and increasing pulse potentials (reverse normal pulse voltammetry; RNPV) from 0 V to 2.5 V *vs.* Al|Al(III) with a pulse length of 1 s and 200 pulses. The polymerisations were carried out in Lewis neutral EMImCl-$AlCl_3$ with 0.1 mol dm^{-3} EDOT. [45]

4.3 Electrode Characterisations

The conductive polymer (Paragraph 4.3.1) and aluminium (Paragraph 4.3.2) electrode were both characterised by their electrochemical behaviour in chloroaluminate ionic liquid and morphological appearance.

4.3.1 Conductive Polymer Electrode Characterisation

The conductive polymer electrodes were electrochemically characterised by cyclic voltammetry (CV; Paragraph 4.3.1.1), electrochemical quartz crystal microbalance measurements (EQCM; Paragraph 4.3.1.2) and electrochemical impedance spectroscopy (EIS; Paragraph 4.3.1.3). The polymer morphology was investigated by scanning electron microscopy (SEM; Paragraph 4.3.1.4) and in-operando atomic force microscopy (AFM; Paragraph 4.3.1.5).

4.3.1.1 Cyclic Voltammetry

The same three-electrode cell used for the electropolymerisation (Paragraph 4.2.2), was employed for the determination of the potential stability windows of the Lewis acidic, neutral and basic ionic liquid and for the characterisation of PEDOT films in Lewis acidic, neutral and basic ionic liquid. The potential stability windows were studied by increasing the potential window of the cyclic voltammetry measurement in the anodic and cathodic direction, respectively. The PEDOT films were characterised by cyclic voltammetry in different potential windows from -0.5 V to 2.5 V *vs.* Al|Al(III) in a monomer-free ionic liquid. The characterisations focused on the determination of the anion insertion and removal potentials, the transferred charges and reversibility of the anion intercalation. All cyclic voltammetry measurements were performed at scan rates between 10 mV s^{-1} and 100 mV s^{-1} and ~25 °C. [36,45,48]

4.3.1.2 Electrochemical Quartz Crystal Microbalance Measurements

The electrochemical quartz crystal microbalance (EQCM) set-up (Figure 7) comprises a three-electrode arrangement in a PTFE cell controlled by a potentiostat (Princeton Applied Research 263A). An AT-cut quartz crystal with a sputtered gold surface (KVG, 10 MHz, 0.22 cm^2) is used as a working electrode and substrate for the polymer. The polymer film was electropolymerised on the gold quartz crystal by cyclic voltammetry from -0.5 V to 2.5 V *vs.* Al|Al(III) in Lewis neutral EMImCl-$AlCl_3$ with 0.1 mol dm^{-3} EDOT at 100 mV s^{-1}, over 20 cycles at 25 °C. A vitreous carbon rod (Micro to Nano, diameter 0.3 cm) placed opposite to the quartz acted as a counter electrode, whereas an aluminium ring was used as reference electrode (Alfa Aesar, 99.999 % metal basis, diameter 0.5 mm). [36]

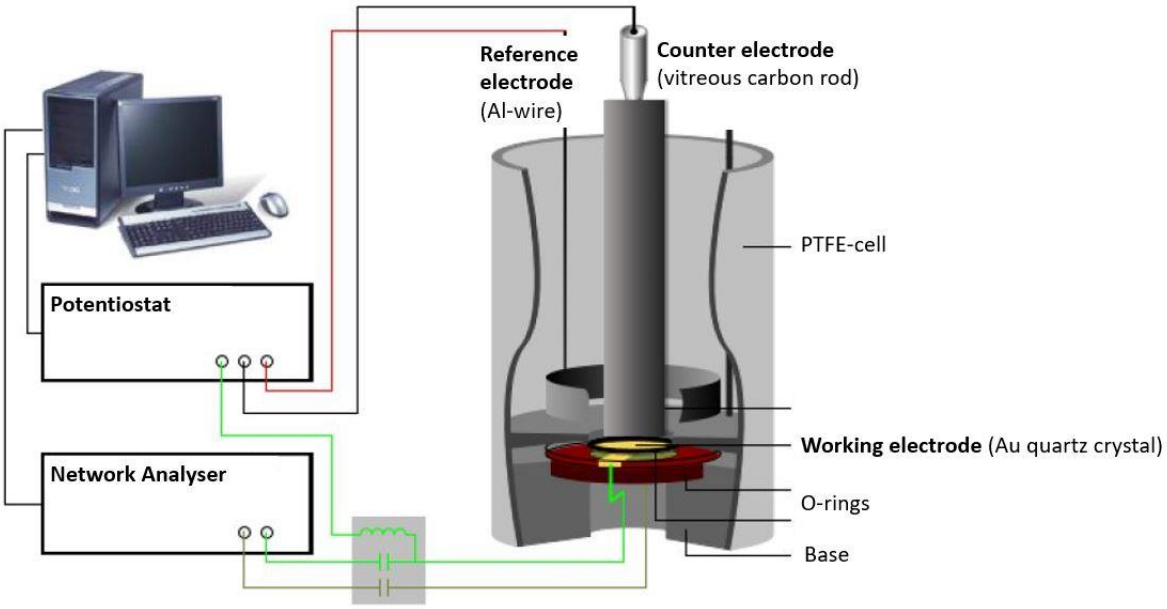

Figure 7: Schematic illustration of the experimental set-up of the quartz crystal microbalance adapted from [56, 36].

By combining electrochemical and EQCM measurements, two electrical signals overlap at the working electrode: a DC voltage, applied by the potentiostat and a high-frequency AC voltage from the network analyser (Agilent E5100A), which causes the oscillation of the quartz.
The change of the quartz resonance frequency caused by the mass changes of the polymer film due to anion insertion/removal is determined by the admittance of the quartz crystal with the network analyser. The spectrum of the admittance has the form of a Lorentz curve, so that the resonance frequency *f* and the quartz damping *w*, which is defined as the width at half the height of the admittance peak, can be determined by curve fitting. [36]

The resonance frequency and the damping provide information about the properties of the quartz crystal and the polymer film as they are mechanically coupled. Therefore, the mechanical properties of the polymer can be combined with the quartz to obtain a single mechanic system, which can be read as one electrical signal. The most accurate electrical description of a quartz crystal is currently given by the Electric Line Model (Transmission Line Model), based on a Mason 3-port model [56,79]. Changes of the electric impedance of the quartz can be translated into a film impedance of the polymer. The oscillation of the quartz causes a shear wave on the surface of the quartz, which is transmitted to the polymer film. Depending

on the polymer properties, such as film density ρ_f, the shear wave is dampened. Therefore, the film impedance Z_f is related to the shear modulus G of the system (Equation 7) [56]. [36]

$$Z_f=\sqrt{\rho_f G} \quad (7)$$

The shear modulus describes the linear elastic deformation of the polymer film and provides information about changes of the polymer stiffness or softness. [36]

4.3.1.2.1 Determination of the Shear Modulus

Ideal planar and rigid films move in phase with the quartz surface of area A. In this case, the change of resonance frequency Δf is proportional to the mass change Δm of the polymer film, and the Sauerbrey equation (Equation 8) [56,80] can be applied. The parameter f_0 indicates the resonance frequency of the unloaded quartz, which has a shear modulus μ_Q of $2{,}957 \times 10^{11}$ g cm s^{-2} and a density ρ_Q of 2,648 g cm^{-3}. [36]

$$\Delta f=-\frac{2f_0^2}{\sqrt{\rho_Q \mu_Q}}\rho h=-\frac{2f_0^2}{\sqrt{\rho_Q \mu_Q}}\frac{\Delta m}{A} \quad (8)$$

Since conductive polymers are not ideal planar rigid films, their viscoelastic properties cause a phase shift and damping of the shear wave propagation. Furthermore, the contact of the polymer film with the electrolyte causes an additional film impedance Z_l. If the electrolyte is inside the polymer pores and on the rough polymer surface (Figure 8), its impedance needs to be considered as it contributes to the overall impedance, which depends on the film thickness h_f. [36]

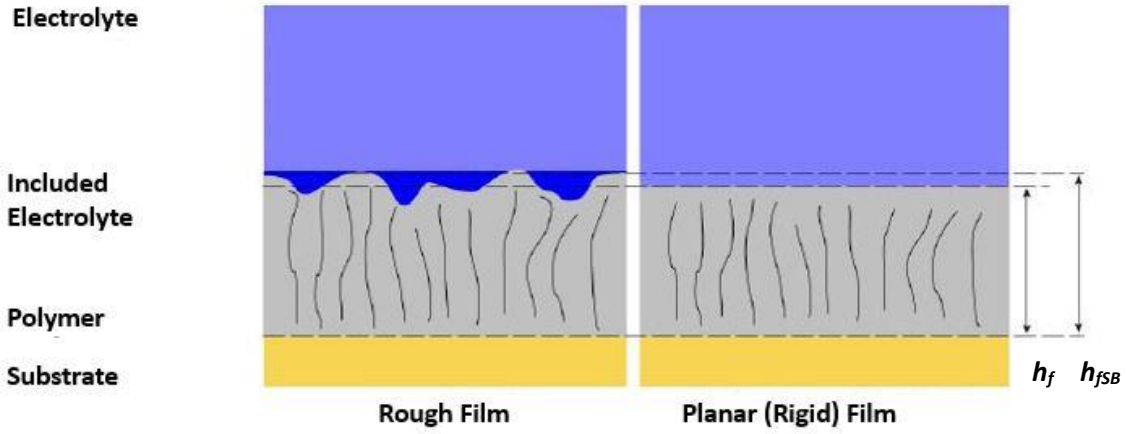

Figure 8: Schematic illustration of a cross-section of a rough and planar polymer film in fluid adapted from [56].

A complex shear modulus *G** for viscoelastic materials can be defined (Equation 9). *G** comprises a real part *G'*, presenting the deformation energy, which can be recovered (elastic behaviour) and an imaginary part *G''*, describing the amount of energy, which is lost due to friction and dissipated as heat. [36]

In this work, the changes of the shear modulus were studied instead of the quantitative mass changes of the polymer during the charging/discharging cycles as the damping change of the viscoelastic polymer film is expected to be higher than the resonance frequency changes. [36]

$$G^{*}=G^{'}+iG^{''} \qquad (9)$$

The final equation [56,81–94] for solving the film impedance numerically and shear modulus was calculated [56,82,83] (Equation 10 and 11) by the software package Mathematica® (Appendix 8.1) by using FindRoot[]-function. [36]

$$0=fn(Z_f)=\frac{\sqrt{i}+\frac{Z_f}{X_l}\tanh\left(i\frac{bZ_{fSB}^{m}}{Z_f}\right)}{1+\sqrt{i}\frac{X_l}{Z_f}\tanh\left(i\frac{bZ_{fSB}^{m}}{Z_f}\right)}-[Re+iIm] \qquad (10)$$

$$G^{*}=G^{'}+iG^{''}=\frac{Z_f^2}{\rho_f}=\frac{Re^2(Z_f)-Im^2(Z_f)}{\rho_f}+i\frac{2Re(Z_f)Im(Z_f)}{\rho_f} \qquad (11)$$

The film impedance Z_f includes the unknown shear modulus G^* and the film density ρ_f, whereas the motional film impedance, which is estimated by the Sauerbrey equation, Z_{fSB}^m, includes the film thickness h_f and density (Equation 12). [36]

$$Z_{fSB}^m=\omega_0\rho_f h_{fSB} \quad (12)$$

The reactance of the electrolyte is represented by X_l (Equation 13). [36]

$$X_l=\sqrt{2\pi f_0\rho_l\eta_l} \quad (13)$$

In order to determine the shear modulus, assumptions for the film thickness and density of the polymer film need to be made. For the polymer density, the monomer density is assumed. The film thickness needs to be estimated. As a first step, it is considered that the polymer consists of a rigid planar film, and the film thickness h_{fSB} is estimated by the Sauerbrey equation. In a second step, the polymer film thickness is corrected by multiplying with the correction factor b (Equation 14), accounting for all deviations of a viscoelastic to an ideal film such as film roughness and density differences (Equation 14). [36]

$$bh_{fSB}=h_f \quad (14)$$

A correction factor b=1 would indicate a rigid and planar surface. The upper limit should be slightly larger than one. In order to determine the correction factor and the complex shear modulus G^*, the b value was varied. The correction factor b was determined by finding the maximum of G' (Figure 9), as G' is a function of b [56]. In this study, an interval of b from 0.5 to 5.5 was selected. [36]

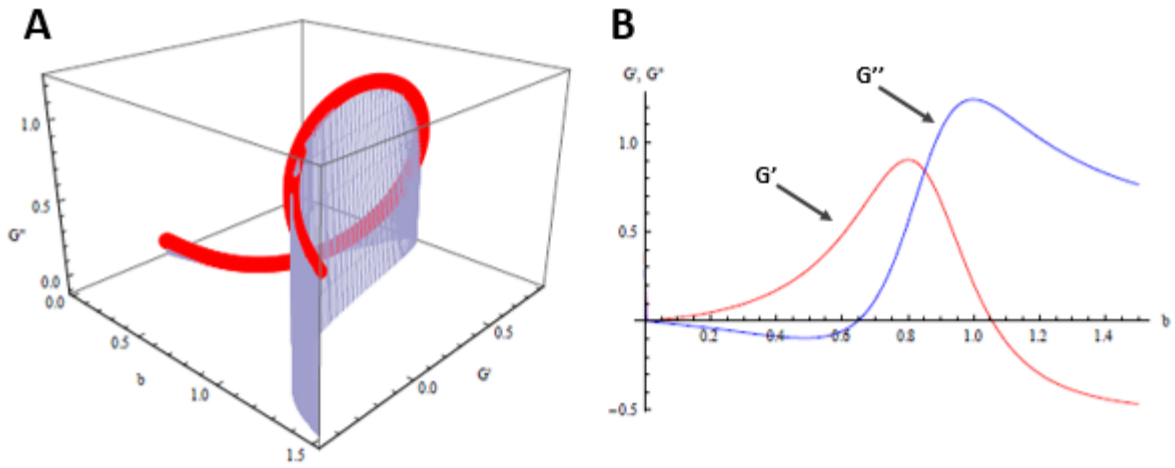

*Figure 9: (A) Illustration of the complex shear modulus G*and (B) real G' (red) and imaginary G'' (blue) part depending on the correction factor b* [adapted from 56].

This is the primary task of the developed script (Appendix 8.1). Since *b* is a parameter for the calculation of *G**, a list "databb" is generated, which contains all b-values. First the Mathematica FindRoot[]-function determines Z_f and then *G** for each *b* in databb. Afterwards, the maximum and the associated b_{Gmax} are determined for *G'*. If both components of the shear modulus for b_{Gmax} are greater than zero, they are added to the result list. [36]

4.3.1.3 Electrochemical Impedance Spectroscopy

The electrochemical impedance spectroscopy (EIS) experiments were performed in the same electrochemical cell as the electropolymerisation (Paragraph 4.2.2). PEDOT was charged successively in 500 mV steps by linear sweep voltammetry (LSV) with 100 mV s^{-1} from 0 V to 2.5 V *vs.* Al|Al(III). The LSV was stopped after every 500 mV, and a constant potential (DC amplitude) was applied at 0 V, 0.5 V, 1.0 V, 1.5 V, 2.0 V and 2.5 V *vs.* Al|Al(III). The spectra were discussed as Nyquist (1 mHz to 500 kHz) and Bode (1 mHz to 1 MHz) plots.

4.3.1.4 Scanning Electron Microscopy

The morphology of the PEDOT films obtained on planar and reticulated vitreous carbon, films polymerised at different potential windows (-0.5 V to 1.5 V 2.0 V and 2.6 V *vs.* Al|Al(III), 100 mV s^{-1}, 25 °C) and before/after battery cycling (after 100 cycles) in Lewis neutral EMImCl-$AlCl_3$ were investigated by scanning electron microscopy (SEM; LEO 1450VP and JEOL JSM 6500F). The samples were rinsed beforehand with dimethyl carbonate and dried in vacuum

for at least 1 h in order to remove residual electrolyte. All SEM images were post-processed to improve contrast and brightness. [1,45,48]

4.3.1.5 In-Operando Atomic Force Microscopy

The experimental set-up for the in-operando atomic force microscopy (AFM) measurements (Figure 10) consists of a self-designed PTFE three-electrode cell with a vitreous carbon disc (Micro to Nano, 6.3 cm^2) as substrate/working electrode, a vitreous carbon ring (Micro to Nano, diameter 3 cm) as counter and an aluminium wire (Alfa Aesar, 99.999 % metal basis, diameter 0.5 mm) as reference electrode. A Biologic SP-240 potentiostat controlled the electrochemical experiments. [36]

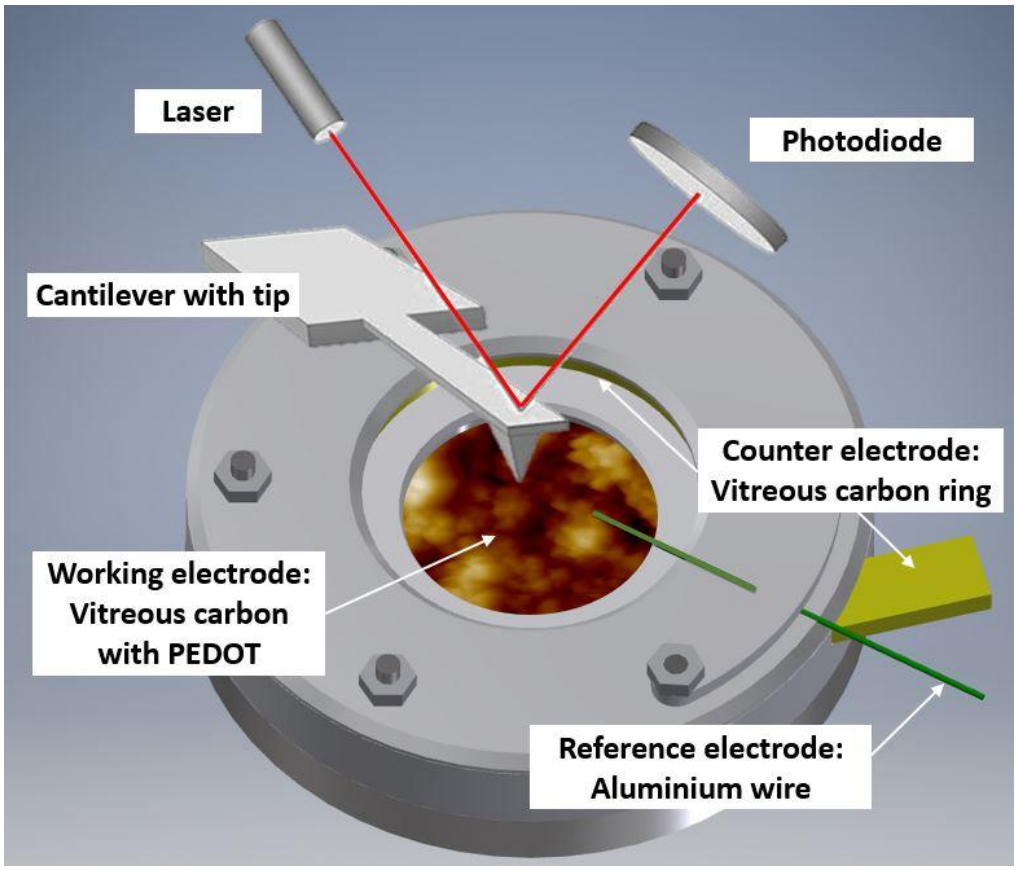

Figure 10: Schematic illustration of the in-operando AFM cell with PEDOT on vitreous carbon covered in Lewis neutral EMImCl-$AlCl_3$ ionic liquid. [36]

The AFM (Dimension ICON, Bruker Co., Billerica, MA, USA) located in a glove box (MBraun, Inertgas-Systeme GmbH), using argon atmosphere (water and oxygen level ≤10 ppm). The AFM measurements were carried out with a silicon probe coated with diamond-like carbon

and a reflective aluminium layer at the back (Windsor Scientific, Multi75DLC, spring constant 3 N m^{-1}, resonance frequency 75 KHz, tip radius <10 nm). The probe was entirely covered by the electrolyte (Lewis neutral EMImCl-$AlCl_3$) during the duration of the electrochemical experiment. [36]

Before the polymer film was charged/discharged, an initial AFM image of the PEDOT surface in the uncharged state was captured. The polymer surface was scanned horizontally over an area of 5 µm × 5 µm at 0.5 Hz, 512 samples per line and 0.05 V force set point. The feedback gain has been adapted automatically as the images were taken in ScanAsyst mode (peak force tapping mode). [36]

The initial position of the polymer surface was set as fixed scanning position and charged/discharged by linear sweep voltammetry (LSV) with 100 mV s^{-1} from 0 V to 2.5 V *vs.* Al|Al(III) and reverse to the uncharged state at 0 V. The LSV was stopped after every 500 mV and the potential was held at the open circuit potential (OCP) for capturing the AFM image with the same set of parameters as in the initial image. The OCP remained stable for the time required to capture the image. [36]

All AFM images were post-edited by a third-order polynomial flattening procedure using the Nanoscope Analysis software (Bruker Co., Billerica, MA, USA) to remove tilt and curvature. A movie combining the AFM images obtained at every step of the charge/discharge cycles is available (Appendix 8.2). [36]

4.3.2 Aluminium Electrode Characterisation

The aluminium deposition and dissolution were electrochemically characterised by cyclic voltammetry. The aluminium deposit morphology was investigated by scanning electron microscopy (SEM) and in-operando atomic force microscopy (AFM).

4.3.2.1 Cyclic Voltammetry

The same three-electrode cell used for the polymerisation and characterisation of PEDOT (Paragraph 4.2.2), was employed for the investigation of the deposition and dissolution of aluminium in Lewis acidic EMImCl-$AlCl_3$ in a potential window from -1.0 V to 1.0 V *vs.* Al|Al(III)

at 100 mV s^{-1} and 25 °C. Furthermore, the influence of the Lewis ionic liquid acidity $\chi(EMImCl):\chi(AlCl_3)$ on the reversibility of aluminium from strong acidic 30 mol-%:70 mol-% to slightly neutral 45 mol-%:55 mol was studied from -0.5 V to 0.5 V *vs.* Al|Al(III) at 100 mV s^{-1} and 25 °C.

4.3.2.2 Scanning Electron Microscopy

The morphology of aluminium deposits obtained on pure aluminium substrates before/after battery cycling (after 100 cycles) in Lewis acidic EMImCl-$AlCl_3$ in dependence on the Lewis acidity were investigated by scanning electron microscopy (SEM; LEO 1450VP and JEOL JSM 6500F). The samples were rinsed beforehand with dimethyl carbonate and dried in vacuum for at least 1 h in order to remove residual electrolyte. All SEM images were post-processed to improve contrast and brightness.

4.3.2.3 In-Operando Atomic Force Microscopy

The experimental set-up and conditions were the same as described in paragraph 4.3.1.5 for the in-operando AFM measurements of PEDOT except with Lewis acidic EMImCl-$AlCl_3$ electrolyte. Before the aluminium deposition, the bare vitreous carbon substrate surface was captured. The surface was scanned with a scan rate of 0.5 Hz, a scan size of 5 µm × 5 µm, 512 samples per line and a force set point of 0.1 V. The feedback gain has been adapted automatically as the images were taken in ScanAsyst mode (peak force tapping mode). Aluminium was deposited by linear sweep voltammetry (LSV) with 100 mV s^{-1} from 0 V to -1.0 V *vs.* Al|Al(III). The LSV was stopped at 0 V (before aluminium deposition), -0.2 V, -0.4 V, -0.5 V, -0.6 V and -1.0 V *vs.* Al|Al(III). The potential was held respectively at the OCP for capturing the AFM image with the same set of parameters as in the initial image of the bare aluminium surface. The OCP remained stable for the time spent to capture the image. All AFM images were post-edited by a third-order polynomial flattening procedure using the Nanoscope Analysis software (Bruker Co., Billerica, MA, USA) to remove tilt and curvature. [36]

4.4 Evaluation of the Proof-of-Concept Study

The initial concept of the aluminium-PEDOT battery in Lewis acidic EMImCl-$AlCl_3$ was evaluated with regard to its feasibility while charging and discharging. Metallic aluminium (99.99 %, 4.5 cm^2) was used as the anode, and PEDOT (4.5 cm^2) on planar vitreous carbon electropolymerised in aqueous solution (Paragraph 4.2.1) was used as the cathode. The cell

was charged and discharged with a constant current at 1.0 mA and -0.1 mA. The cell was additionally equipped with a commercially available porous (pore size range of 0.03 mm to 0.8 mm) glass separator as support for the electrolyte solution, which was soaked with an ionic liquid and placed between the electrodes. The experiments were performed with and without the electrolyte support and the results compared. [1]

4.5 Battery Design and Characterisation

In order to determine the charging/discharging behaviour of the advanced aluminium-PEDOT battery cell performance and long-term stability, battery cycling was carried out in a test cell (EL-CELL; PAT-Core cell with single PAT-testing socket) (Figure 11) placed in a glove box with nitrogen atmosphere (MBraun, UNIlab Pro Eco, ≤0.5 ppm water and ≤0.5 ppm oxygen) at ~25 °C. The positive electrode was previously polymerised PEDOT on RVC (4.2.2) soaked in monomer-free Lewis neutral EMImCl-$AlCl_3$ and the negative electrode was an aluminium disc (Alfa Aesar; 99.997 %, 1.2 cm^2, 0.1 mm thickness). The aluminium electrodes were polished with fine abrasive paper and rinsed with Lewis acidic EMImCl-$AlCl_3$ before battery cycling. A glass fibre separator (Whatman; 1.2 cm^2, 0.1 mm thickness) was soaked in Lewis acidic EMImCl-$AlCl_3$ (Sigma-Aldrich) (33 mol-%:67 mol-%) and placed between the positive and negative electrode.

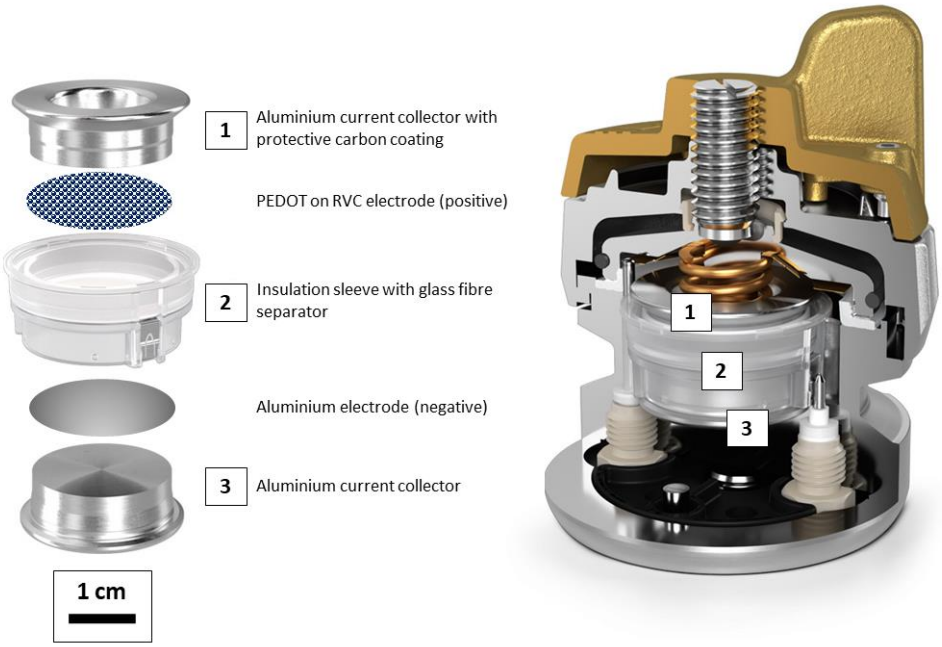

Figure 11: Schematic illustration of the battery test cell.

The separation of the electrolyte acidities at the aluminium and PEDOT electrode is a significant feature of this battery. The deposition of aluminium is only possible if the chloroaluminate species $Al_2Cl_7^-$ is present in the battery electrolyte [2]. This is the case in a strongly Lewis acidic composition (33 mol-%:67 mol-%) but also up to a slightly neutral composition (45 mol-%:55 mol-%) of EMImCl-$AlCl_3$, whereas the performance of the conductive polymer electrode is better in a Lewis neutral composition (50 mol-%:50 mol-%) with $AlCl_4^-$ as predominant anion [48]. For this reason, a gradient of electrolyte acidity from Lewis neutral at the PEDOT electrode to Lewis acidic at the aluminium electrode was established (Figure 12). In the pores of the polymer only $AlCl_4^-$ anions are enclosed, so that the Lewis acidity of the electrolyte in the pores remains unchanged.

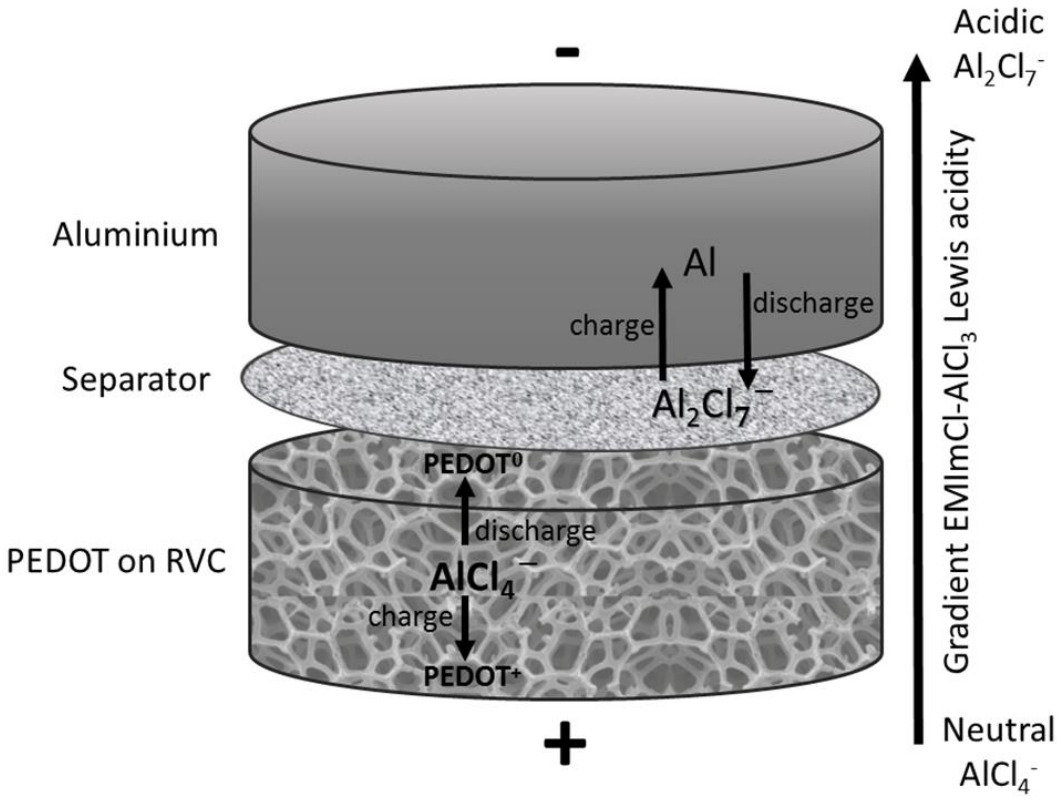

Figure 12: Schematic illustration of an aluminium-PEDOT battery with a gradient in Lewis acidity of the chloroaluminate ionic liquid.

4.5.1 Battery Charging and Discharging

The battery was charged until 2.2 V at constant current. The potential was subsequently held until the current reached only 0.15 mA (constant current constant voltage (CCCV) charging procedure). The cut-off potential for the constant current discharging was 0.5 V. The batteries were charged and discharged at different rates from 0.1 mA (0.8C) to 10 mA (80C) and -0.1 mA (0.8C) to -1 mA (8C), respectively.

4.5.2 Determination of the Battery Characteristic Values

Batteries are characterised by their specific values such as capacity Q_{spec} [Ah kg^{-1}], energy E_{spec} [Wh kg^{-1}] and power P_{spec} [W kg^{-1}] per unit active mass m_a (Equation 15 to Equation 17). Throughout this work, the average discharge potential E, applied discharge current I and discharge time t will be used to calculate the following specific values.

$$Q_{spec} = \frac{\int I dt}{m_a} \quad (15)$$

$$E_{spec} = \frac{EIt}{m_a} \quad (16)$$

$$P_{spec} = \frac{EI}{m_a} \quad (17)$$

The battery will also be characterised by its coulombic efficiency Q_{eff} (Equation 18) and energy efficiency E_{eff} (Equation 19).

$$Q_{eff} = \frac{Q_{charge}}{Q_{discharge}} = \frac{(\int I dt)_{charge}}{(\int I dt)_{discharge}} \quad (18)$$

$$E_{eff} = \frac{(EIt)_{charge}}{(EIt)_{discharge}} \quad (19)$$

4.5.2.1 Considered Active Mass

The battery characteristic values have been determined for three different cases in terms of considered active mass m_a in order to enable a fair comparison between reported specific energy and power of state-of-the-art batteries and other aluminium-based batteries [12,13,95,96].

Case 1) Active species: Considering solely the mass m_a (Equation 20) of species which actively take part in the battery reaction (Equation 3).

$$m_a(\text{case 1}) = m_a(Al_2Cl_7^-) + m_a(\text{EDOT}) \quad (20)$$

As the total mass of PEDOT (Equation 21) is considered, the mass polymerised around the struts of the RVC with an overall polymer film area [97] A_f of 2.1 cm^2 and film thickness [45] h_f of 3 µm. It is assumed that the density of PEDOT is approximately the density of one EDOT monomer unit (ρ(EDOT)≈ρ(PEDOT) with molar mass EDOT M(EDOT)=142 g mol^{-1}) [36].

$$m_a(\text{PEDOT}) = A_f h_f \rho(\text{PEDOT}) \quad (21)$$

The mass of $Al_2Cl_7^-$ anions (Equation 22) is determined by the deposited mass of aluminium during constant current charging Q_{charge}. The deposited mass of aluminium in the fully charged state was calculated via the Faraday equation (with a number of transferred electrons z=3 and Faraday constant F=96485 As mol^{-1}).

$$m_a(Al_2Cl_7^-) = \frac{4Q_{discharge} M(Al_2Cl_7^-)}{zF} \quad (22)$$

Case 2) Active species with insertion anions: Considering the mass m_a *of* active species like in case 1 with inserting $AlCl_4^-$ anions from Lewis neutral EMImCl-$AlCl_3$ in the PEDOT cathode (Equation 23) [96].

$$m_a(\text{case 2}) = m_a(Al_2Cl_7^-) + m_a(\text{EDOT}) + m_a(AlCl_4^-) \quad (23)$$

As the unique feature of the presented aluminium-PEDOT battery is the simultaneous oxidation/reduction of PEDOT and insertion/removal of $AlCl_4^-$ anions into the polymer

structure, the mass of inserting anions $m_a(AlCl_4^-)$ (Equation 24) should be considered additionally for a degree of anion insertion of 0.33. $AlCl_4^-$ is the only inserting anion as at the cathode a Lewis neutral EMImCl-$AlCl_3$ is present, which is soaked into the conductive polymer.

$$m_a(AlCl_4^-) = \frac{0.33\ m_a(EDOT)\ M(AlCl_4^-)}{M(EDOT)} \quad (24)$$

Case 3) All species: Considering the mass m_a of all species in the battery. This also includes species which do not actively take part in the battery reaction ("dead mass") such as $EMIm^+$ cations after the method of Kravchyk et al. [95]. This method is designed to account for the depletion of electrolyte species during charging, where $Al_2Cl_7^-$ is split into Al and $AlCl_4^-$. The latter is then extracted from the electrolyte and stored in the cathode. The electrolyte composition can only change from 2:1 (saturation of $AlCl_3$ in EMImCl) to ~1.1:1 (aluminium stops depositing from electrolyte) so that a certain quantity of $Al_2Cl_7^-$ is required. In the following equation (Equation 25) [95] F is the Faraday constant, x is the number of electrons involved in reducing 1 mol of $AlCl_3$, r is the maximum molar ratio of the electrolyte, Q_C is the specific capacity of the cathode (in mAh g^{-1}), and $M(AlCl_3)$ and $M(EMImCl)$ are the molar masses of $AlCl_3$ and EMImCl, respectively.

$$Q_{spec} = \frac{Fx(r-1)Q_c}{Fx(r-1)+Q_c(rM(AlCl_3)+M(EMImCl))} \quad (25)$$

This specific capacity and the overall charge capacity of the battery are then used to calculate the active mass m_a to be considered for energy and power density for case (3).

5 Results and Discussion

In this chapter paragraphs, figures, tables and equations were published and reproduced with permission of Springer Berlin Heidelberg [1], The Electrochemical Society [2], Elsevier [48], Elsevier [45] and The Royal Society of Chemistry [36].

5.1 Proof-of-Concept

The interest of the scientific community in batteries beyond lithium is rather significant. Therefore, the project idea, to combine aluminium and a conductive polymer (PEDOT) in an imidazolium-based chloroaluminate ionic liquid, is in line with the current trend regarding the development of novel energy storage chemistries. For the proof-of-concept study, conductive polymer electrodes were prepared by electropolymerisation in aqueous solution on planar vitreous carbon substrates. Metallic aluminium, previously synthesised PEDOT cathodes and a Lewis acidic chloroaluminate ionic liquid electrolyte were tested and characterised in battery cells. [1]

5.1.1 Preliminary Battery Evaluation

The aluminium-PEDOT battery in Lewis acidic EMImCl-$AlCl_3$ was assembled with a porous electrolyte support separating the aluminium and PEDOT electrodes as well as without a support (Figure 13). The battery operates by the deposition and dissolution of aluminium at the anode (Equation 1), showing a very porous surface (pore diameter ~0.4 µm to 1.4 µm) on the aluminium substrate surface and hemispherical aluminium deposits with a diameter of ~28 µm (Figure 13 A). PEDOT prepared by constant potential electropolymerisation in 0.01 mol dm^{-3} EDOT and 0.1 mol dm^{-3} KCl shows a granular and porous structure on planar vitreous carbon. The homogeneously distributed grains have an average size of 0.2 µm to 2 µm (Figure 13 C). The battery with an OCP of 1.3 V was charged and discharged at constant current

(1.0 mA and -0.1 mA) between 0.5 V and 2.35 V. During battery cycling (≤20 cycles) a detachment of the PEDOT film was observed in the ionic liquid, which appears as blue streaks in the ionic liquid electrolyte. The rapid loss of active cathode material caused a loss of contact and consequently, the failure of the battery. In order to limit the loss of PEDOT mass due to detachment of the film from the electrode, a porous glass support for the electrolyte was used. The aim was to keep the PEDOT film as close as possible to the vitreous carbon

electrode. The pore size is between 0.03 mm to 0.8 mm to allow the ions in the ionic liquid to move freely and maintain the ionic conductivity (Figure 13 B). It is assumed that the detachment of PEDOT is caused by residual water in the pores of the PEDOT electrode, which reacts with highly hygroscopic Lewis acidic EMImCl-$AlCl_3$. [1]

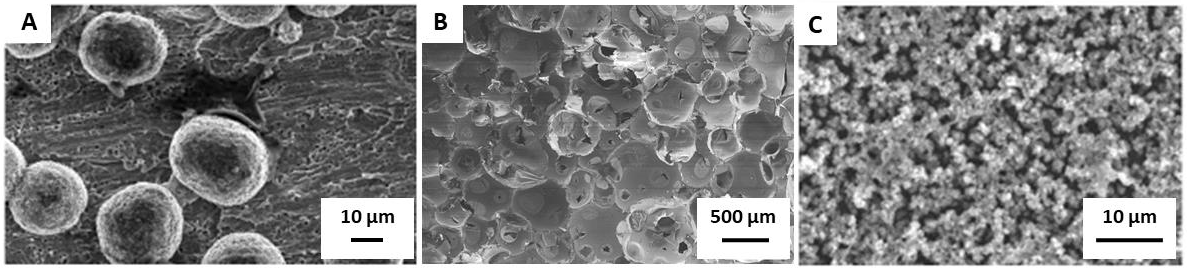

Figure 13: SEM images of (A) aluminium electrode surface after ~20 charge/discharge cycles in Lewis acidic EMImCl-$AlCl_3$, (B) porous glass electrolyte support in the dry state and (C) PEDOT electropolymerised at 1.2 V vs. Ag/AgCl for 30 min on planar vitreous carbon in 0.01 mol dm^{-3} EDOT and 0.1 mol dm^{-3} KCl aqueous solution. [adapted from 1]

The battery-related characteristics (Table 4), which are based on the deposited mass of PEDOT and the active mass of aluminium, show a specific energy and power of 84 Wh kg^{-1} and 228 W kg^{-1}, respectively. The discharge reaction for the cell with the porous electrolyte support is characterised by a significantly higher discharge capacity (0.05 mAh without and 0.17 mAh with electrolyte support). However, only a low coulombic efficiency of 38 % can be reached. [1]

Table 4: Comparison of charge/discharge capacity Q_{charge} and $Q_{discharge}$, specific energy E_{spec} and power P_{spec} of the initial aluminium-PEDOT battery in Lewis acidic EMImCl-$AlCl_3$ with and without electrolyte support. [1]

Battery Assembling	Q_{charge} / mAh	$Q_{discharge}$ / mAh	E_{spec} / Wh kg^{-1}	P_{spec} / W kg^{-1}
Without electrolyte support	0.44	0.05	84	179
With electrolyte support	0.44	0.17	228	143

In summary, the concept of an aluminium-PEDOT battery in chloroaluminate ionic liquid is feasible, showing good specific energy and power because of the light-weight active

materials. However, the capacity and coulombic efficiency are deficient, and the peformance is also affected by the loss of active material and very low cycle stability. [1]

5.2 Improvements of the Conductive Polymer Electrode

The proof-of-concept study of an aluminium-conductive polymer battery showed promising preliminary performance. However, the battery cells failed already at less than 20 charge and discharge cycles [1]. The reason for the failure is residual water from the electropolymerisation in the pores of the conductive polymer electrode, which can hardly be removed by drying. The water reacted with the highly hygroscopic and moisture-sensible ionic liquid electrolyte in the battery to form hydrochloric acid and chlorine gas, which caused a detachment of the polymer from its substrate [1].

The most obvious approach to stabilise the conductive polymer electrode is the electropolymerisation in a non-aqueous electrolyte, which is similar to the used battery electrolyte. On the one hand, the moisture is excluded and on the other hand, the same anion species, which is also present in the battery electrolyte, is already inserted in the polymer [48].

A further improvement was the effective increase of the active polymer area. This problem was addressed by synthesising three-dimensional conductive polymer-carbon composites in ionic liquid [45]. The electropolymerisation of a thin polymer film on a high surface area substrate assures larger availability of active material ("footprint area"), increasing the electrode capacity due to the higher number of inserted anions [97,98]. [45]

5.2.1 Synthesis of PEDOT Electrodes in Ionic Liquid

The electropolymerisation of PEDOT on planar vitreous carbon substrates was performed in Lewis acidic, basic and neutral EMImCl-$AlCl_3$ ionic liquid electrolyte with 0.1 mol dm^{-3} EDOT by cyclic voltammetry. [48]

A bare (monomer-free) Lewis neutral composition of EMImCl-$AlCl_3$ shows the widest stability potential window of ≥4 V with the anodic and cathodic potentials over 2 V and -2 V *vs.* Al|Al(III) before it decomposes $EMIm^+$ (cathodic) and the chloroaluminate species to chlorine gas (anodic), respectively (Figure 14). In contrast, the basic composition of the ionic liquid

shows anodic and cathodic potential limits between 1.3 V and -0.8 V *vs.* Al|Al(III) respectively, providing around 2.1 V of potential stability window. The acidic composition is stable between 1.5 V and -2 V *vs.* Al|Al(III). [48]

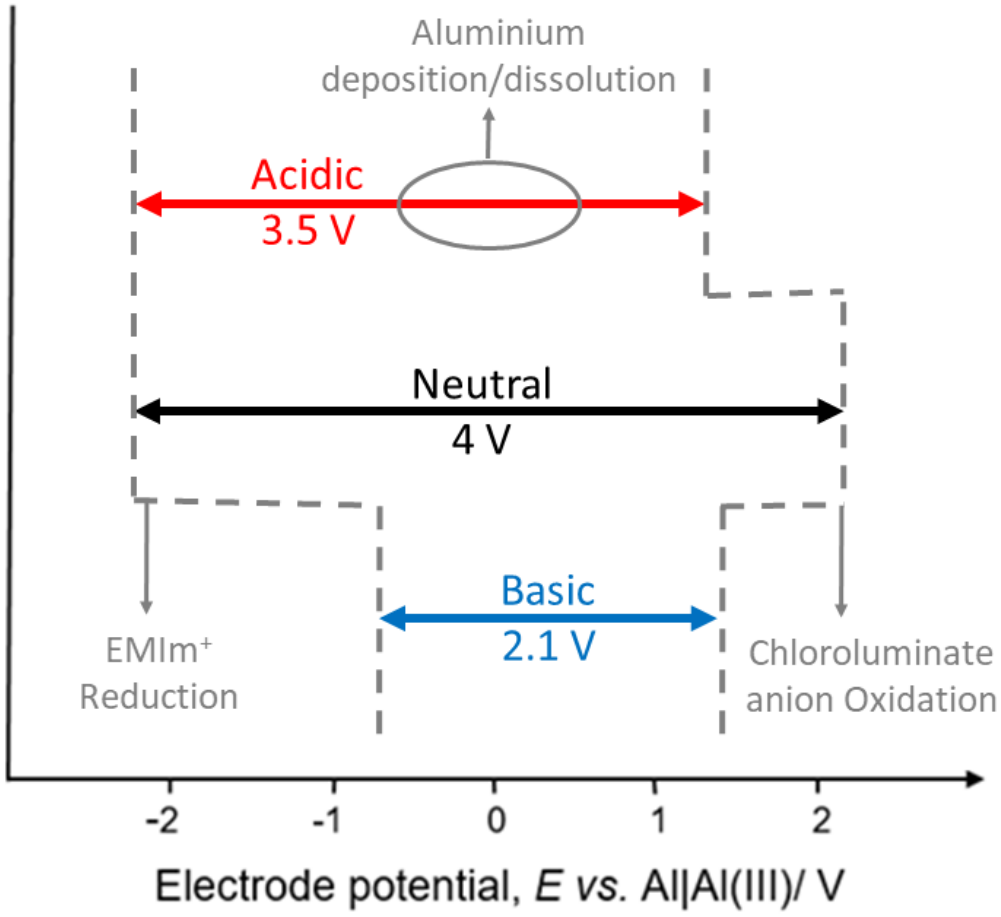

Figure 14: Stability potential windows of monomer-free Lewis acidic, neutral and basic EMImCl-$AlCl_3$ at 25 °C with vitreous carbon as working and counter electrode and aluminium as a reference electrode.

5.2.1.1 Polymerisation in Lewis Acidic Ionic Liquid

In a first step, the potential stability window of the monomer-free Lewis acidic EMImCl-$AlCl_3$ (χ(EMImCl):χ($AlCl_3$)=33 mol-%:67 mol-%) was determined by cyclic voltammetry. The aluminium deposition and dissolution occurs from -0.2 to -0.5 V and -0.2 V to 0.1 V *vs.* Al|Al(III) on a vitreous carbon substrate, respectively, in a monomer-free Lewis acidic EMImCl-$AlCl_3$. The decomposition of the cation species $EMIm^+$ on a vitreous carbon electrode was observed below -2.0 V *vs*. Al|Al(III) and the oxidation of the chloroaluminate anion to chlorine gas takes

place over ~1.5 V *vs.* Al|Al(III) (Figure 15, dashed line). The addition of 0.1 mol dm^{-3} EDOT to the Lewis acidic EMImCl-$AlCl_3$ caused a dark brown and very viscous solution to form immediately (Figure 6 C). It is assumed that a very stable complex is formed between EDOT and $AlCl_3$ [99]. The solution was tested to electropolymerise EDOT on a vitreous carbon electrode of 0.8 cm^2 surface area from 0 V to 2 V *vs.* Al|Al(III) (Figure 15, solid line). [48]

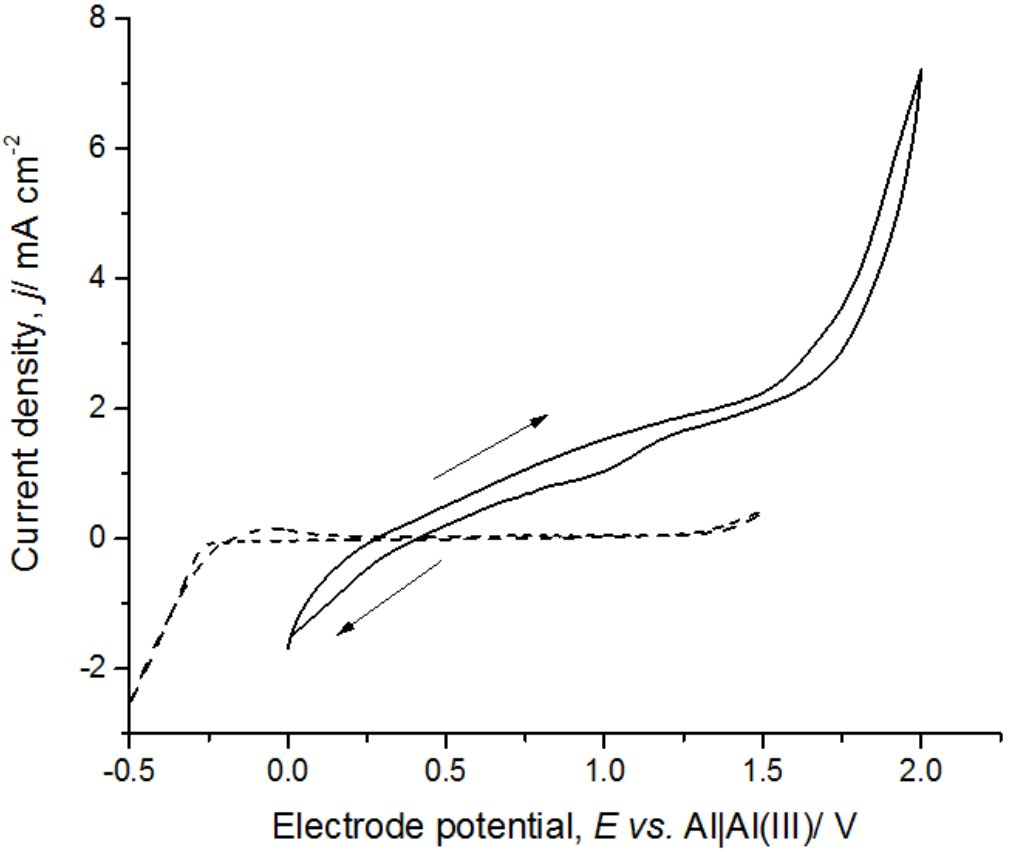

Figure 15: Cyclic voltammograms of a monomer-free Lewis acidic (dashed line, cycle 15) and with 0.1 mol dm^{-3} EDOT (solid line, cycle 15) EMImCl-$AlCl_3$ ionic liquid at 100 mV s^{-1} and 25 °C. [48]

The cyclic voltammetry of the Lewis acidic ionic liquid with 0.1 mol dm^{-3} EDOT showed a steadily increasing current at anodic potentials until 1.5 V *vs.* Al|Al(III). It is assumed that the current slope is caused by the high viscosity of the ionic liquid that increases the electrical resistance of the electrolyte. The solution decomposed to chlorine gas at potentials higher than 1.5 V *vs.* Al|Al(III). A polymer film was not deposited on the vitreous carbon substrate. Instead, EDOT and $AlCl_3$ formed a stable complex in solution, preventing further

electropolymerisation on the vitreous carbon substrate. However, a small peak around 1 V *vs.* Al|Al(III) in the backward scan is visible, which might be an indication of an anion removal process from a thin polymer film attached on the electrode surface. [48]

5.2.1.2 Polymerisation in Lewis Basic Ionic Liquid

The potential stability window of a monomer-free Lewis basic EMImCl-$AlCl_3$ (χ(EMImCl):χ($AlCl_3$) = 67 mol-%:33 mol-%) is very small in comparison to the Lewis neutral and acidic composition. The anodic and cathodic limits are below 1.5 V and -0.8 V *vs.* Al|Al(III), respectively (Figure 16, dashed line). The addition of 0.1 mol dm^{-3} EDOT to the light-yellow Lewis basic EMImCl-$AlCl_3$ ionic liquid did not cause any colour changes (Figure 6 C) and the electropolymerisation of EDOT on the electrode using this solution was not observed. The ionic liquid decomposed to chlorine gas from 1.5 V *vs.* Al|Al(III) before EDOT could have been polymerised, although the anodic stability potential window is ~0.5 V wider with EDOT than the bare Lewis basic ionic liquid (Figure 16, solid line). It is assumed that $EMIm^+$ forms a compound with EDOT, which is noticeable in the higher viscosity in comparison to the monomer-free ionic liquid. The decomposition in the more viscous liquid might be kinetically retarded, resulting in a larger potential stability window.

In addition, the conductivity of a Lewis basic chloroaluminate ionic liquid is lower (2.07 mS cm^{-1} at 21.4 °C [78]) than a Lewis acidic (14 mS cm^{-1} at 22.2 °C [78]) or neutral (21 mS cm^{-1} at 21.9 °C [78]) composition, which is represented in the lower current density of the cyclic voltammogram. [48]

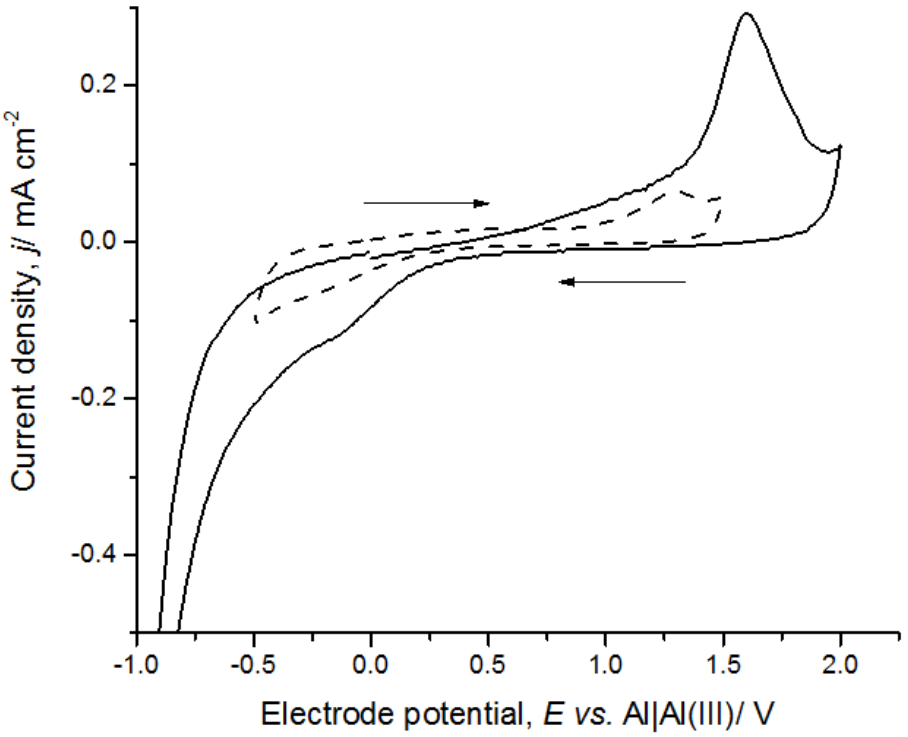

Figure 16 Cyclic voltammograms of a monomer-free Lewis basic (dashed line, cycle 3) and with 0.1 mol dm^{-3} EDOT (solid line, cycle 3) EMImCl-AlCl$_3$ ionic liquid at 100 mVs^{-1} and 25 °C. [48]

5.2.1.3 Polymerisation in Lewis Neutral Ionic Liquid

The monomer-free Lewis neutral solution (χ(EMImCl):χ(AlCl$_3$) = 50 mol-%:50 mol-%) has the widest potential stability window of ≥4 V from -2V to 2V *vs*. Al|Al(III) (Figure 17, inset CV). The Lewis neutral ionic liquid with 0.1 mol dm^{-3} EDOT changed colour from translucent yellowish to dark orange within 48 h (Figure 6 C). The cyclic voltammogram of the electropolymerisation from -0.5 to 2.6 V *vs.* Al|Al(III), recorded from 0 V *vs.* Al|Al(III), shows a continuous growth of the polymer film on the vitreous carbon surface with every cycle (Figure 17, main CV). The first two cycles show a clear peak >2.0 V *vs*. Al|Al(III), which is related to the nucleation of a polymer film on the vitreous carbon surface. Cycles three to twenty are characterised by the growth of polymer on the previously polymerised polymer. The anodic potential stability window of the Lewis neutral ionic liquid with 0.1 mol dm^{-3} EDOT seems to reach up to 2.8 V *vs*. Al|Al(III), which is ~0.8 V wider than the bare Lewis neutral ionic liquid.

The predominant anion in the Lewis neutral chloroaluminate ionic liquid is $AlCl_4^-$. The insertion of the anion into the conductive polymer co-occurs during the polymerisation of EDOT on the vitreous carbon electrode surface. The oxidation/polymerisation and anion insertion process is characterised by four anodic peaks at 0.75 V, 1.1 V, 1.7 V and 2.2 V *vs.* Al|Al(III), which overlap each other. The anion removal process shows two clear peaks at 1.6 V and 0.9 V *vs.* Al|Al(III). [48]

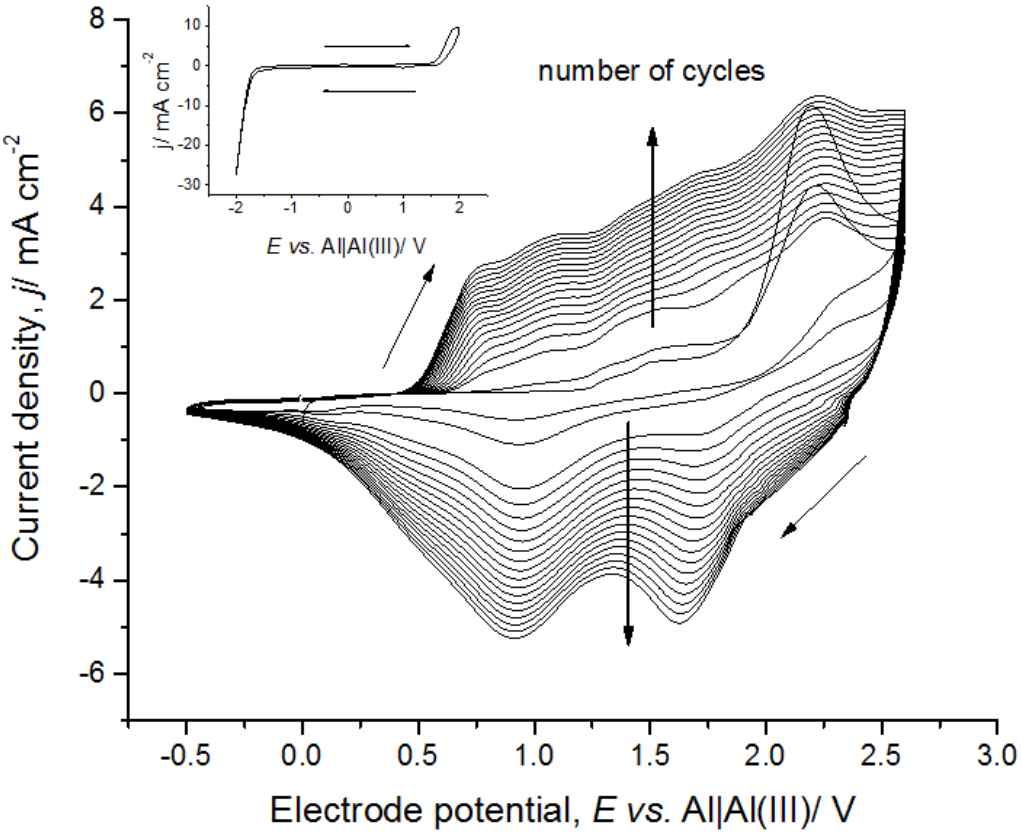

Figure 17: Cyclic voltammograms of a monomer-free Lewis neutral (inset CV, cycle 3) and with 0.1 mol dm^{-3} EDOT (main CV, 20 cycles) EMImCl-$AlCl_3$ ionic liquid at 100 mVs^{-1} and 25 °C. [48]

The anodic Q_a and cathodic Q_c transferred charges from cycle 1 to 20 increased from 35 mAs to 74 mAs and 19 mAs to 66 mAs, respectively, due to polymer growth and the formation of more anion insertion sites in the polymer film, which allows a higher number of transferred anions. If it is assumed that the cathodic transferred charges indicate the removal of $AlCl_4^-$ ($Q_c = Q_{remove}$), the same proportion of anodic charges Q_a will correspond to the initial amount of inserted charges $AlCl_4^-$ ($Q_{insert} = Q_{remove}$). The difference between the transferred

charges of the anion insertion process and the measured overall anodic value corresponds to the charge of the polymerisation reaction ($Q_{pol} = Q_a - Q_{insert}$). The ratio Q_{pol}/Q_a decreases from 45 % to 10 %, indicating that the polymerisation reaction reaches a limit, and the anion insertion process becomes dominant. At the same time, the ratio Q_c/Q_a increases from 54 % to 89 %, which suggest a reversible insertion and removal of $AlCl_4^-$ into PEDOT. [48]

The PEDOT appears as dull dark blue-violet films on the vitreous carbon substrates. The SEM images of the PEDOT surfaces (Figure 18) show the typical porous structure of PEDOT, which consists of agglomerated granules with an average diameter of ≤1 µm [35,87,100]. [48]

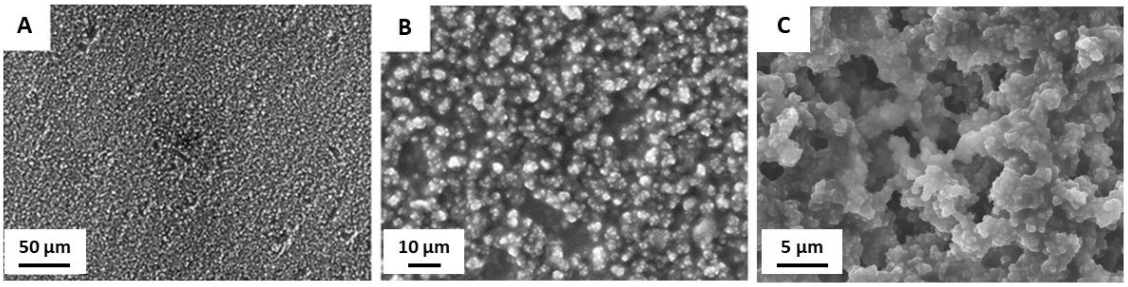

Figure 18: SEM images of PEDOT surfaces at (A-C) increasing magnification obtained in Lewis neutral EMImCl-$AlCl_3$ with 0.1 mol dm^{-3} EDOT from -0.5 V to 2.6 V vs. Al|Al(III) at 100 mV s^{-1}, 20 cycles and 25 °C. [adapted from 48]

5.2.2 Synthesis of PEDOT on 3D Substrates in Ionic Liquid

Once the conductive polymer electrode was successfully electropolymerised in a chloroaluminate ionic liquid and showed stable charging and discharging behaviour [48], the improvement of the polymer capacity was required. A thin film of PEDOT was electropolymerised on three-dimensional reticulated vitreous carbon substrates by cyclic voltammetry and pulsed polymerisation methods from a Lewis neutral chloroaluminate ionic liquid containing EDOT monomer. The polymer composite offers a high active surface area for the redox reaction co-occurring with the anion insertion/removal into the conductive polymer (Figure 19). The structure of the polymer films and their stability in Lewis neutral ionic liquid were characterised by scanning electron microscopy and cyclic voltammetry and compared with films electropolymerised on planar vitreous carbon. [45]

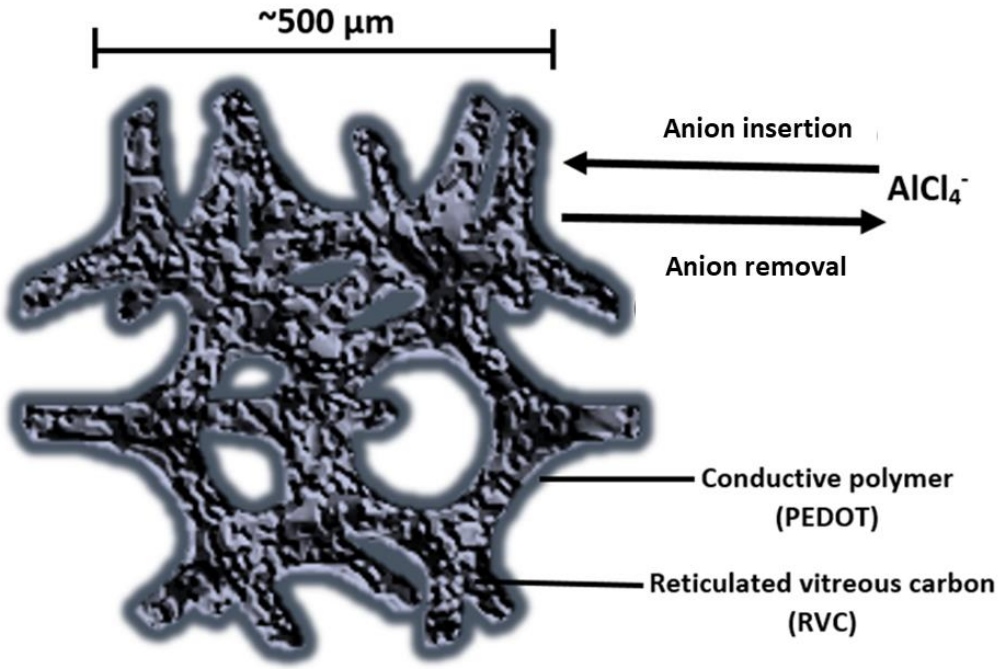

Figure 19: Schematic illustration of the three-dimensional RVC-PEDOT composite with inserting $AlCl_4^-$ ions of a Lewis neutral chloroaluminate ionic liquid. [adapted from 45]

PEDOT was electropolymerised by pulsed potential methods and CV on RVC in Lewis neutral EMImCl-$AlCl_3$. The PEDOT film obtained by RNPV formed irregular shapes on the edges of the RVC struts (Figure 20 A) and on the closest areas of the RVC substrate to the counter electrode (Figure 20 B). [45]

The electropolymerisation by DPA (Figure 20 C) induced the polymer formation in deeper sections of the RVC substrate rather than just on the surface closest to the counter electrode due to the higher applied potentials that can be achieved by the constant higher pulse potential. However, PEDOT was polymerised as thick agglomerated grains with an average grain size of 5 µm only on the edges of the RVC backbone (Figure 20 D). These grains are 5 times larger than PEDOT grains obtained by cyclic voltammetry on the VC. The pulsed potential polymerisation methods do not generate a uniform current distribution on the RVC substrate, and as a result, a preferential polymerisation and polymer growth occur on the edges of the struts, where the current density is higher. [45]

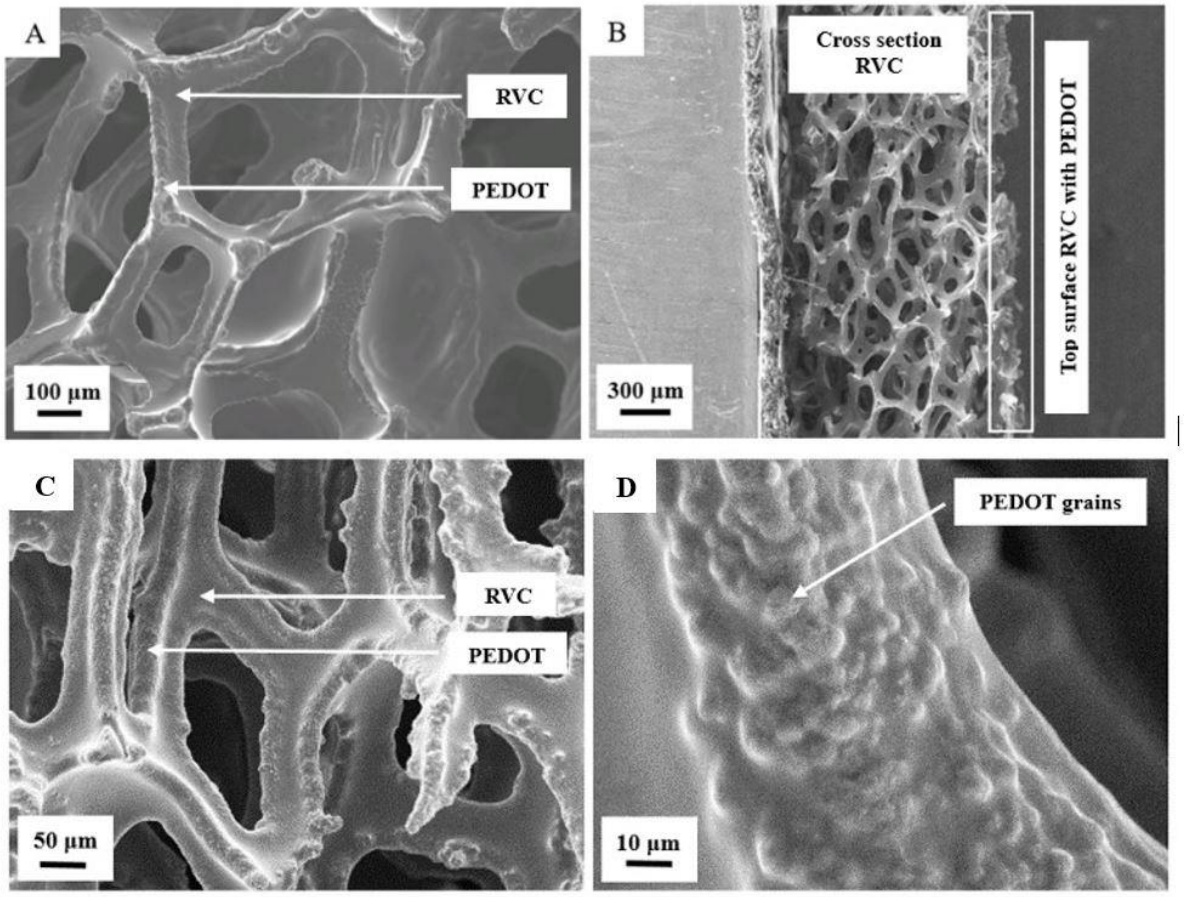

Figure 20: SEM images of PEDOT on reticulated vitreous carbon after electropolymerisation over 200 pulses in Lewis neutral EMImCl-$AlCl_3$ containing 0.1 mol dm^{-3} EDOT by RNPV (A) top view, (B) cross-sectional view and by DPA (C) cross-sectional view lower part RVC substrate and (D) zoom on polymerised edge of the RVC backbone. [45]

The electropolymerisation by CV on bare RVC (Figure 21 A) leads to PEDOT films with the same porous structure and with an average grain diameter of ≤1 µm (Figure 21 B-E) similar to those obtained on VC under the same conditions. The cross-sectional areas (Figure 21 D and Figure 21 E) show that PEDOT films polymerise uniformly on the whole RVC substrate. The polymer has an overall film thickness up to 3 µm, whereas the granular structure grows on an initial thin planar PEDOT layer of ~200 nm thickness. [45]

After 250 anion insertion/removal cycles in monomer-free Lewis neutral EMImCl-$AlCl_3$, the PEDOT film shows no significant structural changes (Figure 21 F-H). The SEM images demonstrate the high stability of PEDOT films on the macro-porous backbone of the RVC in the imidazolium-based chloroaluminate ionic liquid. [45]

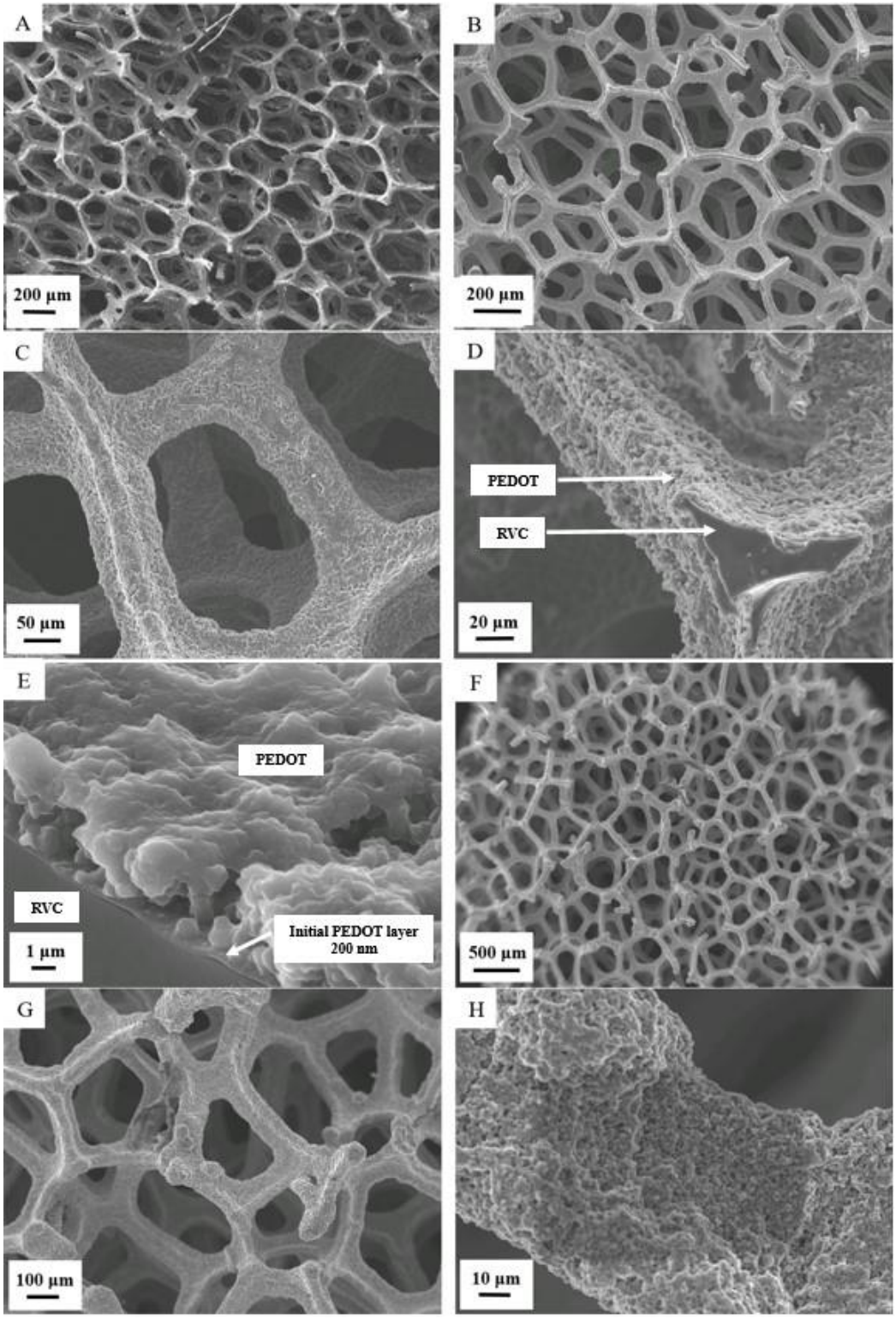

Figure 21: SEM images of (A) bare reticulated vitreous carbon, (B) and (C) PEDOT on reticulated vitreous carbon surface, (D) and (E) cross-sectional area after electropolymerisation by cyclic voltammetry in Lewis neutral EMImCl-$AlCl_3$ containing 0.1 mol dm^{-3} EDOT and (F-H) after 250 cycles in monomer-free Lewis neutral EMImCl-$AlCl_3$. [45]

5.3 Electrode Characterisation in Ionic Liquid

Half-cell studies of PEDOT polymerised in Lewis neutral chloroaluminate ionic liquid, and metallic aluminium were performed by cyclic voltammetry and scanning electron microscopy. In addition, mechanistic characterisations of the polymer behaviour depending on the state of charge were investigated by electrochemical quartz crystal microbalance measurements, in-operando atomic force microscopy and electrochemical impedance spectroscopy.

5.3.1 Characterisation of PEDOT in Ionic Liquid

The half-cell behaviour of PEDOT was studied in monomer-free Lewis acidic, basic and neutral ionic liquid by cyclic voltammetry (Figure 22). Each ionic liquid composition has a clear stability window (Figure 14) and contains different predominant anions (Table 2) which influence the polymer behaviour, especially the formation of anion insertion and removal sites. The PEDOT films were previously electropolymerised on planar vitreous carbon in Lewis neutral EMImCl-$AlCl_3$ with 0.1 mol dm^{-3} EDOT by cyclic voltammetry for 20 cycles, at 100 mV s^{-1} and 25 °C. [48]

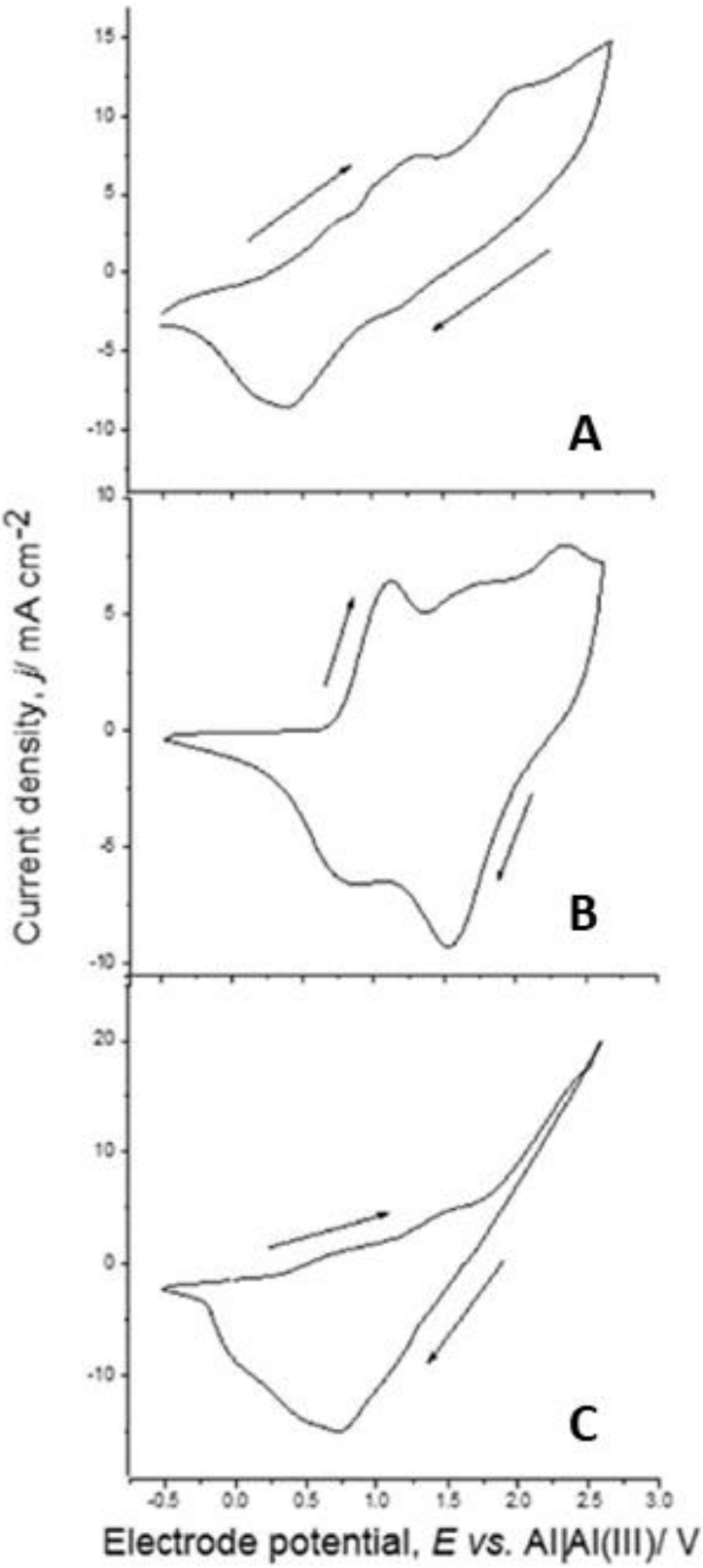

Figure 22: Cyclic voltammograms of PEDOT films in monomer-free Lewis (A) acidic (cycle 7), (B) neutral (cycle 15) and (C) basic (cycle 7) EMImCl-$AlCl_3$ at 100 mV s^{-1} and 25 °C. [48]

The cyclic voltammogram of the PEDOT film in Lewis acidic ionic liquid (Figure 22 A) shows three anodic peaks (anion insertion processes) at 0.5 V, 1.5 V and 2 V as well as two cathodic peaks (anion removal processes) at 1.2 V and 0.8 V *vs.* Al|Al(III). The inserting anions in this Lewis acidic ionic liquid are $AlCl_4^-$ and $Al_2Cl_7^-$, showing an insertion/removal reversibility (Q_c/Q_a) of 43 % into the polymer film. On the PEDOT surface, a viscous and dark orange-brown film was formed after a few cycles. The colour and consistency of the film were comparable with Lewis acidic EMImCl-$AlCl_3$ solution with EDOT (Figure 6 C). It is assumed that this viscous film increased the electrolyte resistance, which was observed as the increasing slope of the cyclic voltammogram. [48]

The PEDOT film in Lewis neutral EMImCl-$AlCl_3$ (Figure 22 B) shows one pair of anion insertion and removal peaks at higher potentials. There are two clear separated anion removal peaks at 1.6 V and 0.8 V *vs.* Al|Al(III). The peak at ~0.8 V *vs.* Al|Al(III) was observed for all PEDOT films characterised in Lewis acidic, basic and neutral EMImCl-$AlCl_3$. The anion insertion peaks in the Lewis neutral composition appear at 1.2 V, 1.7 V and 2.3 V *vs.* Al|Al(III). [48]
The anodic peak at 1.2 V *vs.* Al|Al(III) describes the formation of anion insertion sites at a lower state of charge, whereas the anodic peak at 1.7 V *vs.* Al|Al(III) shows anion insertion at an intermediate state of charge. The increase of the anion insertion with increasing state of charge due to oxidation enables a consequently higher degree of inserted anions [48,49]. The anodic peak at 2.3 V *vs.* Al|Al(III) is the maximum value for PEDOT in Lewis neutral EMImCl-$AlCl_3$. An even higher anodic potential of PEDOT cannot be investigated in this solution. A further increase of the anodic potential would cause the decomposition (≥2.6 V *vs.* Al|Al(III)) of the Lewis neutral ionic liquid and degradation of the PEDOT film. [48,49]

The PEDOT film in Lewis basic EMImCl-$AlCl_3$ (Figure 22 C) is characterised by a wide cathodic peak at ~0.8 V *vs.* Al|Al(III) with 157 mAs transferred charge of removed anions. In contrast, the transferred charges of inserted anions are 29 mAs between around 0.8 V and 1.5 V *vs.* Al|Al(III). The cyclic voltammogram indicates that the anion removal is dominant, pointing to an inefficient anion insertion/removal of both the Cl^- ions of the Lewis basic ionic liquid and $AlCl_4^-$ ions inserted in the previously polymerised PEDOT film. The viscosity of the Lewis basic composition (~306 mPa s at 20.7 °C [101]) is 27 and 19 times higher than a Lewis acidic (~11.5 mPa s at 20.0 °C [101]) and Lewis neutral composition (~16 mPa s at 20.0 °C [101]),

respectively. Therefore, the anion insertion might be mass transport controlled. Furthermore, the PEDOT film shows low stability at high anodic potentials. The decomposition starts already at 1.8 V *vs.* Al|Al(III). [48]

It can be concluded that PEDOT films in Lewis neutral EMImCl-$AlCl_3$ are more useful for batteries because of the formation of anion insertion/removal sites at higher potentials, providing higher cell potentials in the battery. [48]

5.3.1.1 Formation of Anion Insertion and Removal Sites

The formation of anion insertion and removal sites in the polymer was studied by cycling and increasing the anodic polymerisation potential window in monomer-free Lewis neutral EMImCl-$AlCl_3$ from -0.5 V to 2.6 V *vs.* Al|Al(III). This experiment refers to the question of whether the anion insertion/removal sites of the conductive polymer are predefined during the electropolymerisation or whether the sites are formed during cycling in the monomer-free ionic liquid electrolyte in the presence of insertion anions. [48]

The cyclic voltammograms of the electropolymerisation obtained from -0.5 V to 1.5 V (Figure 23 A), 2.0 V (Figure 23 B) and 2.6 V (Figure 23 C) *vs.* Al|Al(III) show an increasing amount of anion insertion and removal sites. PEDOT polymerised from -0.5 V to 1.5 V *vs.* Al|Al(III) is characterised by one clear anion insertion site at 0.85 V and removal site at 0.8 V *vs.* Al|Al(III), whereas PEDOT obtained from -0.5 V to 2.0 V *vs.* Al|Al(III) shows merged insertion sites without clear peaks between 0.8 V and 1.8 V and removal sites between 1.6 V and 0.3 V *vs.* Al|Al(III). PEDOT polymerised in the widest polymerisation window from -0.5 V to 2.6 V *vs.* Al|Al(III) has four anion insertion sites at 0.75 V, 1.1 V, 1.7 V and 2.2 V *vs.* Al|Al(III) which overlap each other and two clear removal sites at 1.6 V and 0.9 V *vs.* Al|Al(III). [48]

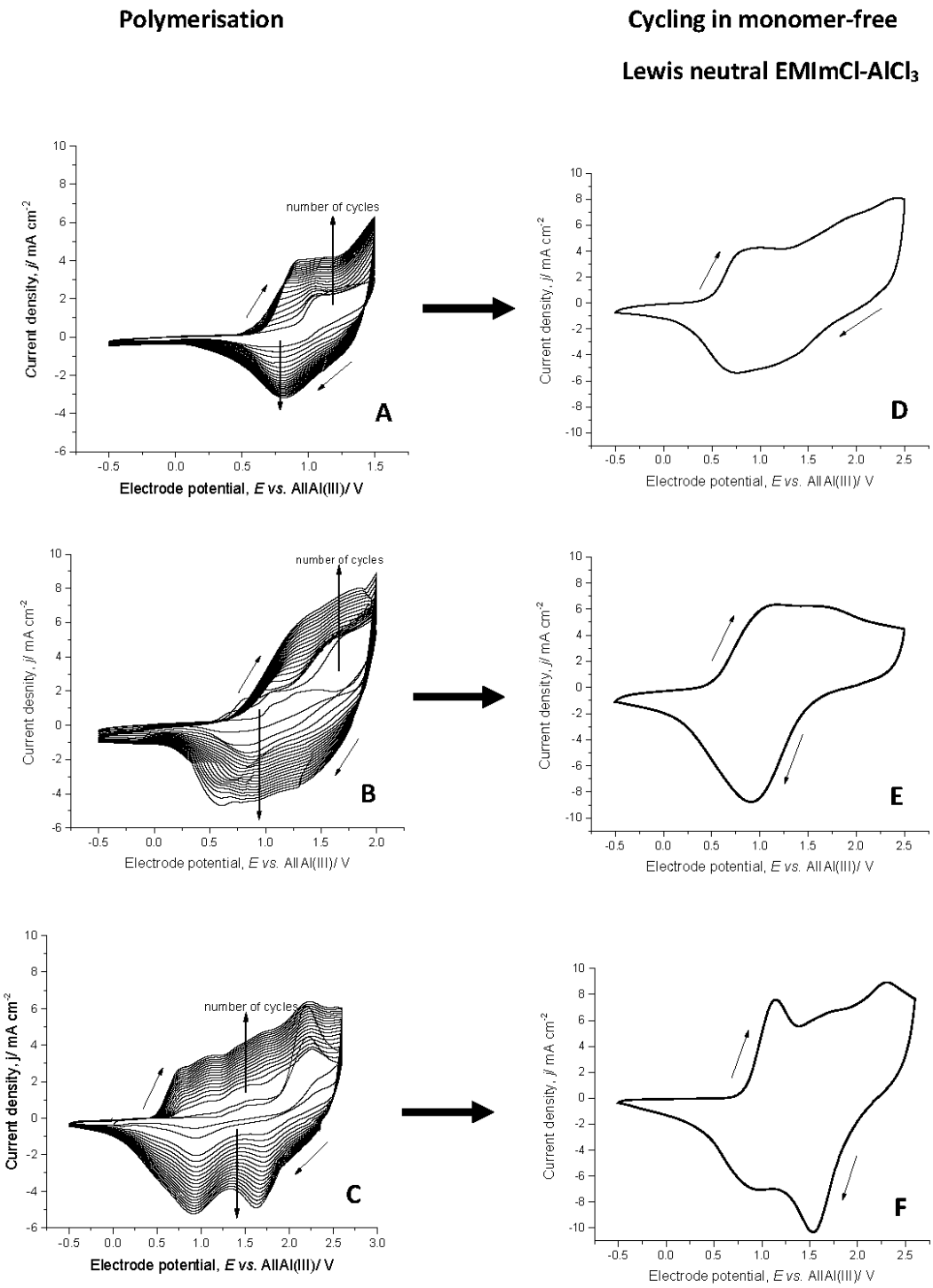

Figure 23: Cyclic voltammograms of PEDOT films polymerised from -0.5 V to (A) 1.5 V, (B) 2.0 V and (C) 2.6 V vs. Al|Al(III) in Lewis neutral EMImCl-$AlCl_3$ with 0.1 mol dm^{-3} EDOT at 20 cycles. Cyclic voltammograms of PEDOT films polymerised to (D) 1.5 V, cycle 15, (E) 2.0 V, cycle 7 and (F) 2.6 V, cycle 15 in monomer-free Lewis neutral EMImCl-$AlCl_3$ from -0.5 V to 2.6 V vs. Al|Al(III) at 100 mV s^{-1} and 25 °C. [adapted from 48]

The PEDOT film obtained from -0.5 V to 1.5 V *vs.* Al|Al(III) (Figure 23 A) shows, in monomer-free Lewis neutral EMImCl-$AlCl_3$, from -0.5 V to 2.6 V *vs.* Al|Al(III) (Figure 23 D) the same anion insertion/removal sites observed already during polymerisation plus an additional insertion wave at 1.75 V *vs.* Al|Al(III). The anion insertion/removal sites in monomer-free Lewis neutral EMImCl-$AlCl_3$, when PEDOT polymerised from -0.5 V to 2.0 V *vs.* Al|Al(III) (Figure 23 E), have the same anodic potential window comparable to the polymerisation (Figure 23 B). However, the anion removal site appears as a wide but clear peak at 0.9 V *vs.* Al|Al(III) in the monomer-free ionic liquid. The PEDOT film obtained from -0.5 V to 2.6 V *vs.* Al|Al(III) (Figure 23 C) shows three anion insertion sites at 0.5 V, 1.5 V and 2 V as well as two anion removal sites at 1.2 V and 0.8 V *vs.* Al|Al(III) (Figure 23 F). [48]

The PEDOT films characterised in monomer-free Lewis neutral EMImCl-$AlCl_3$ clearly show that the anion insertion and removal sites are predefined during electropolymerisation. Anion insertion or removal sites of PEDOT films in the monomer-free ionic liquid, at a higher potential than the initial polymerisation potential window, were not observed. The characteristic anion insertion and removal sites are similar to the sites, formed during polymerisation in a specific polymerisation potential window. Additional insertion sites are not formed during cycling in monomer-free Lewis neutral EMImCl-$AlCl_3$. [48]

The polymerisation potential window also has a clear influence on the density of the agglomerated granules. The PEDOT film obtained at the lowest polymerisation potential window from -0.5 V to 1.5 V *vs.* Al|Al(III) shows the lowest granule density (Figure 24 A and Figure 24 D). The increase of the polymerisation potential window to 2.0 V (Figure 24 B and Figure 24 E) and 2.6 V *vs.* Al|Al(III) (Figure 24 C and Figure 24 F) causes an increase of the granule density. [48]

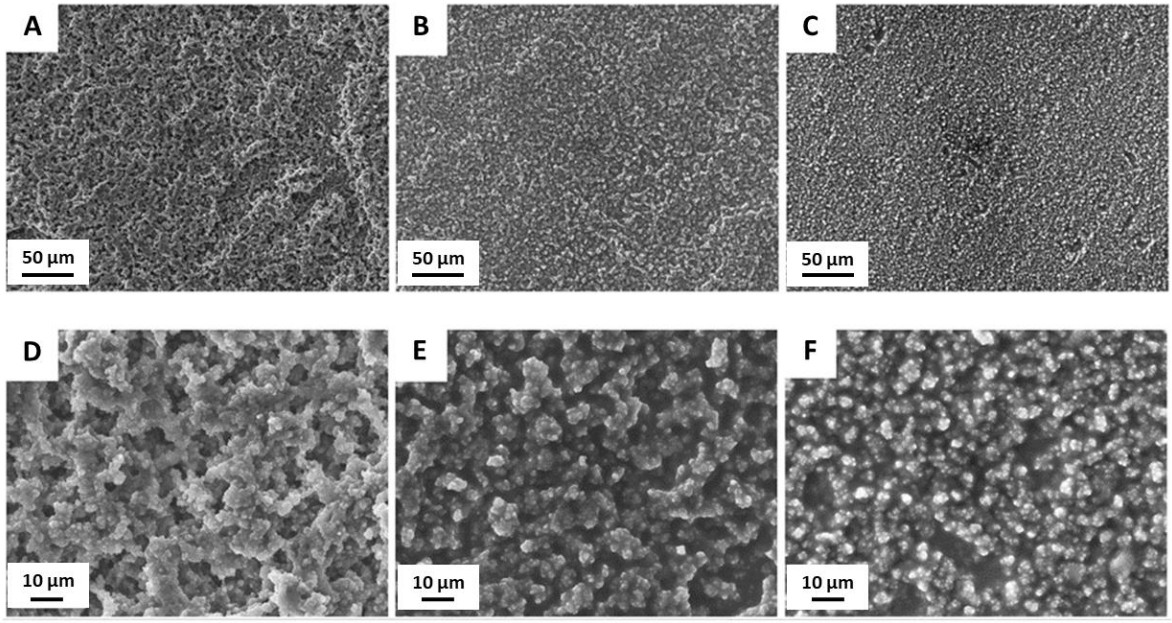

Figure 24: SEM images of PEDOT surfaces at (A,B,C) 1000-fold and (D,E,F) 5000-fold magnification obtained in Lewis neutral EMImCl-$AlCl_3$ with 0.1 mol dm^{-3} EDOT from -0.5 V to (A,D) 1.5 V, (B,E) 2.0 V and (C,F) 2.6 V vs. Al|Al(III) at 100 mV s^{-1}, 20 cycles and 25 °C. [48]

The increase of grain density results from the growth of the chain length of PEDOT with a wider polymerisation potential window [49], forming a cross-linked network of polymer chains. It is assumed that a highly cross-linked polymer network generates more accessible anion insertion sites for $AlCl_4^-$, which are accessible at higher potentials. [48]

5.3.1.2 Stability of PEDOT in Ionic Liquid

A similar PEDOT film electropolymerised by cyclic voltammetry in Lewis neutral EMImCl-$AlCl_3$ containing 0.1 mol dm^{-3} EDOT from -0.5 V to 2.5 V with 100 mV s^{-1} on planar vitreous carbon was cycled 500 times in monomer-free Lewis neutral EMImCl-$AlCl_3$ (Figure 25). [45]

The redox reaction of the polymer reaction (Q_c/Q_a) reaches a minimum coulombic efficiency of 97 % within 500 cycles, considering the overall cathodic and anodic transferred charges. This high reversibility demonstrates that the inserting anion $AlCl_4^-$ does not remain trapped in the conductive polymer, proving that there is good accessibility to the anion insertion sites in the polymer during oxidation. Furthermore, a detachment of the polymer film from the substrate was not observed. The good

reversibility and adhesion to the substrate make in ionic liquid electropolymerised PEDOT suitable as a charge storage material in batteries. [45]

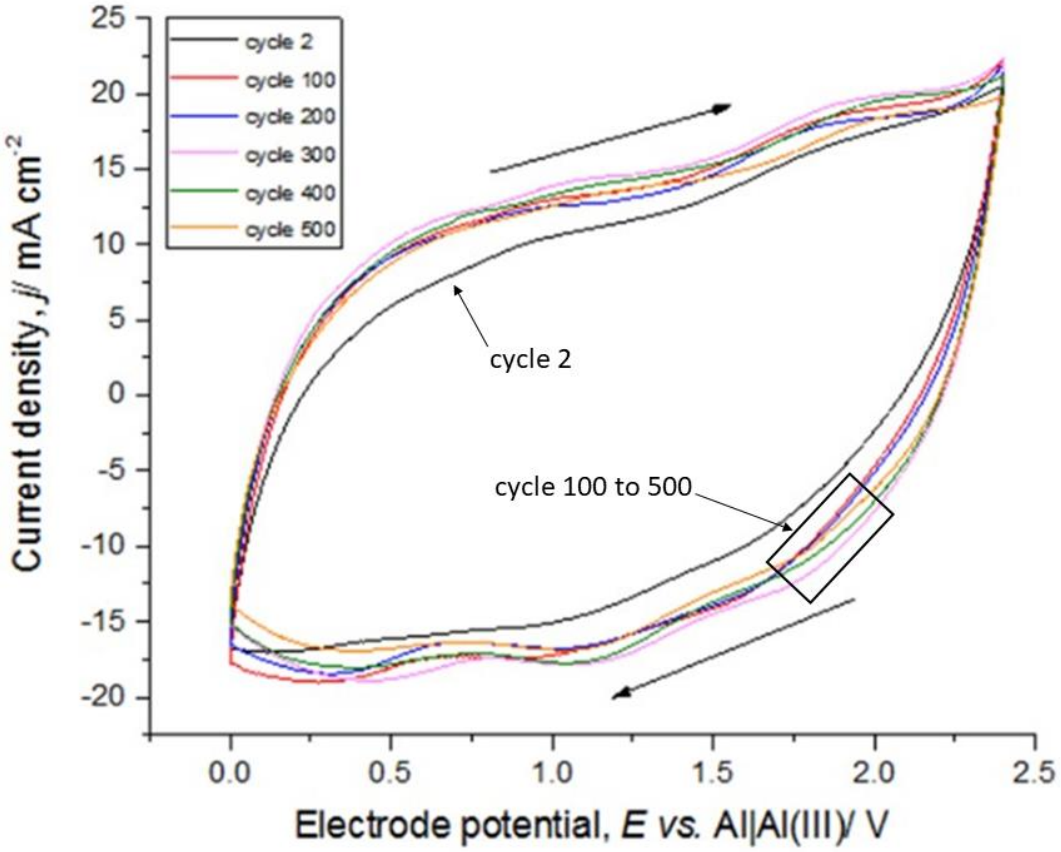

Figure 25: Cyclic voltammogram of a PEDOT film on a 0.8 cm^2 area vitreous carbon disc, from 0 V to 2.5 V vs. Al|Al(III) at 100 mV s^{-1}. Cycles: 2nd (black line), 100th (red line), 200th (blue line), 300th (violet line), 400th (green line) and 500th (orange line) cycle in monomer-free Lewis neutral EMImCl-$AlCl_3$. The PEDOT film was previously polymerised in Lewis neutral EMImCl-$AlCl_3$ containing 0.1 mol dm^{-3} EDOT from -0.5 V to 2.5 V vs. Al|Al(IIII) at 100 mV s^{-1}, during 20 cycles and 25 °C. [45]

5.3.1.3 Comparison of PEDOT on 2D and 3D Vitreous Carbon

The characteristics of PEDOT films obtained by CV in Lewis neutral EMImCl-$AlCl_3$ from -0.5 V to 2.5 V with 100 mV s^{-1} at 25 °C on planar (2D) vitreous carbon were compared with those polymerised on reticulated (3D) vitreous carbon (Figure 26). [45]

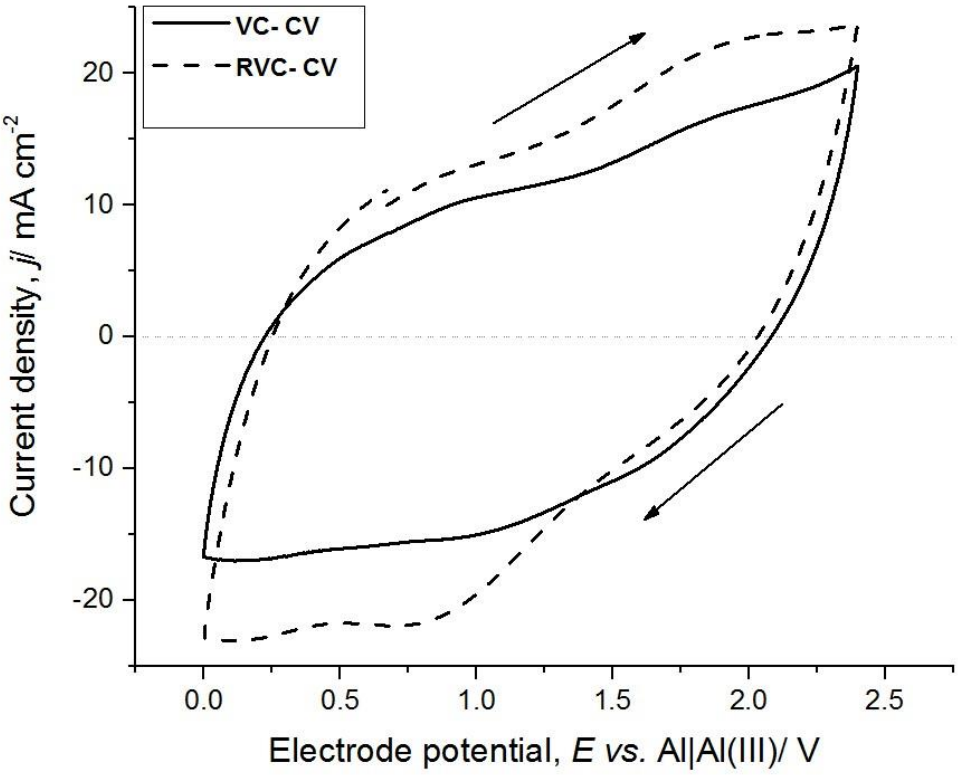

Figure 26: Cyclic voltammogram of PEDOT films from 0 V to 2.5 V vs. Al|Al(III) with 100 mV s^{-1} at 2nd cycle and 25 °C in monomer-free Lewis neutral EMImCl-$AlCl_3$. PEDOT films polymerised on planar vitreous carbon (VC) by cyclic voltammetry (solid line) and on reticulated vitreous carbon (RVC) by cyclic voltammetry (dashed line). [45]

The PEDOT film polymerised on RVC by cyclic voltammetry shows a clearer formation of the anion insertion/removal sites (oxidation/reduction waves) in comparison to PEDOT films on planar vitreous carbon. Furthermore, the obtained PEDOT film capacity on RVC (1035 mAs) is about 45 % higher than the capacity calculated for planar films (455 mAs), whereas the coulombic efficiency of the anion insertion/removal process is similar for the polymer films on both substrates at 94 %. [45]

5.3.1.4 Characteristics of PEDOT Depending on the State of Charge

The following investigations identify the relation of polymer morphology, nanomechanical and viscoelastic changes depending on the state of charge of the PEDOT electrode. It is assumed that conductive polymers, such as PEDOT, undergo a morphological and structural change with every charge/discharge cycle by polymer swelling and contraction [36]. These changes have a significant influence on the polymer characteristics and consequently on the

performance as a battery material. These studies provide information about the anion insertion/removal process of the conductive polymer while charging/discharging and associated capacitive, as well as faradaic behaviour, depending on the state of charge/discharge by CV coupled with EQCM measurements and EIS [36]. In-operando AFM measurements will show the morphological change of the polymer surface while charging and discharging. The combination of these results draws a conclusion on how morphology determines the battery and capacitor characteristics of PEDOT. [36]

5.3.1.4.1 Viscoelastic Changes

The PEDOT films electropolymerised in Lewis neutral ionic liquid on an oscillating gold quartz crystal of an electrochemical quartz crystal microbalance were cycled in monomer-free Lewis neutral EMImCl-$AlCl_3$ by CV. At the same time, the change of frequency and damping of the quartz crystal were recorded. [36]

The overall frequency and damping change (Figure 27 A) remain approximately constant over time during all measured cycles. The decrease of the resonance frequency indicates anion insertion during polymer oxidation/charging, whereas the increase shows the anion removal during reduction/discharging. The damping change is significantly larger than the frequency change, making the quantitative determination of the exchanged mass more complicated, as the Sauerbrey equation (Equation 8) cannot be applied. [36]

The real part of the shear modulus (Figure 27 B) shows an overall decrease, indicating a slight increase of the polymer softness with time. Every charging cycle shows a clear decrease while an increase of the shear modulus characterises every discharging cycle. Thus, the anion insertion (charging reaction) causes a softening of the polymer film, which regains its stiffness when the anions are removed (discharge reaction). [36]

The thickness of the PEDOT film (Figure 27 C) fluctuates about ±45 nm from its average value of 340 nm during charging and discharging, indicating polymer swelling (increased film thickness) during anion insertion and contraction (decreased film thickness) during removal of $AlCl_4^-$ anions. There is nearly no net mass change of the polymer film during the cycling (Figure 27 C). The mass of the polymer increases when anions are inserted into the film and

decreases when anions are removed. The PEDOT film reaches reversibility in terms of the anion insertion/removal >95 %. Therefore, the inserting anion $AlCl_4^-$ is not trapped in the polymer backbone during charging and discharging. [36]

The electropolymerised PEDOT film has a correction factor *b* (Figure 27 D) between 2.0 and 2.6 (definition in Paragraph 4.3.1.2.1), indicating a very rough surface area [90]. Assuming that meaningful values were used for the physical properties of the system, these values are two to three times larger than those reported for aqueous systems (b ~ 0.8) [56] due to the stronger interaction of PEDOT with the insertion anion $AlCl_4^-$, the insertion of which is not hindered by hydrate shielding as it is when electropolymerised in an aqueous electrolyte. [36]

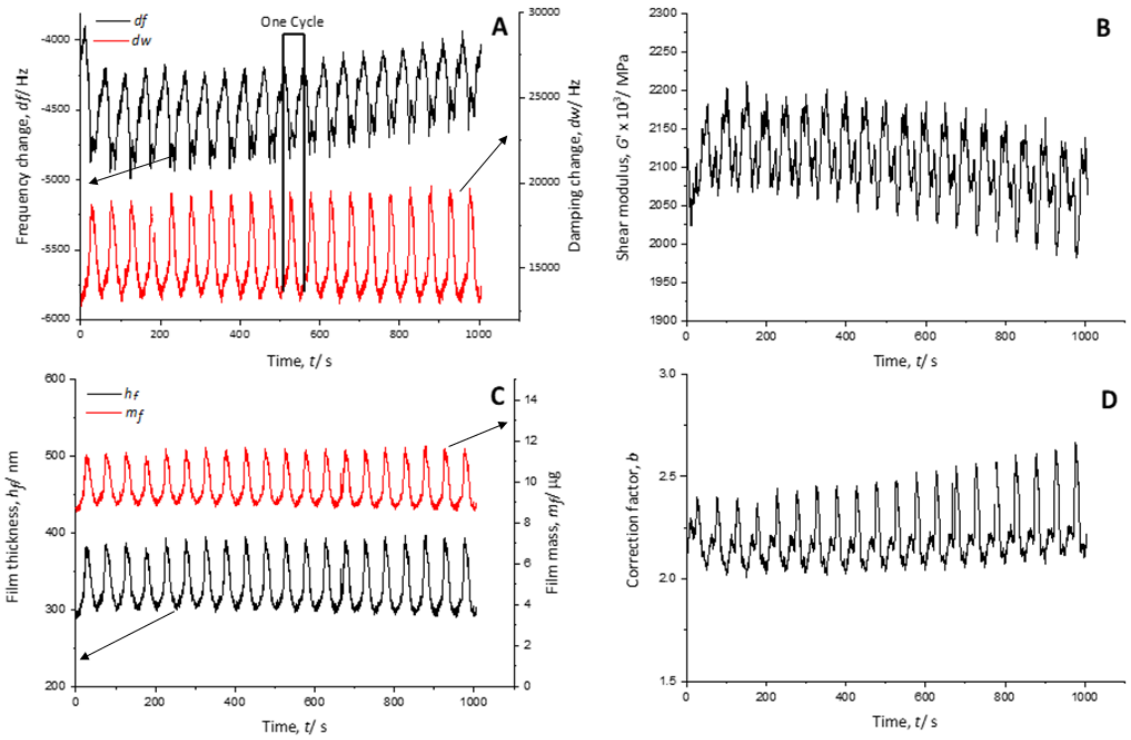

Figure 27: (A) Frequency (black line) and damping (red line) change of a gold-coated quartz crystal, (B) calculated shear modulus (real part), (C) polymer film thickness (black line) and mass (red line) and (D) correction factor during the cycling of PEDOT in monomer-free Lewis neutral EMImCl-$AlCl_3$ from 0 V to 2.5 V vs. Al|Al(III), 100 mV s^{-1}, 25 °C. [36]

Each charging and discharging cycle can be divided into four potential areas with different behaviour shown by cyclic voltammetry (Figure 28 A), the change of resonance frequency (Figure 28 B) and the calculated shear modulus (Figure 28 C) as shown for cycle 10. [36]

Oxidation potential window I (0 V - 0.5 V):

At the beginning of the polymer charging (oxidation) from 0 V to 0.5 V *vs.* Al|Al(III), the current density increases slightly. The frequency change also shows only a slight increase, which implies no significant ion insertion or removal. The shear modulus shows a clear decrease, indicating a softening of the polymer. [36]

Oxidation potential window II (0.5 V - 1.5 V):

The next potential window, from 0.5 V to 1.5 V *vs.* Al|Al(III) shows a broad oxidation peak of PEDOT, indicating the generation of positive charges in the polymer backbone. The frequency change reaches a maximum after a slight increase but shows no anion insertion yet. The shear modulus decreases further up to its minimum. Thus, the polymer is softest in this potential range. [36]

Oxidation potential window III (1.5 V – 2.1 V):

Further oxidation from 1.5 V to 2.1 V *vs.* Al|Al(III) shows another oxidation peak of PEDOT. At this potential window, the resonance frequency decreases significantly, which is a clear indication of anion insertion. The shear modulus increases slightly, indicating a stiffening of the polymer backbone due to a large number of anions entering the polymer structure. [36]

Oxidation potential window IV (2.1 V - 2.5 V):

The last potential window from 2.1 V to 2.5 V *vs.* Al|Al(III) is characterised by a phase-out of the oxidation peak and a further significant decrease of the resonance frequency, showing a clear anion insertion. The polymer softens once again as the shear modulus decreases. [36]

Reduction potential window IV (2.5 V - 2.1 V):

The discharge reaction (towards reduction) shows that the current density decreases and the resonance frequency increases strongly, indicating the reverse anion removal from the film. The shear modulus decreases further, which might be related to the enhanced anion movement in the polymer backbone, opening the paths between the polymer chains due to the removal of the anions. [36]

Reduction potential window III (2.1 V - 1.5 V):

The current density decreases almost linearly from 2.1 V to 1.5 V *vs.* Al|Al(III). Furthermore, there is practically no change in resonance frequency, indicating no significant anion removal. However, the polymer is stiffening as the shear modulus increases. [36]

Reduction potential window II (1.5 V - 0.5 V):

The potential window from 1.5 V to 0.5 V *vs.* Al|Al(III) shows a reduction peak of PEDOT, indicating the removal of repulsive forces between the polymer chains. This leads to the contraction of the polymer paths, accompanied by anion removal shown by increasing resonance frequency and further stiffening of the polymer as the shear modulus rises up to a maximum. [36]

Reduction potential window I (0.5 V - 0 V):

The current density increases from 0.5 V to 0 V *vs.* Al|Al(III) and the frequency change is almost constant, showing that the anion removal is completed. The shear modulus increases again to its initial value, indicating it has regained the original stiffness of the polymer. [36]

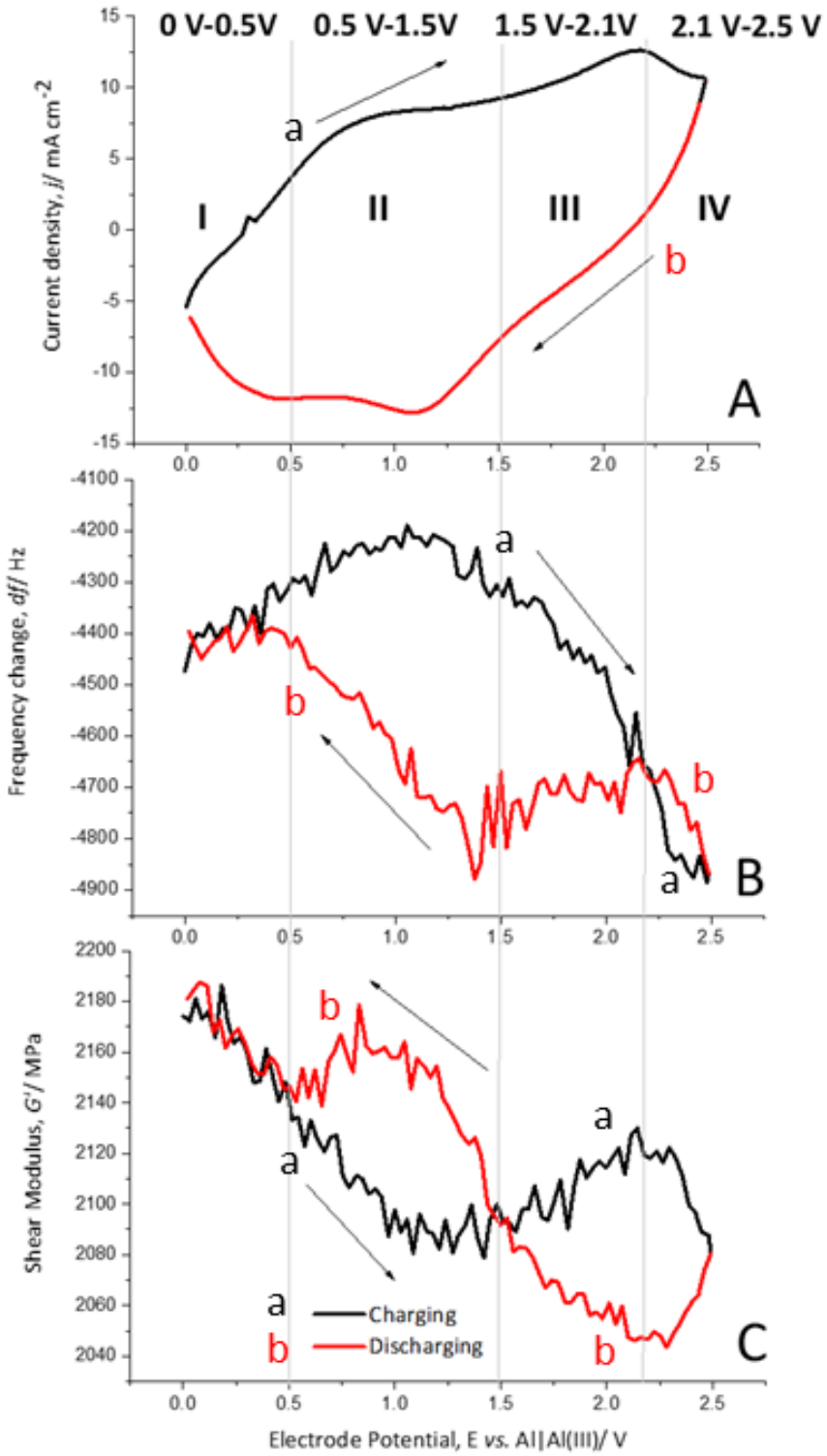

Figure 28: (A) Cyclic voltammogram, (B) frequency change of a gold-coated quartz crystal, (C) calculated shear modulus (real part) of the polymer film during charging (a; black lines) and discharging (b; red lines) of PEDOT in monomer-free Lewis neutral EMImCl-$AlCl_3$ from 0 V to 2.5 V vs. Al|Al(III) at cycle 10, 100 mV s^{-1} at 25 °C. [36]

5.3.1.4.2 Morphological Changes

In-operando AFM measurements of PEDOT films in monomer-free Lewis neutral chloroaluminate ionic liquid provide information about the morphological changes of the polymer surface during charging/discharging (anion insertion/removal) cycles. [36]

PEDOT polymerised in Lewis neutral chloroaluminate ionic liquid appears very porous and granular (Figure 29) in its uncharged state. The agglomerated grains have an average size of 100 nm, and the maximum height difference between the agglomerated areas reaches up to 1 µm (Figure 29) (brighter areas have a larger height). The average surface roughness R_a is between 180 and 190 nm. [36]

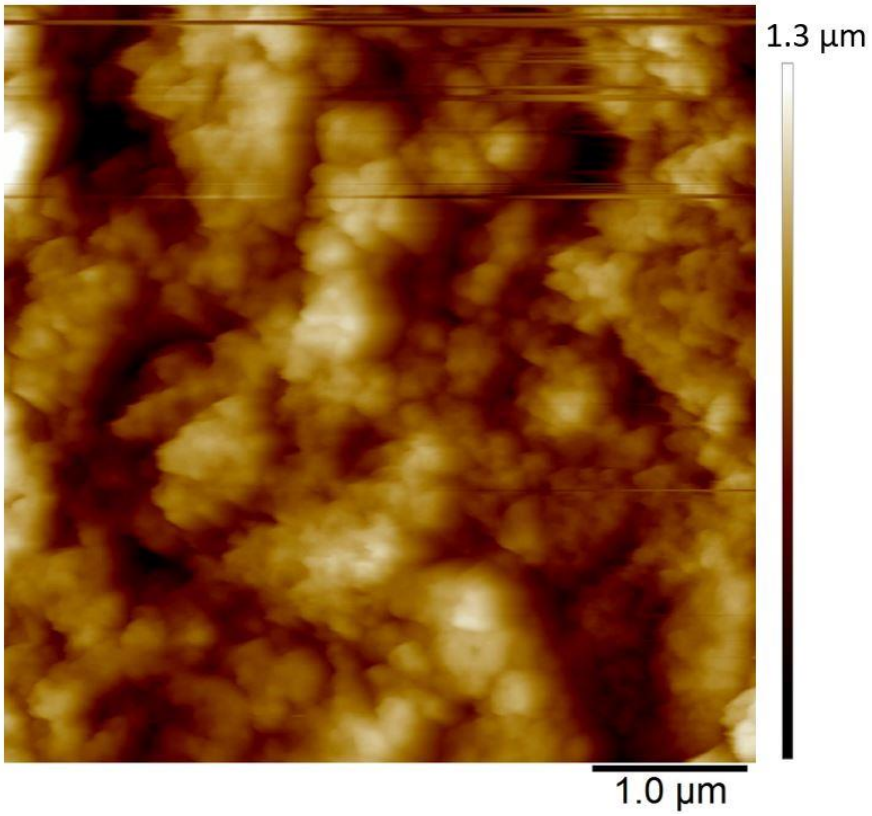

Figure 29: Initial state AFM image of uncharged PEDOT in monomer-free Lewis neutral EMImCl-$AlCl_3$. PEDOT was polymerised by CV from -0.5 V to 2.5 V vs. Al|Al(III) in Lewis neutral EMImCl-$AlCl_3$ with 0.1 mol dm^{-3} EDOT at 100 mV s^{-1}, 20 cycles and 25 °C. [36]

The polymer surface also shows local differences in terms of deformability (Figure 30) in the uncharged state. It has been shown that PEDOT grows as vertically aligned granular pillars (Figure 21 E), which are directly connected to the substrate. These pillars, which appear as grains on the surface (Figure 30 A), are partially connected horizontally by a granular polymer

layer. This layer has no direct contact to the substrate and is visible as stretched areas (Figure 30 A) [45]. The stretched areas are caused by the strong force applied between the tip and the polymer surface, which is required to measure the deformability. It is assumed that the polymer pillars have lower deformability due to the direct contact with the substrate and appear as darker areas (Figure 30 B) and the brighter areas with higher deformability can be led back to horizontally connecting polymer layers (Figure 30 B). [36]

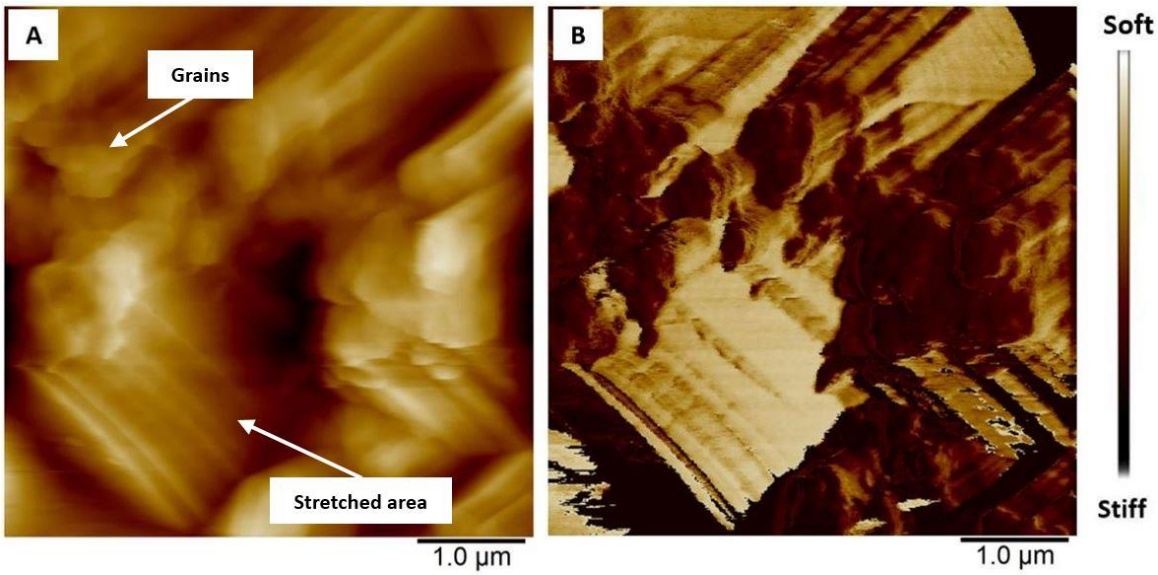

Figure 30: AFM images showing differences in (A) height and (B) deformability of uncharged PEDOT in monomer-free Lewis neutral EMImCl-$AlCl_3$. [36]

During the charging of PEDOT (Figure 31 A-E), the polymer oxidation and anion insertion process causes the merging of the polymer granules. Conversely, during discharging (Figure 31 F-J), the polymer reduces, and the anion removal process takes place. This is characterised by a renewed separation of the granules, whereas the grain shape and position are not identical with the previous grain morphology before the charging reaction. Four areas indicated by squares a, b, c, and d (Figure 31) demonstrate the morphological changes and the merging of the granules and the reversible separation. The newly emerged grains have approximately the same size (~100 nm) as the initial grains. Most areas show the recovery of the initial morphology. However, area d seems not to regain its initial surface morphology after discharging. The overall surface roughness *Rq* decreases from 180 to 190 nm down to ~160 nm during charging and increases during discharging again up to ~180 nm, which indicates high morphological reversibility during cycling. [36]

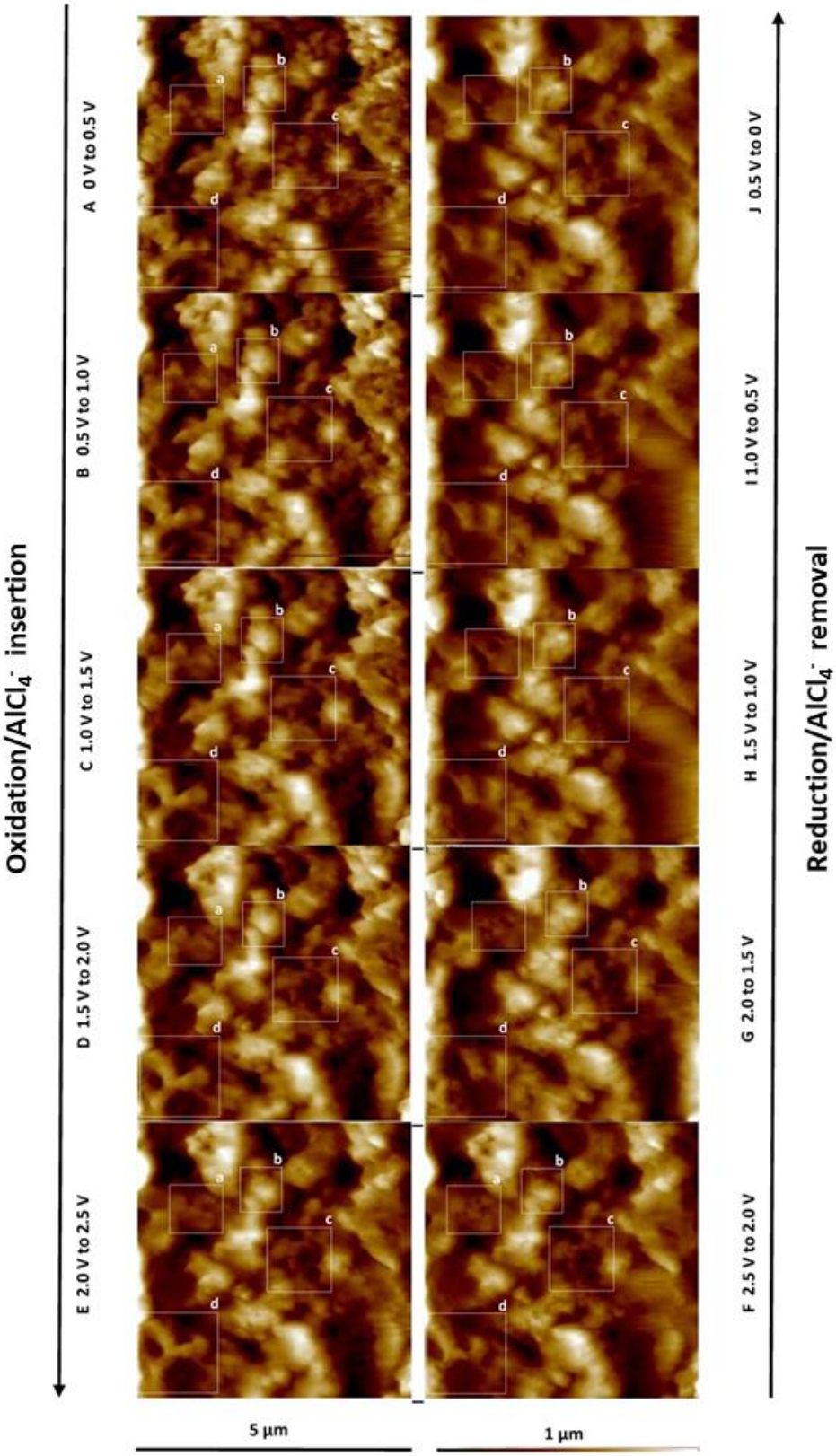

Figure 31: AFM images at different states of charge (A-E) and discharge (F-J). The squared areas (a-d) show morphological surface changes of the PEDOT in detail. [36]

5.3.1.4.3 Impedance Response

The EIS spectra are shown both as Nyquist and Bode plots depending on the state of charge of PEDOT in monomer-free Lewis neutral EMImCl-$AlCl_3$.

5.3.1.4.3.1 Discussion of the Nyquist Plot

The Nyquist plots (Figure 32) show a semi-circle at high frequencies beginning at 100 kHz and a Warburg impedance at lower frequencies beginning around 1 kHz for all states of charge. It indicates that the electrode process is controlled by electrochemical reactions at high frequencies and by mass transfer at low frequencies. At a low state of charge between 0 V and 0.5 V *vs.* Al|Al(III) the electrode process is limited by semi-infinite diffusion (faradaic behaviour). The higher state of charge from 1.0 V to 2.0 V *vs.* Al|Al(III) is dominated by a surface-limited process such as the adsorption of anions at a surface (pseudo-capacitive-like behaviour). The semi-circles are more pronounced when the anion insertion occurs between 0.5 V and 2.0 V *vs.* Al|Al(III) (Paragraph 5.3.1.4.1). This is also characteristic for kinetic control by an electrochemical charge transfer step. The circles are followed by Warburg diffusion diverting from the linear 45° line. The Warburg diffusion lines at 1.0 V and 1.5 V *vs.* Al|Al(III) approach 90° around 3 kHz, associated with the generation of a (pseudo)-capacitive-like effect. This shows that the polymer is oxidised and simultaneously, anions are being inserted into the polymer backbone. The charge transfer takes place at the polymer surface and in pores filled [45] with electrolyte, causing a deviation of the Warburg impedance from linear diffusional behaviour.

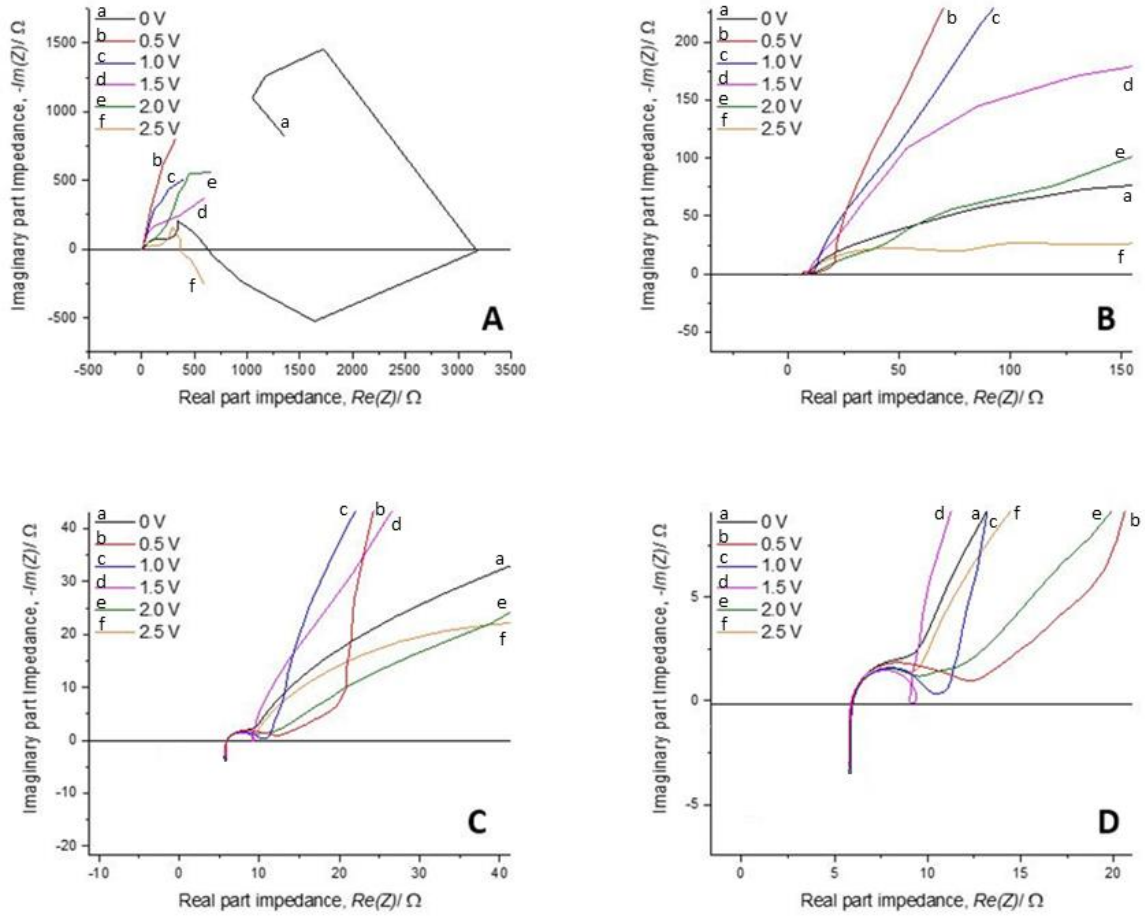

Figure 32: Nyquist plots with increasing magnification from (A) to (D) of PEDOT in monomer-free Lewis neutral EMImCl-$AlCl_3$ depending on the state of charge from 0 V to 2.5 V vs. Al|Al(III) at a frequency range from 1 mHz to 500 kHz and 25 °C.

5.3.1.4.3.2 Discussion of the Bode Plot

The Bode plots (Figure 33) represent the phase shift angle *Z* as a function of frequency *f* at an increasing state of charge from 0 V to 2.5 V *vs.* Al|Al(III) of PEDOT in monomer-free Lewis neutral EMImCl-$AlCl_3$. The plots visualise the contributions of capacitive-like and resistive (faradaic) charge transfer, changing with the applied potential.

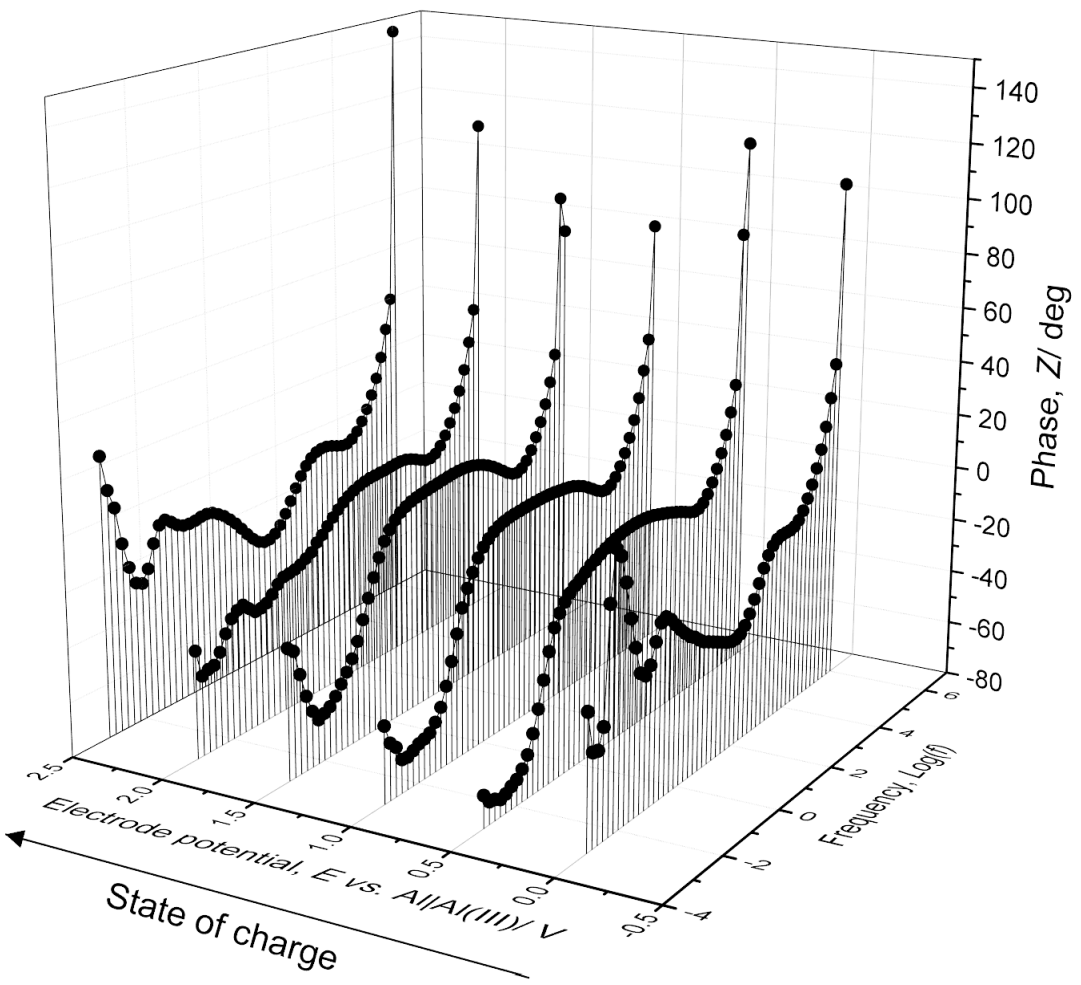

Figure 33: 3D Bode plots of PEDOT in monomer-free Lewis neutral EMImCl-$AlCl_3$ depending on the state of charge from 0 V to 2.5 V vs. Al|Al(III) at a frequency range from 1 mHz to 1 MHz and 25 °C.

PEDOT appears as distinct grains when it is in a completely discharged and electro-neutral state at 0 V *vs.* Al|Al(III) (Paragraph 5.3.1.4.2). At this stage, no anions are inserted in the polymer backbone (Paragraph 5.3.1.4.1). When PEDOT is charged the grains expand and merge into each other, accompanied by the opening of paths between the polymer chains which can be entered by anions of the ionic liquid [36]. At 0.5 V, 1.0 V, 1.5 V and 2.0 V *vs.* Al|Al(III) the phase angle approaches a plateau between 0° and -5° in the frequency region 0.5 Hz to 20 kHz. This indicates diffusion limitation associated with faradaic-like reactions such as the oxidation of PEDOT and the generation of positive charges in the polymer backbone. At lower frequencies, around 1 mHz, the phase angle shows a minimum increasing from -40° to -70° with increasing state of charge from 0.5 V to 2.0 V *vs.* Al|Al(III). It points to a higher resistance

contribution, arising with the simultaneous insertion of anions and formation of a double layer, which causes a capacitive-like charge transfer. The oxidation and insertion of anions occurs from 0.5 V to 2.0 V *vs.* Al|Al(III). The change of the phase angle at the highest state of charge at 2.5 V *vs.* Al|Al(III) appears similar to the curve at the fully discharged state at 0 V *vs.* Al|Al(III). There is no plateau of the phase angle from 0.5 Hz to 20 kHz but a minimum of the phase angle of -40°. When PEDOT is charged, its grains expand and merge into each other, accommodating an increasing number of anions (Paragraph 5.3.1.4.1 and 5.3.1.4.2). The polymer softens when it expands. However, at the highest state of charge, it regains its stiffness partially, indicating that the polymer has expanded to its limits [36]. Therefore, it is assumed that PEDOT is fully saturated with anions and all positive charges in the polymer are compensated at 2.5 V *vs.* Al|Al(III), leading to the impression that PEDOT is in an electro-neutral state like at 0 V *vs.* Al|Al(III). [36]

5.3.1.4.4 Suggested Model of PEDOT Depending on the State of Charge

The previously discussed EQCM and AFM results (Paragraph 5.3.1.4.1 and 5.3.1.4.2) suggest that the change of polymer stiffness/softness, morphology as well as the faradaic and (pseudo)-capacitive behaviour, depending on the state of charge, are related to each other.

The overall charging behaviour of PEDOT is characterised by a swelling and softening of the grainy morphology accompanied by anion insertion. Similarly, the discharging reaction shows the contraction of the polymer grains, which regain their stiffness. A closer look at each charging and discharging cycle reveals that the charge storage mechanisms depend on the state of charge. [36]

Polymer charging (oxidation):

It is known that the oxidation of PEDOT (Figure 34) generates positively charged centres on the monomer units in the polymer backbone [56,57], which appear as waves in the CV (Figure 28 A). During polymer charging, the number of positive charge carriers increases in the polymer backbone, leading to repulsive forces between the charged centres and the polymer chains (Figure 34). This implies a gradual opening of transport paths between the polymer chains, providing access for inserting anions to the positive charges which are consequently compensated and form a double layer. The anion insertion into the polymer has been

indirectly demonstrated by the decrease of the resonance frequency (Figure 28 B) with EQCM, whereas the polymer oxidation (faradaic behaviour) occurs first and is followed by the anion insertion and double layer formation (pseudo-capacitive behaviour) at a lower state of charge. The shear modulus decreases gradually during the charging reaction down to a minimum, indicating a softening effect of the polymer (Figure 28 C) due to the gradual opening of the transport paths. The opening of the transport paths and softening correlates with the observed polymer swelling and grain merging shown by AFM measurements (Figure 31 A-E). [36]

The slight increase of the shear modulus and stiffening of the polymer at a high state of charge accompanies the polymer oxidation with simultaneous strong anion insertion and increased formation of the double layer surface (pseudo-capacitive behaviour), which stretches and expands the polymer backbone to its limits. The strong anion insertion at a high state of charge (>2.1 V *vs.* Al|Al(III)), forming the double layer, suggests a predominant pseudo-capacitive behaviour of the polymer. [36]

Polymer discharging (reduction):

Vice versa, the polymer reduction (Figure 34) is accompanied by the removal of positive charges and therefore, repulsive forces in the polymer backbone. This causes the reversible anion removal (Figure 28 B), the disintegration of the double layer and the contraction of the polymer morphology to its original grainy morphology, as shown by the AFM images (Figure 31 F-J). Simultaneously the shear modulus increases to its initial value, indicating that the original polymer stiffness is regained (Figure 28 C). [36]

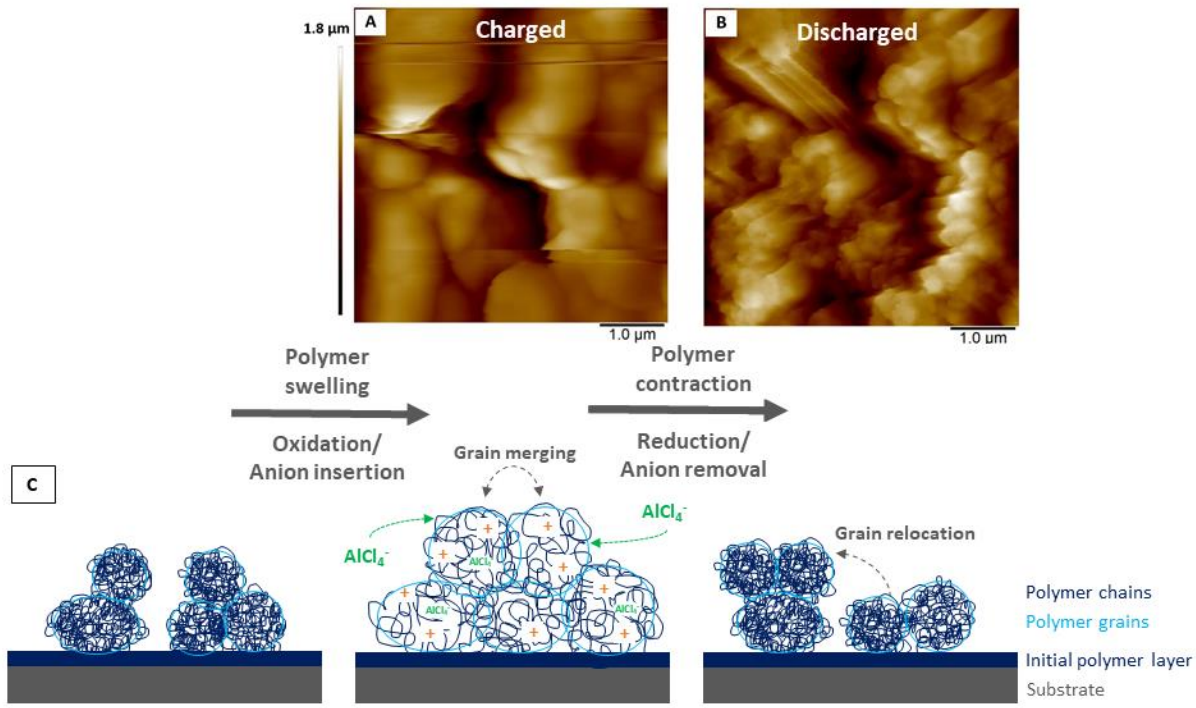

Figure 34: AFM images of PEDOT in monomer-free Lewis neutral EMImCl-$AlCl_3$ in the fully (A) charged and (B) discharged state and (C) schematic model of the morphological changes of a conductive polymer in ionic liquid during charging (oxidation, anion insertion) and discharging (reduction, anion removal). [adapted from 36]

Furthermore, it is assumed that the polymer swelling causes a stronger interchain charge transport due to the merged polymer grains. For instance, the anion insertion/removal at a higher state of charge (2.1 V to 2.5 V *vs.* Al|Al(III)) seems to be more pronounced as the resonance frequency decreases/increases significantly (Figure 28 B). This might be related to the swollen polymer morphology with opened transport paths for anions between the polymer chains. The anions would have the ability to move in and out of the polymer backbone more easily. Furthermore, PEDOT shows a more (pseudo)-capacitive behaviour due to the enhanced anion insertion/removal and simultaneous formation/disintegration of the double layer at this higher electrode potential (>2.1 V *vs.* Al|Al(III)). [36]

It can be concluded that an increasing state of charge is accompanied by an increase of (pseudo)-capacitive behaviour of PEDOT and a lower state of charge is characterised by faradaic or battery-like behaviour. [36]

5.3.2 Aluminium Deposition and Dissolution

The deposition and dissolution of aluminium in Lewis acidic EMImCl-$AlCl_3$ at the anode of the aluminium-PEDOT battery, was characterised by cyclic voltammetry, in-operando atomic force and scanning electron microscopy.

A Lewis acidic EMImCl-$AlCl_3$ ionic liquid contains an excess of $AlCl_3$ and therefore $Al_2Cl_7^-$ ions which can be reduced to metallic aluminium (Equation 1) without any additives in the electrolyte and at room temperature. The cyclic voltammogram (Figure 35) shows a representative cycle of the deposition and dissolution of aluminium on vitreous carbon between -1.0 V and 1.0 V *vs.* Al|Al(III). The reduction of the complex aluminium ion $Al_2Cl_7^-$ starts at -0.2 V *vs.* Al|Al(III) and is accompanied by the nucleation and growth of bulk aluminium on the vitreous carbon surface, showing a peak at -0.25 V *vs.* Al|Al(III) [1]. The deposition occurs with some overpotential due to the nucleation process, which has been reported for many metals in ionic liquids [1,37–42]. The aluminium dissolution is characterised by a broad anodic peak with a maximum of around 0.25 V *vs.* Al|Al(III) [1]. The aluminium deposition and dissolution was performed in a nitrogen atmosphere with water and oxygen levels below 0.5 ppm. Therefore, a passivation layer on the aluminium surface cannot be formed. The coulombic efficiency of aluminium deposition to dissolution (ratio cathodic to anodic charge) is 85 % because the aluminium dissolution is not entirely reversible. It seems that an initial layer of aluminium on the substrate is formed, which is not dissolved. [1]

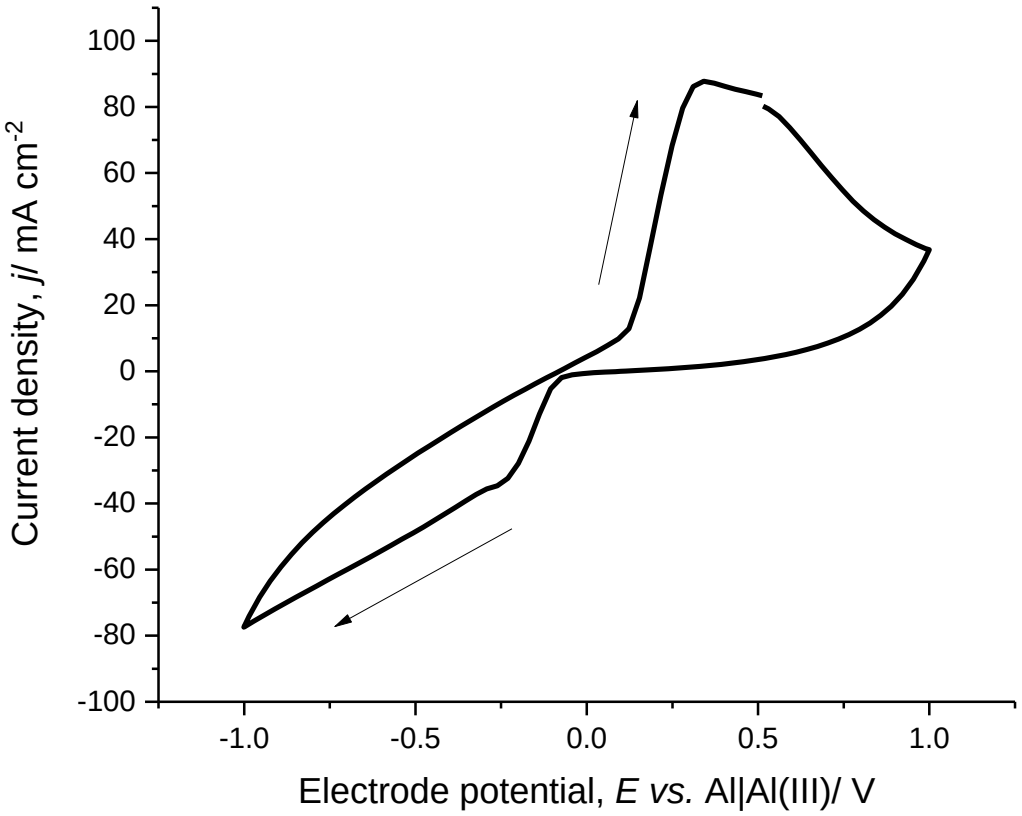

Figure 35: Cyclic voltammogram of the aluminium deposition and dissolution on vitreous carbon in Lewis acidic EMImCl-$AlCl_3$ ionic liquid at cycle 3, 100 mV s^{-1} and 25 °C.

The in-operando AFM measurements of the aluminium deposition in Lewis acidic chloroaluminate ionic liquid provided information about the morphological growth at increasing cathodic potentials from -0.2 to -1.0 V *vs.* Al|Al(III). Aluminium grows as hemispherical grains along the vitreous carbon surface features such as particles and scratches (Figure 36). The average diameter of the hemispherical grains increases gradually from 30 nm to 90 nm with decreasing deposition potential from -0.2 V to -1.0 V *vs.* Al|Al(III). The surface appears very smooth with an average surface roughness R_a from 1.04 nm to 1.12 nm. The maximum height difference of grainy morphology is 10 nm. Dendrite growth cannot be observed.

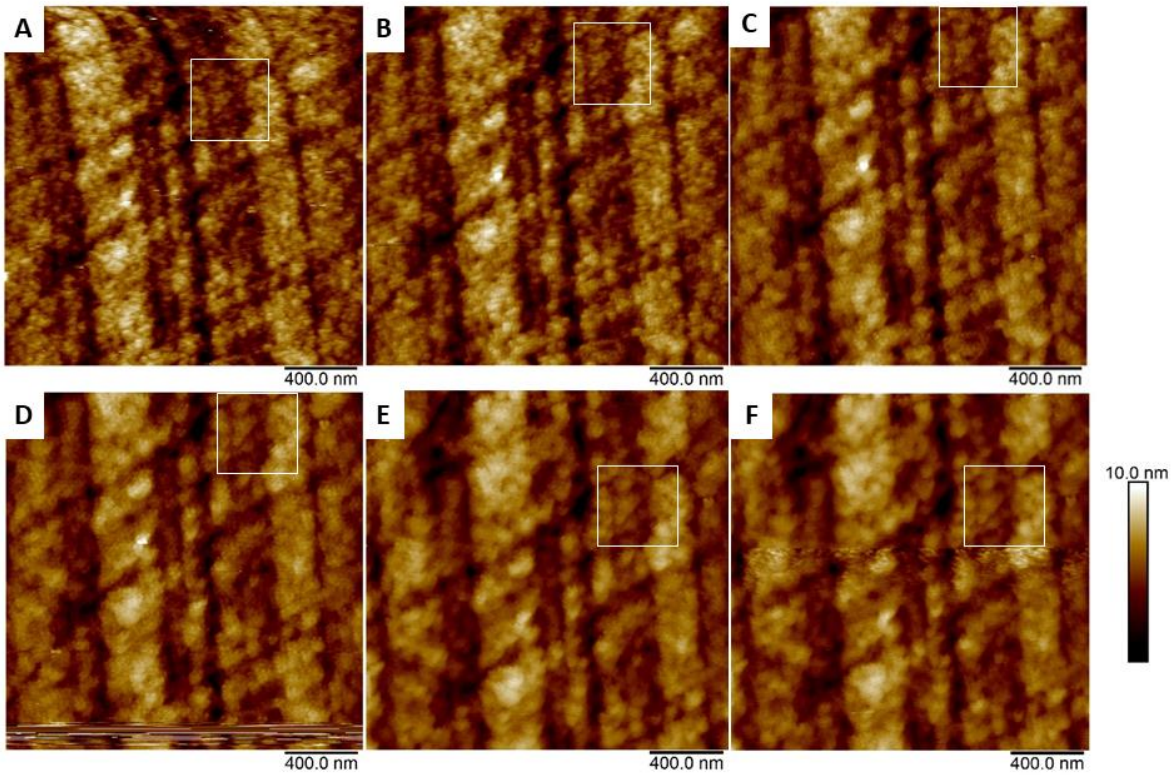

Figure 36: In-operando AFM images of the aluminium deposition on (A) bare vitreous carbon at (B) -0.2 V, (C) -0.4 V, (D) -0.5 V, (E) -0.6 V and (F) -1.0 V vs. Al|Al(III) in Lewis acidic EMImCl-$AlCl_3$ at 25 °C. The white rectangles indicate the same position on the surface.

5.3.2.1 Influence of Lewis Acidity on Aluminium Deposition

In the aluminium-PEDOT battery, a gradient of Lewis acidity is induced (Figure 12) as the polymer cathode performs better in Lewis neutral EMImCl-$AlCl_3$, whereas the aluminium deposition is only possible in a Lewis acidic composition (Paragraph 5.3.1.2 and 3.2.1). Therefore, the influence of the Lewis acidity from neutral (50 mol-%: 50 mol-%) to ultra-acidic (30 mol-%:70 mol-%) on the aluminium deposition was investigated, looking at morphology and coulombic efficiency.

The increase in Lewis acidity (increased ratio of $AlCl_3$ to EMImCl) is also visible in the change of colour of the ionic liquid (Figure 37) from light yellow (neutral, Figure 37 A) to dark brown (ultra-acidic, Figure 37 E).

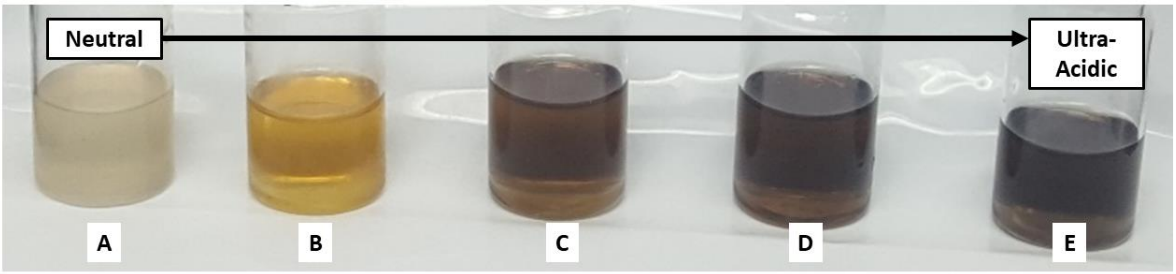

Figure 37: Changes in colour of EMImCl-$AlCl_3$ from Lewis neutral to ultra-acidic. (A) 50 mol-%:50 mol-% (neutral), (B) 45 mol-%:55 mol-%, (C) 40 mol-%:60 mol-%, (D) 35 mol-%:65 mol-% (acidic) and (E) 30 mol-%:70 mol-% (ultra-acidic).

Cyclic voltammograms of the aluminium deposition and dissolution in EMImCl-$AlCl_3$ with increasing Lewis acidity from neutral to ultra-acidic (Figure 38) show that there is no deposition of aluminium in a Lewis neutral composition as the predominant anion is $AlCl_4^-$. It can be reduced to metallic aluminium; however, at potentials below -2 V *vs.* Al|Al(III) which overlaps with the decomposition of the ionic liquid (Figure 14). The CV of a 45 mol-%: 55 mol-% composition, containing slightly more $AlCl_3$, shows a typical nucleation loop of aluminium deposited on the vitreous carbon surface. The nucleation loop starts from -0.2 V *vs.* Al|Al(III) due to a high nucleation overpotential, forming a crossover when the aluminium dissolution occurs already. However, the coulombic efficiency is only 63 % in this composition. Significant higher current densities during the aluminium deposition and dissolution are reached in a light-acidic composition of 40 mol-%:60 mol-%, showing a nucleation loop as well but with a lower overpotential than in 45 mol-%:55 mol-% EMImCl-$AlCl_3$. Dissolution occurs at 0.3 V *vs.* Al|Al(III). A full deposition peak at 0.25 V and 0.3 V *vs.* Al|Al(III) appears for an acidic 35 mol-%:65 mol-% and ultra-acidic 30 mol-%:70 mol-% composition. The aluminium deposits are dissolved at ~0.2 V *vs.* Al|Al(III), respectively, whereas the coulombic efficiency for a Lewis acidic composition is over 80 % and for an ultra-acidic composition only 65 %.

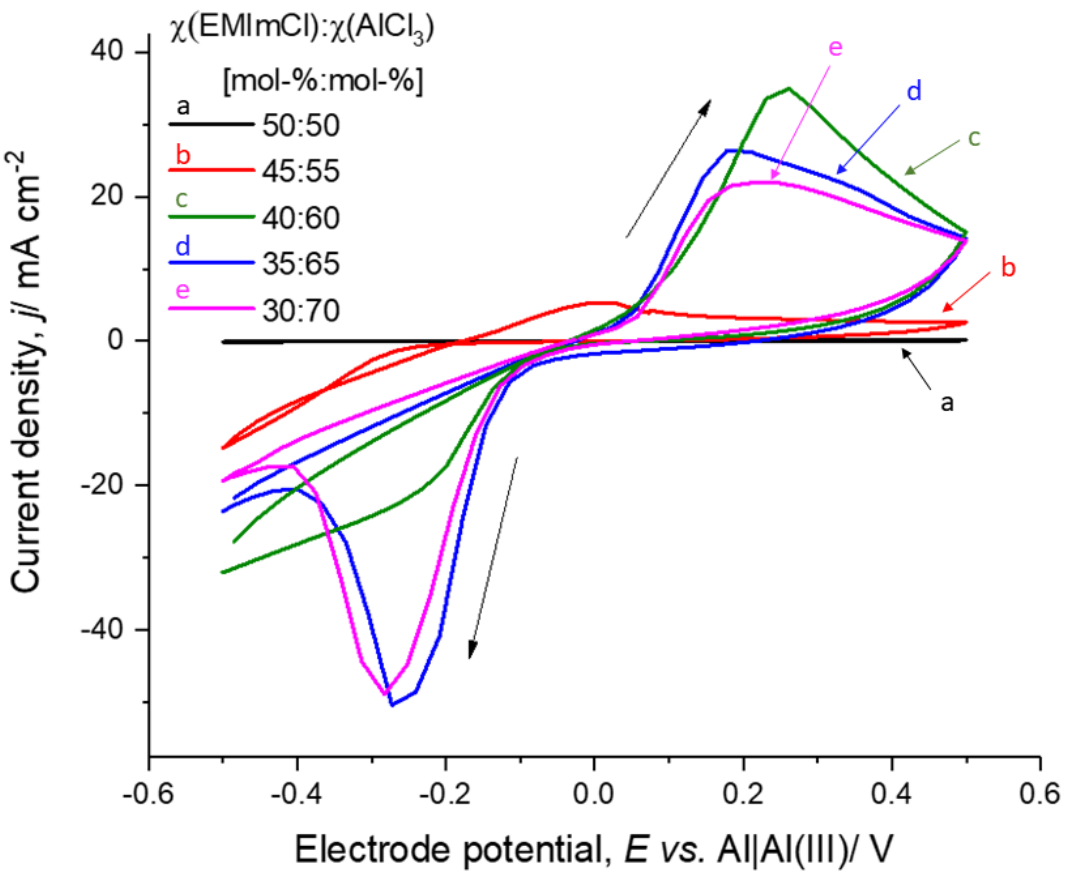

Figure 38: Cyclic voltammograms of the aluminium deposition and dissolution on vitreous carbon in EMImCl-$AlCl_3$ (black line; a) 50 mol-%:50 mol-% (neutral), (red line; b) 45 mol-%: 55 mol-%, (green line; c) 40 mol-%:60 mol-%, (blue line; d) 35 mol-%:65 mol-% (acidic) and (pink line; e) 30 mol-%:70 mol-% (ultra-acidic) at cycle 3, 100 mV s^{-1} and 25 °C.

Aluminium was deposited on a bare aluminium substrate, as intended in the battery assembling, with -1 mA for 30 min at 25 °C in order to investigate the differences in morphology of aluminium deposits obtained in EMImCl-$AlCl_3$ with increasing Lewis acidity (Figure 39). The bare aluminium surface (Figure 39 A) shows parallel scratches from polishing the surface to remove any oxides. As expected, aluminium was not deposited in a Lewis neutral ionic liquid composition because the $Al_2Cl_7^-$ ions required for the deposition of metallic aluminium are not present (Equation 1). There is only a film of ionic liquid left (Figure 39 B) which appears as light patches on the bare aluminium surface. A slight increase in Lewis acidity (45 mol-%:55 mol-%) enables the deposition of single distributed aluminium nuclei with an average grain size of 200 nm (Figure 39 C). A noticeable aluminium deposit grows from a light-acidic composition (40 mol-%:60 mol-%). The aluminium grains (~500 nm) are

distributed homogeneously over the whole surface (Figure 39 D). The grain size increases with an increase in Lewis acidity (Figure 39 D-F) from light-acidic (40 mol-%:60 mol-%) over acidic (35 mol-%:65 mol-%) to ultra-acidic (30 mol-%:70 mol-%), whereas the shape becomes more hemispherical and smaller grains (~200-300 nm) agglomerate to bigger grains (up to 1 µm) in a Lewis acidic composition (Figure 39 E). Aluminium obtained in the Lewis ultra-acidic ionic liquid appears as big cauliflower-like agglomerates with a size from 1 µm to 2 µm (Figure 39 F). It can be seen that aluminium dendrites are not formed in any composition of EMImCl-$AlCl_3$, demonstrating no risk of a potential short circuit in the aluminium-PEDOT battery cell.

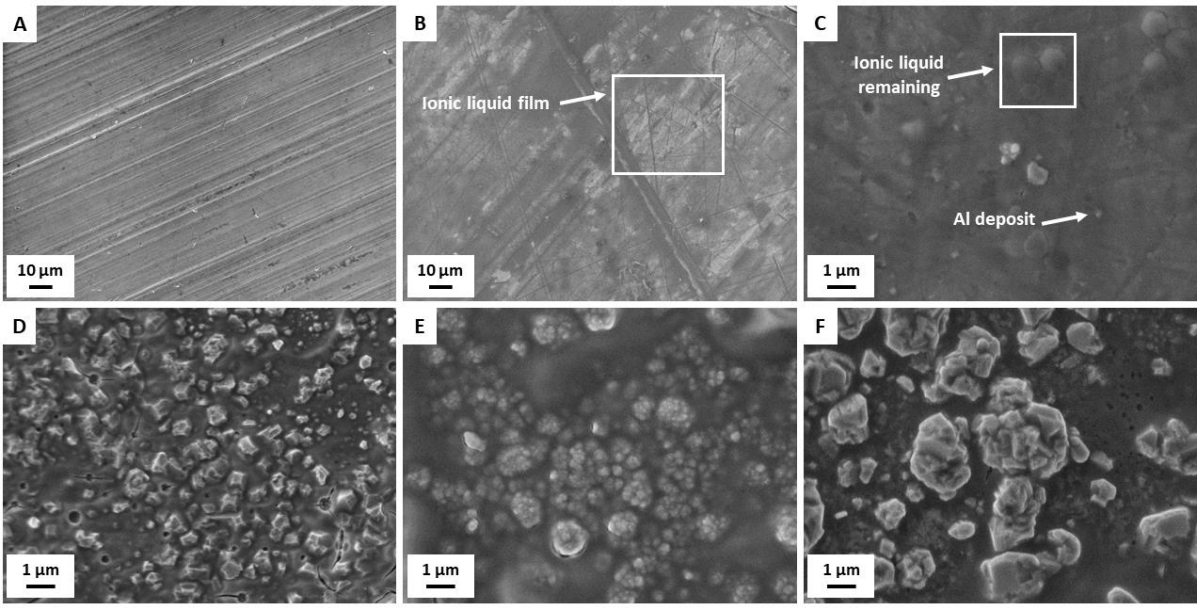

Figure 39: SEM images of (A) bare aluminium surface and aluminium deposit obtained at -1.0 mA for 30 min at 25 °C in EMImCl-$AlCl_3$ (B) 50 mol-%:50 mol-% (neutral), (C) 45 mol-%:55 mol-%, (D) 40 mol-%:60 mol-%, (E) 35 mol-%:65 mol-% (acidic) and (F) 30 mol-%:70 mol-% (ultra-acidic).

5.4 Determination of Battery Characteristics

In comparison to the initial proof-of-concept study of the aluminium-PEDOT battery in Lewis acidic chloroaluminate electrolyte (Paragraph 5.1) [111], the improved battery uses the stable three-dimensional PEDOT electrodes synthesised in Lewis neutral chloroaluminate ionic liquid. Furthermore, in the battery presented here, a gradient in the Lewis acidity of the electrolyte is introduced because PEDOT forms anion insertion sites at higher potentials in a

Lewis neutral composition with $AlCl_4^-$ predominant anions [48], whereas aluminium deposition is only possible in a Lewis acidic chloroaluminate ionic liquid with $Al_2Cl_7^-$ present.

The charge and discharge curve for an aluminium-PEDOT battery (Figure 40) shows several plateaus between 0.5 V and 2.2 V [36]. The open-circuit potential in the fully charged state is 2.1 V. The low potential drop of 100 mV between the charging and starting discharge potential shows the excellent conductivity of the combination of Lewis neutral EMImCl-$AlCl_3$ at the PEDOT cathode (positive electrode) and Lewis acidic EMImCl-$AlCl_3$ at the aluminium anode (negative electrode), forming a gradient between the electrodes.

The calculated coulombic efficiency Q_{eff} (Equation 18) and energy efficiency E_{eff} (Equation 19; consideration of an average charge potential of 1.5 V and average discharge potential of 1.3 V) for the battery are nearly 100 % and 87 %, respectively (Figure 40).

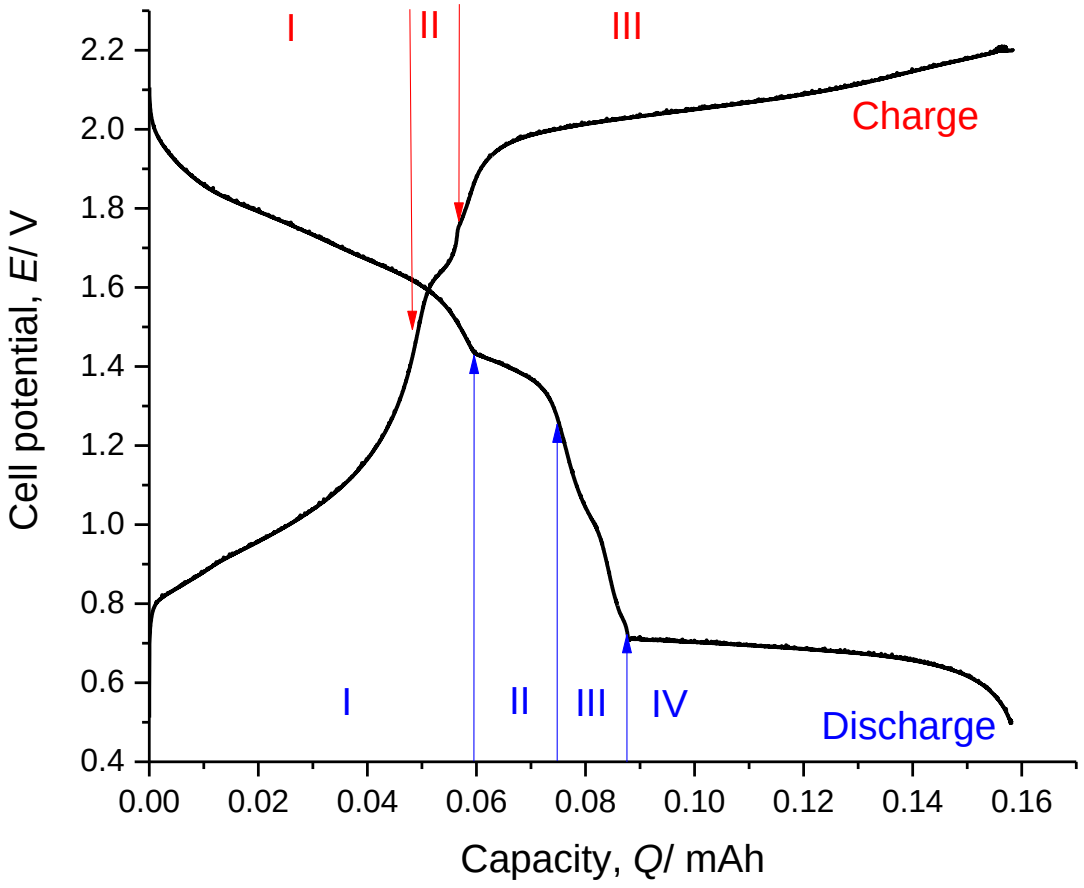

Figure 40: Characteristic charge and discharge cycle of an aluminium-PEDOT battery charged at 0.1 mA (0.8C) until 2.2 V and discharged at -0.1 mA (0.8C) until 0.5 V at 25 °C.

Battery Charging:

The aluminium-PEDOT battery shows a steady increase in potential until 1.5 V when charged at 0.1 mA (0.8C) (Figure 40, area I). A charging plateau cannot be observed in this potential window because the insertion of anions only occurs at potentials above 1.5 V as shown in previous EQCM study (Paragraph 5.3.1.4.1). In the potential range from 0.5 V to 1.5 V the anion insertion paths within the polymer widen [36]. This is due to the formation of repulsive positive charges in the polymer backbone by oxidation (Paragraph 5.3.1.4.2). The starting anion insertion is shown by two potential dips in the charging curve between 1.5 V and 1.7 V (Figure 40, area II). There is a slightly increasing plateau until the cut-off potential of 2.2 V, showing the enhanced insertion of anions (Figure 40, area III). At this stage, PEDOT is oxidised and swollen, enabling the accommodation of high concentrations of $AlCl_4^-$ anions from the Lewis neutral ionic liquid.

Battery Discharging:

The discharge curve starting at 2.1 V is slightly sloping in the potential window from 2.1 V to 1.4 V (Figure 40, area I) when discharged at -0.1 mA (0.8C). In this potential window, the anion removal from the polymer backbone is fast, as the paths between polymer chains are still swollen and open [36]. The formation of the sloping plateau with an average discharge potential of 1.75 V correlates with capacitive-like behaviour of PEDOT observed at this state of charge/discharge [36]. It follows a smaller discharge plateau around 1.4 V (Figure 40, area II) and a drop of the discharge potential from 1.3 V to 0.7 V (Figure 40, area III). This is related to the contraction of the paths between the polymer chains [36]. A constant discharge plateau at 0.6 V (Figure 40, area IV) indicates the battery-like behaviour of PEDOT at a lower state of charge/discharge.

5.4.1 Charge Rate

The aluminium-PEDOT battery has been charged and discharged with an increased charge rate from 0.1 mA to 10 mA (0.8C to 80C) until 2.2 V and subsequently held at 2.2 V until the cell current reached 0.15 mA. The corresponding discharge curves (-0.1 mA, 0.8C) were compared (Figure 41).

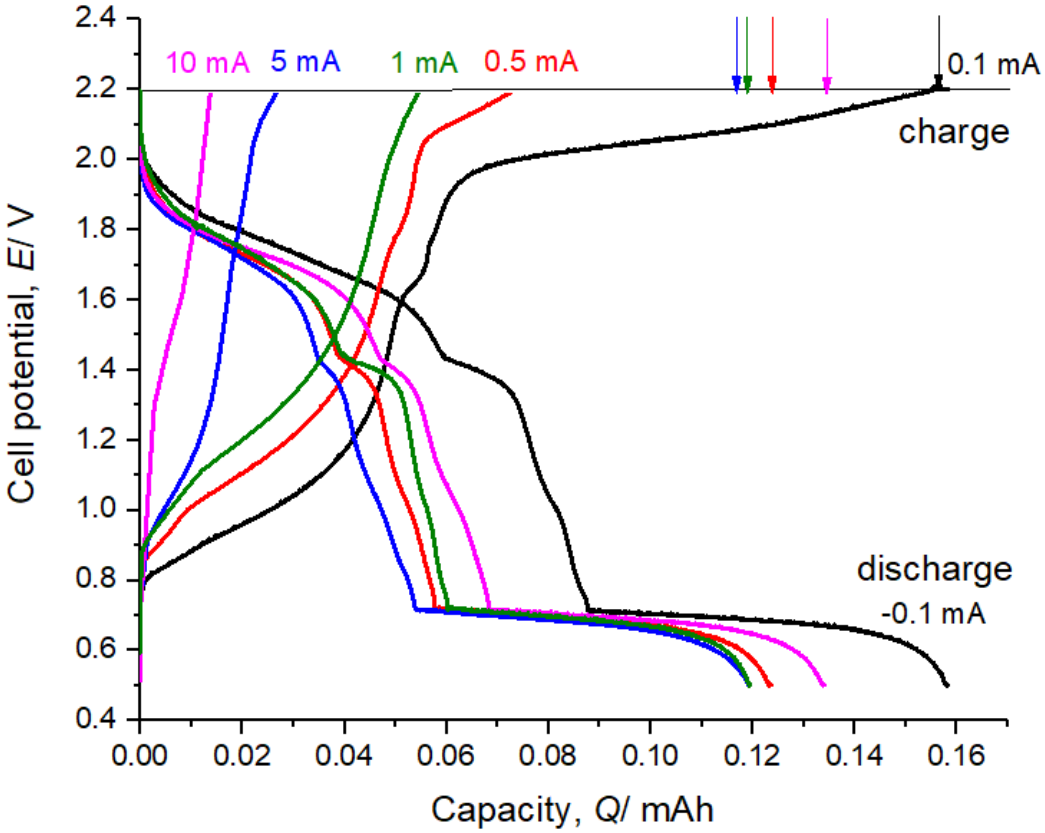

Figure 41: Charge and discharge curves of an aluminium-PEDOT battery charged at 0.1 mA (0.8C, black line), 0.5 mA (4C, red line), 1.0 mA (8C, green line), 5.0 mA (40C, blue line) and 10 mA (80C, pink line) until 2.2 V, held at a constant potential of 2.2 V until 0.15 mA (end of charge marked by arrows) and discharged at -0.1 mA (0.8C) until 0.5 V at 25 °C.

For all charge rates, the charge capacity is equal to the corresponding discharge capacity. The capacity is highest when the cell is charged slowly at 0.1 mA (0.8C), which is the expected behaviour. However, a linear decrease of the capacity with increasing charge rate is not observed. When the cell is charged with 10 mA (80C), it delivers a still higher capacity when charged with 5 mA (40C), 1 mA (8C) or 0.5 mA (4C). With increasing charge rate, the cut off potential of 2.2 V is reached faster, but the constant potential phase until the battery is fully charged (at 0.15 mA) is longer. The battery seems more efficient when charged primarily at constant current, enabling a better anion insertion and higher capacity [36].

5.4.2 Discharge Rate

The battery was charged at 1 mA (8C) to 2.2 V, held at a constant potential of 2.2 V until the current decreased to 0.15 mA, and discharged at -0.1 mA (0.8C), -0.5 mA (4C) and -1 mA (8C)

(Figure 42). The battery shows the same characteristic of discharge behaviour for all discharge rates. The extracted capacity decreases about 37 % when discharged at -1 mA (8C) in comparison to -0.1 mA (0.8C).

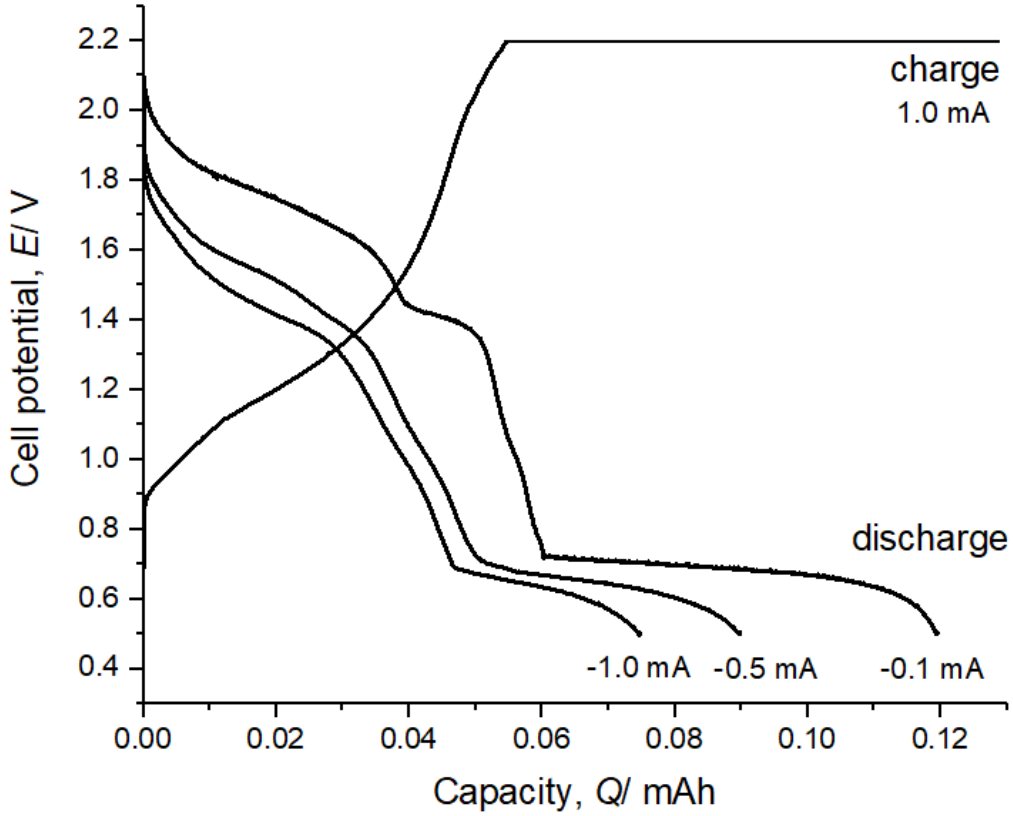

Figure 42: Charge and discharge curves of an aluminium-PEDOT battery charged at 1.0 mA (8C) (until 2.2 V, held at a constant potential of 2.2 V until 0.15 mA and discharged at -0.1 mA (0.8), -0.5 mA (4C) and -1.0 mA (8C) until 0.5 V at 25 °C.

5.4.3 Cycle Stability

The aluminium-PEDOT battery was charged with 1 mA (8C) until 2.2 V, held at this potential until the cell reached 0.2 mA, and discharged at -0.1 mA (0.8C) until 0.5 V for 100 cycles. The coulombic efficiency of one charge and discharge cycle ($Q_{charge}/Q_{discharge}$) ranges between 94 % and 99 % (Figure 43). It demonstrates the reversibility of the electrode reactions (Equation 3) as well as the stability.

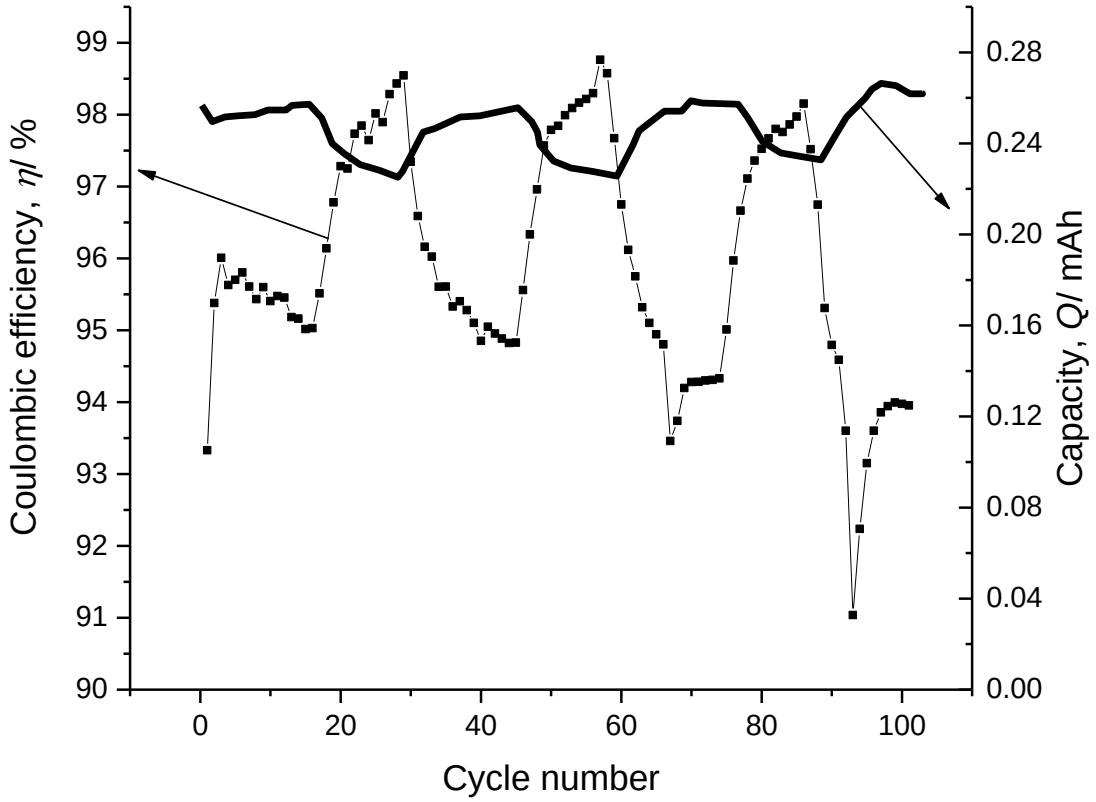

Figure 43: Coulombic efficiency of the charge and discharge reaction of an aluminium-PEDOT battery depending on the cycle number at 25 °C. Battery charged at 0.1 mA (0.8C) until 2.2 V and discharged at -0.1 mA (0.8C) until 0.5 V at 25 °C.

The coulombic efficiency Q_{eff} (Equation 18) of the first cycle (≥93 %) is lower than the average value as the efficiency increases to >95 % over the following cycles. It seems that the coulombic efficiency fluctuates periodically every 20 cycles by 6 %. This might be related to the morphological and viscoelastic changes which the polymer electrode undergoes when charged and discharged (Paragraph 5.3.1.4.1 and 5.3.1.4.2) [36,56,57]. The change of the polymer characteristics is caused by a polymer swelling and contraction phenomena, which has been explained by the generation and removal of repulsive forces between the monomer units, accompanied by anion insertion and removal in the polymer backbone. The charging reaction causes swelling and merging of the polymer grains as well as a softening of the film [36]. This enables a fast charge transfer of anions and the formation of a double layer at the polymer chain surface at a high state of charge, which produces non-faradaic behaviour like a capacitor. [36]

Furthermore, the swelling of the polymer has the effect of widening the transport paths for anions, storing more charges due to the double layer formation and delivering a higher

capacity. The discharge reaction is characterised by contraction and separation of the previously merged polymer grains, whereas the grains relocate from their initial position with decreasing state of charge. At the same time, the polymer regains its stiffness and pronounced faradaic behaviour like a battery. The shear modulus (softness/stiffness) of the polymer film does not return to its initial value after every cycle [36]. PEDOT remains swollen to a certain extent [36]. It seems that it takes about 20 cycles for the polymer to return to its initial shear modulus. [36]

The morphologies of the PEDOT (Figure 44) and aluminium (Figure 45) electrodes were investigated by SEM both before battery cycling and after 100 cycles. The struts of the RVC are coated with an up to 3 µm layer of PEDOT [45] consisting of grains with an average diameter of ≤1 µm. The SEM images before (Figure 44 B) and after (Figure 44 C) battery cycling show no significant change in morphology and no detachment or degradation of the polymer film. This observation coincides with previous studies when PEDOT has been cycled over 500 times by cyclic voltammetry in Lewis neutral EMImCl-$AlCl_3$ [45].

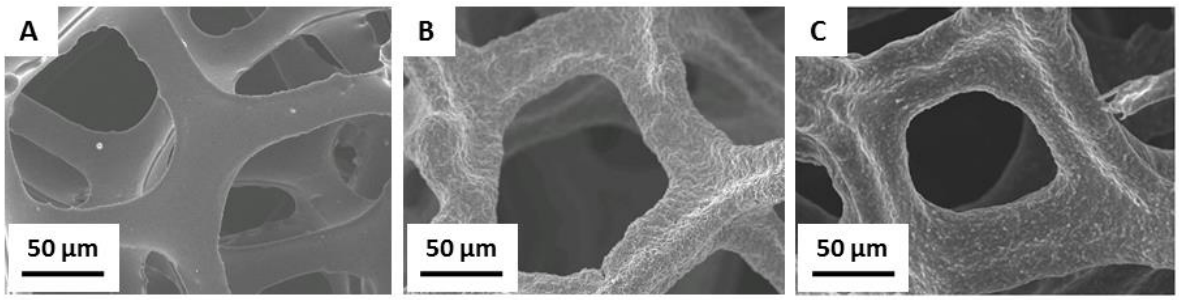

Figure 44: PEDOT: SEM images of (A) bare RVC. (B) PEDOT on RVC, before battery cycling. (C) PEDOT on RVC, after battery cycling (charge CCCV: 1 mA (8C) until 2.2 V, 2.2 V until 0.15 mA; discharge CC -0.1 mA (0.8C) until 0.5 V) for 100 cycles.

The aluminium deposition on the negative electrode was carried out on polished high purity aluminium substrates (Figure 45 A). After 100 charge and discharge cycles, a clear aluminium deposit is visible (Figure 45 B-D). The aluminium deposits appear as hemispherical grains with an average size of ≤5 µm, which is typical for aluminium deposits in ionic liquids at low anodic current densities of ≤10 mA cm^{-2} [1,9,13,27,102,103]. These grains agglomerate over the electrode surface, forming hemispherical flower-like structures with an average diameter of ≤50 µm. Dendrite growth, which could lead to a short circuit of the battery, has not been observed.

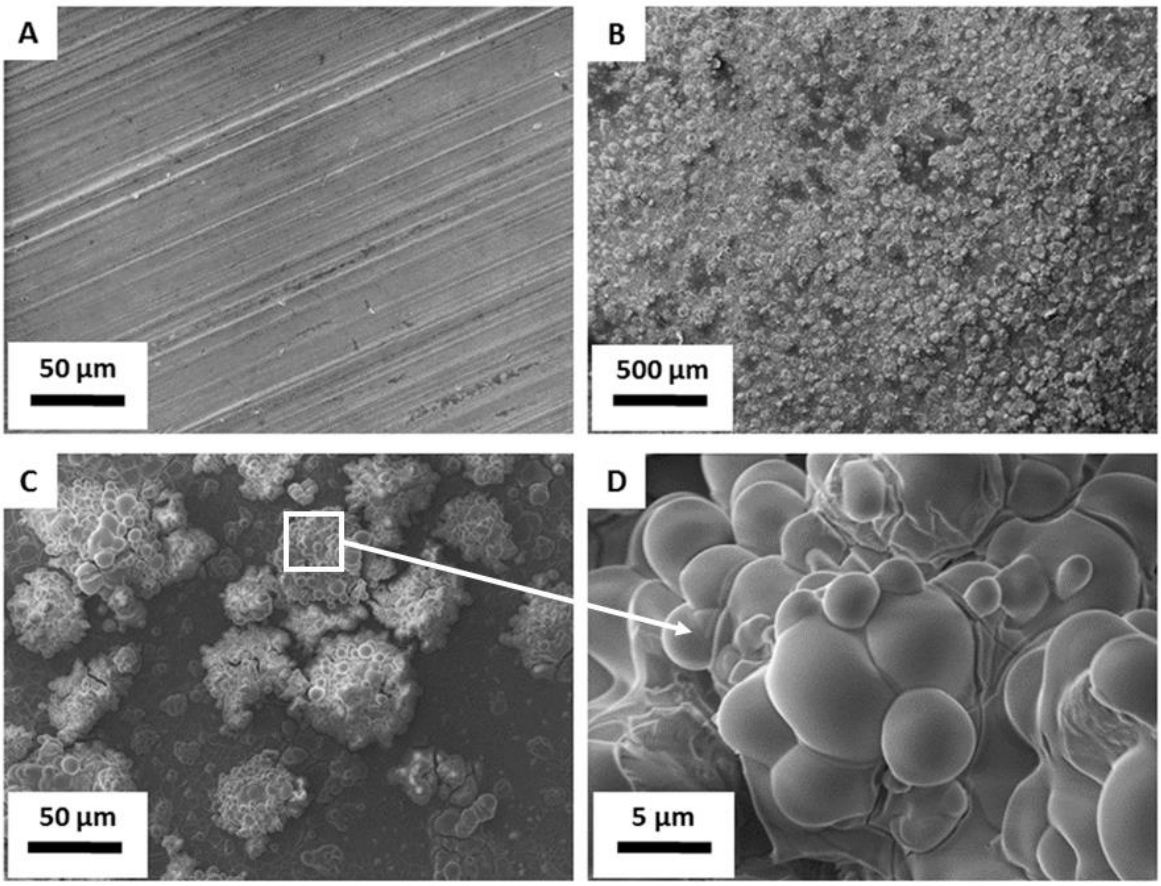

Figure 45: SEM images of (A) pure aluminium surface before and (B-D) after battery cycling (charge CCCV: 1 mA (8C) until 2.2 V, 2.2 V until 0.15 mA; discharge CC -0.1 mA (0.8C) until 0.5 V; 100 cycles) with aluminium deposit.

5.4.4 Battery Characteristic Values

PEDOT and aluminium are both low-weight materials, not least because of the three-dimensional structure of PEDOT and its highly active surface area per unit volume and mass. The battery characteristic values (Table 5) such as specific capacity, energy and power were calculated for the aluminium-PEDOT battery based on its measured discharge capacity of 0.16 mAh and average discharge potential of 1.3 V (Figure 40). For the active mass, 3 different cases were considered:

Case 1) Active species: Considering solely of mass m_a of active species which actively take part in the battery reaction (Equation 20).

Case 2) Active species with insertion anions: Considering mass m_a *of* active species like in case 1 with inserting $AlCl_4^-$ anions from Lewis neutral EMImCl-$AlCl_3$ in the PEDOT cathode (Equation 23).

Case 3) All species: Considering mass m_a of all species in the battery. This also includes "dead mass" such as $EMIm^+$ cations, based on the method (Equation 25) of Kravchyk et al. [95].

Table 5: Calculated active mass m_a, specific capacity Q_{spec}, energy E_{spec} and power P_{spec} for an aluminium-PEDOT battery at a charge and discharge rate of ± 0.1 mA (0.8C) (Figure 40).

Case	m_a/ kg	Q_{spec}/ Ah kg^{-1}	E_{spec}/ Wh kg^{-1}	P_{spec}/ W kg^{-1}
1) Active species	3.24×10^{-6}	49	64	40
2) Active species with insertion anion	3.57×10^{-6}	41	58	36
3) All species	4.13×10^{-6}	39	50	32

The calculated performance of the aluminium-PEDOT battery is similar to other reported aluminium-based batteries with chloroaluminate ionic liquid electrolyte. Using a method comparable to case (2), aluminium-graphite batteries have achieved 69 Wh kg^{-1} [96], whereas using a method comparable to the case (3), a specific energy of 65 Wh kg^{-1} [95] has been reported for the half-cell. The increase in specific energy compared to aluminium-PEDOT is due to the higher average discharge potential of aluminium-graphite (~1.77 V *vs.* 1.3 V).

For the purpose of comparison, e.g. with the initial proof-of-concept study, the specific capacity, energy and power for an active mass only of the deposited mass of aluminium and PEDOT are 179 Ah kg^{-1}, 233 Wh kg^{-1}, and 146 W kg^{-1}. Taking into account also the inserting anions $AlCl_4^-$ at the cathode for a degree of insertion of 0.33, the values reduce to 56 Ah kg^{-1}, 73 Wh kg^{-1} and 46 W kg^{-1}.

The theoretical capacity of the used PEDOT cathode is 191 mAh g^{-1} if the whole mass of polymerised PEDOT on RVC and a battery discharge capacity of 0.16 mAh is considered (Figure 40). That demonstrates a capacity that indicates that every monomer unit present carries a single positive charge. However, it is not suggested that all of these charges are balanced by an inserted anion. From previous research, the maximum degree of anion insertion α is 0.33 [46–48]. Therefore, PEDOT clearly indicates a combination of faradaic and capacitive charge storage in the proportion of 2:1 capacitive to faradaic storage, achieving 64 mAh g^{-1} through faradaic storage and 127 mAh g^{-1} capacitive storage. The capacity of PEDOT used in this work is about 50 mAh g^{-1} higher than the highest achieved for graphite (142 mAh g^{-1}) in aluminium batteries with chloroaluminate ionic liquid [95]. It must be pointed out that the charge storage mechanism of conductive polymers differs from graphite. Conductive polymers such as PEDOT insert anions into their polymer structure while compensating positive charges located at the monomer units. In contrast, graphite intercalates anions between its carbon layers. The capacity of graphite is limited as not every layer intercalates chloroaluminate anions.

In addition, a high degree of intercalation causes a macroscopic expansion of the cathode material and could cause damage to the battery. In contrast, PEDOT can be designed to accommodate a variable amount of anions by adapting film thickness, substrate dimensions and shape. PEDOT also expands during charging [36], providing a higher capacity as more monomer units become accessible for inserting anions. However, the polymer cathode is designed smartly as there is no overall volumetric change. PEDOT expands and contracts around the struts of the RVC, which acts as a rigid substrate. The mesoporous structure of the RVC provides space for PEDOT to change its volume internally in the cathode. This makes PEDOT more efficient than graphite as the whole electrode mass can actively take part in the battery reaction, and no dead electrode mass needs to be considered.

Considering only the cathode, PEDOT shows better performance than graphite with a higher specific capacity and better volume change characteristics. Nevertheless, the limiting factor is not the cathode material. The specific capacity, energy and power are almost entirely determined by the chloroaluminate ionic liquid, especially the Lewis acidic composition with $Al_2Cl_7^-$ anions. In order to improve the battery performance with a chloroaluminate ionic liquid, the cell potential needs to be increased instead. The cell potential can be improved by

modifications of the electrolyte, e.g. gelification, increasing the potential stability window. Currently, the ionic liquid starts to decompose when charged frequently over 2.3 V. Therefore, the limiting charging potential is 2.2 V. If the potential window of a Lewis neutral chloroaluminate ionic liquid with solely $AlCl_4^-$ anions can be increased by 1 V, the deposition of aluminium from $AlCl_4^-$ would be possible, reducing the active mass of the electrolyte significantly.

5.5 Next Step for Performance Improvement

In general, the limiting factor in terms of specific capacity, energy and power of aluminium-based batteries is the Lewis acidic chloroaluminate ionic liquid with heavy $Al_2Cl_7^-$ anions and the potential stability window of 4 V. In order to improve the battery performance with a chloroaluminate ionic liquid, the cell potential has to be increased and aluminium deposited from the $AlCl_4^-$ anion (Equation 26) which has almost half of the molar mass of the $Al_2Cl_7^-$ anion.

$$AlCl_4^- + 3e^- \underset{\text{discharge}}{\overset{\text{charge}}{\rightleftharpoons}} Al + 4Cl^- \qquad (26)$$

The cell potential can be improved by modifications of the electrolyte, e.g. gelification (Figure 46, inset photo), increasing the total potential stability window up to 8 V (Figure 46). The ionogel has been synthesised by adding 10 % polyethylene oxide to the Lewis neutral EMImCl-$AlCl_3$ at 60 °C. The gel forms when the mixture cools down to room temperature. Furthermore, the ionogel is stable in an ambient atmosphere. Thus, the handling is easier and cheaper as it does not require a glove box with an argon or nitrogen atmosphere, which is free of oxygen and water.

Currently, a Lewis neutral ionic liquid starts to decompose around -2 V *vs.* Al|Al(III) (Figure 46, blue curve), so that the reduction of $AlCl_4^-$ to metallic aluminium at ≤-2 V *vs.* Al|Al(III) cannot occur. The CV of the Lewis neutral ionogel shows a potential stability window from -4 V to 4 V *vs.* Al|Al(III) (Figure 46, black curve) with significantly higher current densities than the liquid. An anodic peak around 0 V *vs.* Al|Al(III) in the ionogel indicates the dissolution of previously deposited aluminium below -2 V *vs.* Al|Al(III) (Figure 46, red curve).

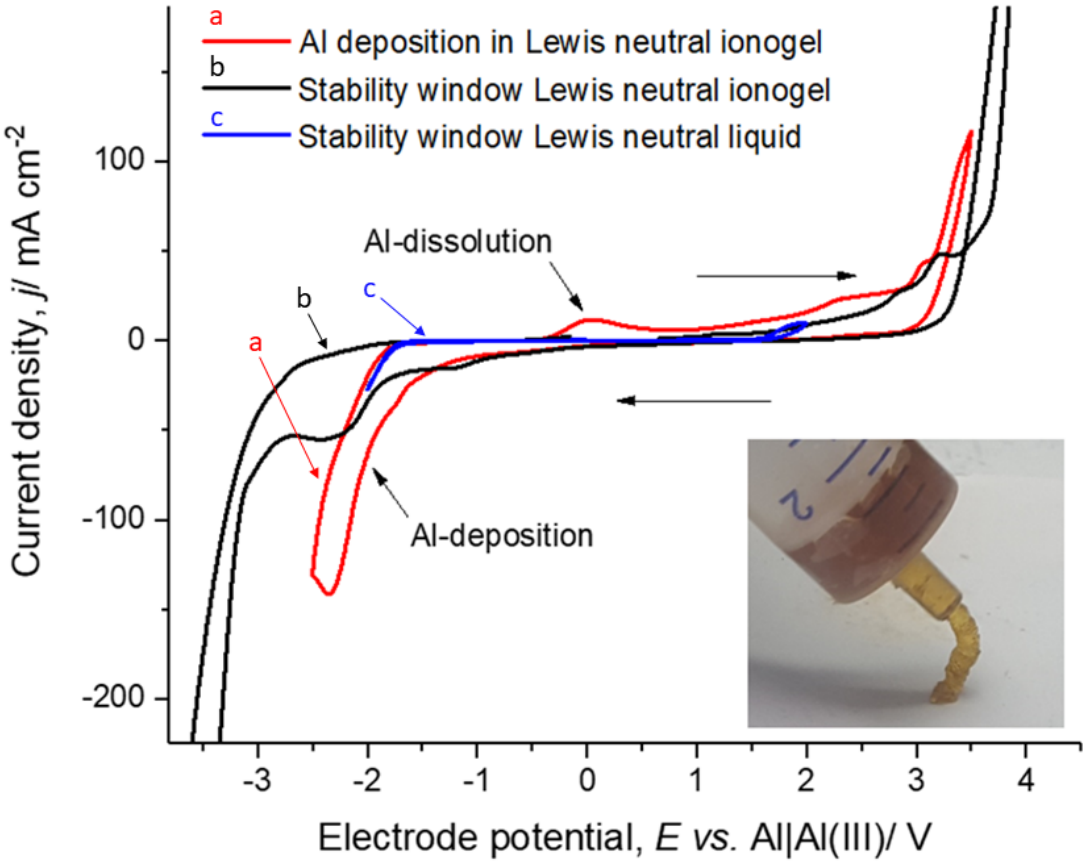

Figure 46: Cyclic voltammograms of Lewis neutral EMImCl-$AlCl_3$ liquid (blue curve, c) and ionogel (black, b and red, a curve) with vitreous carbon as working and counter electrode and aluminium as reference electrode at 100 mV s^{-1} and 25 °C. The inset photo shows synthesised Lewis neutral ionogel.

Hypothetically, if the same discharge capacity of 0.16 mAh (Paragraph 5.4.4) is extracted from a battery with Lewis neutral ionogel, but the aluminium is deposited from $AlCl_4^-$ (Equation 26), the specific capacity, energy and power can be increased to 260 Ah kg^{-1}, 338 Wh kg^{-1} and 211 W kg^{-1} (referring to mass m_a of active species which actively take part in the battery reaction). Considering additionally an increase of cell potential by at least 1 V so that the average discharge potential increases to 2.3 V, the specific capacity, energy and power can be improved still further to 260 Ah kg^{-1}, 598 Wh kg^{-1} and 374 W kg^{-1} (referring to mass m_a of active species which actively take part in the battery reaction). This level of performance would compete with state-of-the-art lithium-based batteries and beyond.

6 Conclusions

This work started with the proof-of-concept study showing the feasibility of a new aluminium-conductive polymer battery with an ionic liquid electrolyte. The conductive polymer PEDOT was electropolymerised in aqueous solution on a two-dimensional vitreous carbon substrate. The PEDOT cathode was assembled with a metallic aluminium anode in a battery cell with Lewis acidic EMImCl-$AlCl_3$ ionic liquid. The initial performance of the battery reached a specific energy and power of 84 Wh kg^{-1} and 179 W kg^{-1} (considering solely the mass of the aluminium anode and the PEDOT cathode), respectively. However, a severe loss of capacity and low coulombic efficiency occurred after just a few charge and discharge cycles (≤20 cycles) due to the detachment of the PEDOT film from its substrate. The lack of polymer stability was caused by residual water in the pores of PEDOT originating from its synthesis in aqueous solution. The moisture sensitive chloroaluminate ionic liquid in the battery reacted with the water to form hydrochloric acid and chlorine gas resulting in the fast battery failure. Therefore, the main focus needed to be put on the improvement of the conductive polymer stability. It was apparent that PEDOT needed to be electropolymerised in an electrolyte similar to the ionic liquid used in the battery. For this reason, the polymerisation was studied in a Lewis basic, neutral and acidic EMImCl-$AlCl_3$. Only a Lewis neutral composition enables the electropolymerisation of PEDOT films which show no degradation and a coulombic efficiency of 97 % during cycling. In order to improve the performance of the polymer, PEDOT was synthesised electrochemically on three-dimensional reticulated vitreous carbon substrates in Lewis neutral EMImCl-$AlCl_3$. The increased number of active anion insertion and removal sites improved the polymer capacity by 45 %. Half-cell studies of aluminium and PEDOT in EMImCl-$AlCl_3$ delivered insights in the anodic and cathodic cell reactions, whereas the aluminium deposition and dissolution in Lewis acidic chloroaluminate ionic liquid is a well-studied process. The focus in this work was put on the interaction between the conductive polymer and the ionic liquid. In addition, the polymer behaviour during charging and discharging has not been fully understood up to this point. The applied in-operando characterisation methods reveal new insights into polymer behaviour during the operation of the battery. The work was concluded by assembling and testing of battery cells with the improved PEDOT cathodes, electropolymerised in Lewis neutral EMImCl-$AlCl_3$ on reticulated vitreous carbon, and a perspective to further studies modifying the ionic liquid electrolyte.

Conductive polymer (PEDOT) cathode:

The behaviour of PEDOT has been studied from its electropolymerisation, its electrochemical behaviour in the ionic liquid, to its charge/discharge characteristic in the full battery cell. It has been shown that PEDOT can only be electropolymerised in Lewis neutral EMImCl-$AlCl_3$ with $AlCl_4^-$ as the predominant insertion anion. The polymerisation has a significant influence on the polymer behaviour when charged and discharged in the battery. The anion insertion and removal are predefined during electropolymerisation and do not form or change during battery cycling ("memory effect" of the polymer). A wider polymerisation potential window generates a cross-linked surface structure and more anion insertion and removal sites, which lead to higher possible charge and discharge potentials of the cathode. In addition, PEDOT films show different anion insertion and removal behaviour in monomer-free Lewis acidic, basic and neutral EMImCl-$AlCl_3$. PEDOT films in a Lewis neutral composition can reach higher anion insertion and removal sites at a higher potential due to the higher potential stability window over 4.0 V *vs.* Al|Al(III) compared with the Lewis acidic and basic compositions. The insertion and removal of $AlCl_4^-$ into the PEDOT film reaches a reversibility of 97 % in Lewis neutral EMImCl-$AlCl_3$. In-operando methods such as atomic force microscopy and electrochemical quartz crystal microbalance measurements helped to create a model for the fundamental understanding of the polymer behaviour in ionic liquid during battery operation. It has been shown that PEDOT undergoes a reversible morphological modification during charging and discharging while its viscoelastic properties change simultaneously. The change of polymer characteristics is caused by a polymer swelling and contraction phenomena, which has been explained by the generation and removal of repulsive forces between the monomer units, accompanied by anion insertion and removal in the polymer backbone. The charging reaction causes swelling and merging of the polymer grains as well as a softening of the film. This enables a fast charge transfer of inserting anions at a high state of charge, which represents capacitive behaviour. The discharging reaction is characterised by contraction and separation of the previously merged polymer grains, whereas the grains relocate from their initial position with a decreasing state of charge. At the same time, the polymer regains its stiffness and pronounced faradaic behaviour like a battery. These fundamental insights of the polymer properties in accordance with the state of charge have an essential influence on the polymer synthesis and design as the polymer morphology determines the performance and

electrode behaviour. A systematic structuring of the polymer can emphasise the battery or capacitor characteristics, depending on the wide range of application.

New insights:

The half-cell studies on the conductive polymer cathode in ionic liquid electrolyte delivered new insights about the polymer behaviour and performance having an impact on the use as a battery material:

- Electropolymerisation of highly reversible PEDOT films is solely possible in Lewis neutral EMImCl-$AlCl_3$ with $AlCl_4^-$ anions.
- PEDOT shows a “memory effect” from its electropolymerisation; polymerisation predefines the behaviour of the polymer cathode during battery cycling such as potential stability window, anion insertion and removal potentials and capacity.
- PEDOT undergoes reversible morphological and viscoelastic changes during battery cycling; polymer swelling and contraction lead to pronounced capacitive charge transfer at a high state of charge and faradaic charge transfer at a low state of charge (hybrid battery-capacitor characteristic).

Aluminium anode:

The aluminium deposition and dissolution at the anode in Lewis acidic EMImCl-$AlCl_3$ shows the expected behaviour. Aluminium forms micro- to nanocrystalline grains on high-purity aluminium substrates. Dendrite growth, which could cause a short circuit in the battery, has not been observed. With regard to changes of the ionic liquid Lewis acidity at the anode, the influence of the acidity on the aluminium deposition has been studied. The deposition of aluminium is possible from a light-acidic (40 mol-%:60 mol-%) to an ultra-acidic (30 mol-%: 70 mol-%) composition, whereas the coulombic efficiency with 85 % is highest at the acidic composition (35 mol-%:65 mol-%). The grain size of the aluminium deposits increases with the Lewis acidity.

Aluminium-PEDOT battery concept and performance:

The aluminium-PEDOT battery with the improved three-dimensional stable PEDOT cathodes and ionic liquid gradient, Lewis acidic EMImCl-$AlCl_3$ at aluminum anode and neutral at PEDOT

cathode, can be charged and discharged reversibly in the cell potential window of 0.5 V to 2.2 V. The battery characteristic values such as specific energy and power are in the range of 50-64 Wh kg^{-1} and 32-40 W kg^{-1} referring to different realistic cases considered in terms of active mass in the battery. In comparison to the initial proof-of-concept study, the battery with the improved PEDOT cathode and electrolyte acidity gradient reaches a significantly higher specific energy of 233 Wh kg^{-1} and a similar power of 146 W kg^{-1} (considering solely cathode and anode masses). In contrast, the cell reaches high cycle stability with a coulombic efficiency of ≥95 % and shows no morphological degradation of the PEDOT or aluminium electrode surface over 100 cycles. The current limiting factor of the battery is the potential stability window of the ionic liquid electrolyte, preventing extended charge and discharge potentials. The Lewis neutral-acidic ionic liquid composition starts to decompose when charged frequently over 2.3 V. Therefore, the limiting charging potential is 2.2 V. The potential window, and consequently, the cell potential can be improved by the gelification of the ionic liquid to an ionogel. Preliminary studies show an increase of at least 2 V in both anodic and cathodic potential directions. Furthermore, the current capacity achievable by the aluminium-PEDOT battery correlates with the capacity of PEDOT obtained during electropolymerisation. This suggests that thicker polymer films and high polymer surface area using three-dimensional (nanostructured) substrates or even freestanding three-dimensional polymer structures can increase the capacity.

Beneficiaries and impact:

The work connects the dots between picking up new ideas, fundamental research, proof-of-concept studies and battery prototype development. The concept of an aluminium-PEDOT battery positions narrow by demonstrating a new and alternative battery concept beyond lithium-ion made of safe and sustainable materials. At the same time, it reaches wide by raising awareness of alternative batteries which can make a distinctive contribution to the development and acceleration of novel and emergent battery technologies which society urgently needs, both today and in the future. Finally, the message of the work highlights the importance of safety and sustainability of the whole energy storage cycle; from raw materials production, materials synthesis and device fabrication to recycling.

7 Perspective and Trends in Battery Research

Modern batteries are all those which make electromobility affordable and accessible for the breadth of society, push forward smarter consumer electronics with low to zero waste impact, realise the miniaturisation of batteries to the nano/micro-scale for medical implants and enable artificial intelligence such as next-generation robotics. Batteries are basically designed with the same principle as when they were first invented. In fact, there has not been a major step forward since the introduction of lithium batteries in the early 90's [104]. Today's fundamental limitation for advancements in energy storage is the compromise that has to be made between performance (referring to capacity, specific energy and power, life-time), safety and sustainability. This compromise can be made easily for stationary applications, e.g. to store energy from renewable energy sources on a large scale. However, superior battery technologies are required for innovative mobile applications such as electromobility, consumer electronics and artificial intelligence. Even post-lithium ion batteries such as lithium-air or lithium-sulphur batteries do not solve the problem of sustainability and safety caused by the use of lithium and even accept losses in performance [105]. Therefore, the timely grand challenge is not to improve already existing technologies but to take a step back, look at the bigger picture, identify today's and tomorrow's energy storage requirements and take a completely novel approach beyond lithium-based batteries [106].

Mobile battery applications certainly require energy storage materials that combine high specific energy and power, long life-time, non-toxicity, non-flammability, raw materials abundance and low cost while the fabricated batteries should be adaptable in size and shape, e.g. nanosized, bendable and flexible. In order to blend these characteristics in a single battery system, safe, smart and sustainable materials need to be identified first. Safety and sustainability criteria can easily be achieved by using the energy storage materials from the following categories (a to d):

Identified safe, smart, sustainable energy storage materials (3sESM):

a) *Charge storage materials*: conductive polymers, 3D carbon materials
b) *Ionic materials:* ionic liquids, ionogels, deep eutectic solvents
c) *Nature-inspired materials:* natural fibres and tissues, engineered microorganisms
d) *Solid state materials:* abundant metals (Al, Mg, Na, Zn), metal oxides, conductive glass

3s-energy storage materials account for safety, smartness and sustainability. This includes no flammable and toxic cell components or reactions for safety. Specific energy, power, capacity, cycle life, rate capability and size and shape adaptability for smartness. Low and stable costs, recyclability, resources availability and ethical production conditions for sustainability.

Some *Charge storage materials* combine faradaic behaviour due to oxidation and reduction of an active electrode species at the electrode-electrolyte interface and at the same time they show non-faradaic behaviour by intercalating or inserting a guest ion species in their three-dimensional material structure without modification [107]. In this case, the materials behave both as a battery and a supercapacitor, closing the gap between high specific energy and power [108]. High capacities can be reached due to high active surface area per unit volume and denser packing of material [109].

*Ionic materials s*uch as ionic liquids and ionogels are especially chemically and electrochemically stable and are recyclable or even biodegradable. Ionogels can be obtained by adding small amounts of a gelating component to ionic liquids at elevated temperatures to then induce physical organisation of a more solid (gel) network while keeping liquid-like properties such as conductivity and ion mobility. In addition, highly conductive and thin ionogel electrolytes do not leak and can be formed to any shape, also making the separator in the battery cells redundant, which could reduce the overall weight. [71]

Nature-inspired materials such as wood fibres create well-ordered conductive paths for ion diffusion, improving rate capability for fast charging. In addition, the materials allow a change in shape and have excellent recyclability. [110]

Solid state materials especially address safety concerns like flammability, leaking, evaporation and decomposition to toxic components. Solid state electrolytes particularly stand out for their wide potential stability window, temperature tolerance and distinct charge transfer excluding unwanted side reactions. [111]

Nevertheless, the materials in the aforementioned categories cannot provide high battery performances when used individually as electrode or electrolyte materials; at least not when

assembled in the conventional battery design (Figure 47), in a stack of layers of anode-electrolyte-cathode materials. What if next generation batteries are not designed like the conventional stack but instead as a “one-piece battery” turning all materials from 2D to 3D (Figure 47) with low-cost electrochemical nano-design methods? The novelty arises when all battery components (anode, electrolyte and cathode) are fabricated to one composite (electrode-electrolyte composite battery, EEC-battery) [112–114].

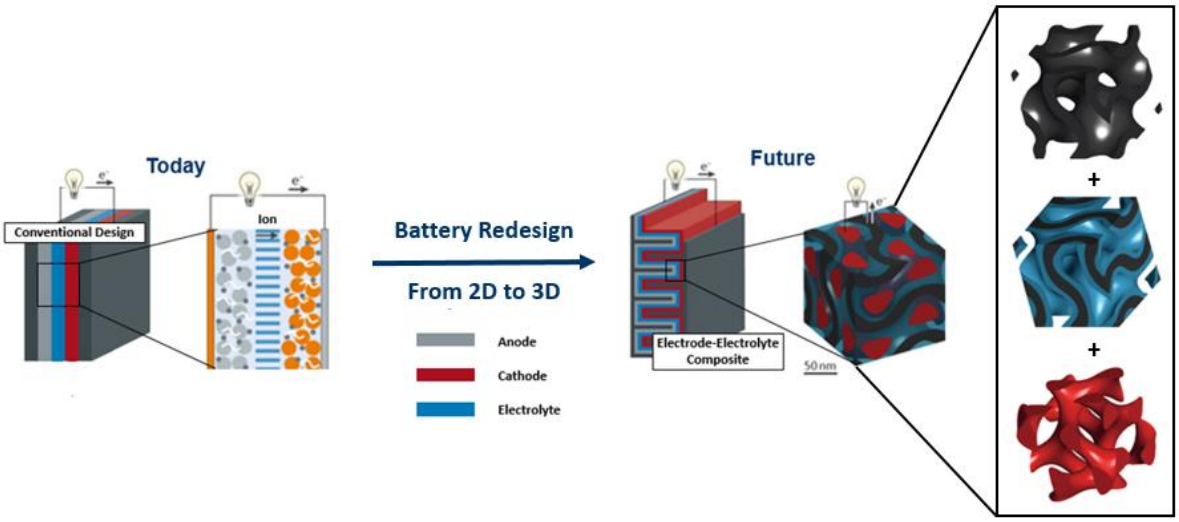

Figure 47: Redesign of today's conventional battery architecture to efficient EEC-batteries in the future. The drawings are adapted and reproduced with permission of The Royal Society of Chemistry [114].

A key aspect are porous, three-dimensional and nano-structured electrode designs with a high active surface area, increasing the battery capacity. A three-dimensional electrode-electrolyte network also lowers the volumetric stress for electrodes during intercalation or insertion processes, preventing degradation like cracking, while keeping structural integrity. In combination with highly conductive solid state or gel electrolytes with a wide potential stability window [74], “charge transfer traffic jam“ can be reduced, realising shorter interconnected transport paths for ions and electrons. This concept enables fast charge rates and a boost of capacity, specific energy and power of 3sESM while flexible, smaller and lighter battery architectures are possible. Moreover, EEC make as much use as possible of active battery materials and minimise the non-active mass (“dead mass”), as the amount of energy stored is proportional to the active material [114].

The application of nano-design methods [115] to 3sESM basically aims to maximise their electrochemical properties. However, nanotechnology only becomes sustainable in energy storage if the synthesis paths are straight forward and inexpensive. For instance, top-down nano-patterning methods or deposition techniques like atomic layer deposition or chemical vapour deposition are not so well suited for large-scale applications because they are slow and expensive. More efficient synthesis paths are bottom-up methods such as electrochemical deposition and pulse plating with and without templates [116]. Complex nanostructures can be created with templates like anodic aluminium oxide, titanium membranes, colloidal polystyrene, carbon nanotubes, self-assembled monolayers and block co-polymers [117–120]. Methods like electrospinning, three-dimensional printing and fountain-pen deposition are also able to fabricate fibre structures [121].

The key challenge for the development of nano-designed EECs is the understanding of the connection between material synthesis paths and material behaviour. Cutting edge in-operando characterisation methods such as electrochemical atomic force microscopy (EC-AFM) provide essential information about theoretical maximum performance values, morphological, viscoelastic, nano-mechanical and nano-electrical characteristics as well as cycle life and degradation processes [36]. With such novel experimental insights, nano-design paths can be improved to increase material performance, reduce cost and save resources by avoiding reverse engineering of battery materials.

As a matter of fact, novel materials, especially at the nanoscale, might show unknown behaviour when used in a battery. Every fundamental research has dead ends, and negative or unexpected results, slowing down the development progress. In order to turn these challenges efficiently into new insights instead, a conclusive cycle of material composite synthesis, determination of characteristic and most importantly, mechanistic study of material behaviour is required.

In-operando methods can visualise morphological, viscoelastic and conductivity changes of the electrode-electrolyte material in real time while applying electrochemical methods such as cyclic voltammetry and electrochemical impedance spectroscopy in three-electrode cells or constant current/potential battery cycling in two-electrode cells. In-operando measurements can be performed in air and in liquid. The latter is crucial to study charge

insertion mechanisms such as intercalation and pseudo-capacitive charge storage in liquid electrolytes. All in all, the understanding of mechanistic material behaviour enables the improved design of the mechanical material network, maintaining the integrity of both electric and ionic transport networks that facilitate the flows of ions and electrons.

The life time of a battery material can be studied *in-situ* depending on time and additional environmental influence factors like material reactivity, degradation, decomposition, corrosion, dendrite growth, formation of bio-films and passivating surface layers, which are also important, for instance, for predicting material recyclability.

One grand challenge in understanding material behaviour is the visualisation and traceability of active charge distribution and transport in electrodes/electrolytes. In particular, in composite electrodes for simplified battery designs, orchestrating ion/electron flows to facilitate battery operations. For instance, gel ionic liquid electrolytes incorporated into three-dimensional structured electrodes as composite or gel fibres woven together with fibre electrodes as composite sheets.

An interesting cross-section here are nature-inspired battery materials such as natural nano-fibres standing out for direct pathways for fast charge transport. Major aspects of new battery materials are the design, fabrication and perseverance of the interconnected electrical, ionic and mechanical networks to allow for simultaneous transport of ions and electrons through low-resistance and continuous networks to maximise the usable energy, power and capacity.

In-operando measurement data can be used to determine material boundaries leading to maximum theoretical battery performance values, which can only be accessed experimentally for certain materials. In-operando measurements also aim to support, extend or disprove theoretical models of material behaviour which are based on assumptions and limited experimental data. The experimental data can also be used to support the theoretical investigation of material behaviour using computational chemistry techniques such as density functional theory (DFT) modelling.

Conclusive Remarks:

I want to conclude that next generation batteries which fulfil all technical, social and environmental requirements will be based on new ideas and profound fundamental research, combining the research areas of electrochemistry, nanotechnology and materials science.

It is a fact that modern batteries will focus more on safe, smart and sustainable energy storage materials (3sESM) and their design might change completely. Electrode-electrolyte composites (EEC batteries), which turn all battery components from 2D into 3D, resulting in only one composite, is one promising approach to boost the battery's performance. Moreover, in-operando characterisation methods will become more popular as they have the ability to facilitate and accelerate material research and design.

However, it is questionable if those modern batteries will assert themselves beyond lithium-ion technologies without any trade-off in performance within the next 50 years as it is quite a mammoth task to reinvent the battery market. When it comes to sustainability, the responsibility does not come only with the manufacturers of technologies with batteries. The responsibility is also with society; the consumer. One half of the environmental impact is made by the battery production process, the other half by the consumer who sets the demand and recycles the battery device in the end. But what if society is given a choice? What if the consumer can decide which kind of battery he wants to use? What if there is an option to choose, a "green" battery option with safe and sustainable materials, but which might have to accept some trade-offs in performance? In the end, the consumer has the power to make a decision where he puts his money.

Even if there is no novel ground-breaking battery technology yet, and it is difficult to predict which one will emerge in reality, I like the direction we are heading.

8 Appendix

In this chapter, the script and video were published and reproduced with permission of The Royal Society of Chemistry [36].

8.1 Script of the Algorithm for the Calculation of the Shear Modulus

The following Mathematica®-notebook adapted according to [56] shows the algorithm for the calculation of the shear modulus presented in paragraph 5.3.1.4.1. Comments are described by „(* Comment *)“ and commands are ended by a semicolon („**;**“) if their output is suppressed. Built-in Mathematica-commands have the form „command[argument,…]“. The symbol („*****“) is neglected as every space between variables is interpreted as multiplication symbol. [36]

The script includes the following main steps:

- Definition of global constants
- Import of measured data
- Exclusion of data outliers
- Determination of quartz crystal parameter with measurement data of the unloaded quartz crystal in argon
- Determination of electrolyte parameter with measurement data of the loaded quartz crystal in the electrolyte
- Determination of the shear modulus for the polymerisation and cycling of PEDOT in monomer-free ionic liquid

```
(* start from scratch *)
Remove["Global`*"];
(* CONSTANTS *)
ρq=2.648; (* g/cm³ *)
μq= 2.957*10^11; (* g/cms² *)
```

```
Zq=Sqrt[ρq μq]; (* g/cm²s *)
K2=0.00774; (* 1 *)
L1=8.898659*10^-3; (* Vs/A = H *)
A=0.22135;(* cm² *)
F=96485.3; (*As/mol *)

(* you may want to change the following parameters *)
ηl=0.16; (* g/cms; [EMIm]AlCl4=0.16(16mPas)  *)
ρl=1.2985; (* g/cm³; [EMIm]AlCl4=1.2985 *)
ρf=1.334; (* PEDOT=1.334 g/cm³ *)

(* DATA FILES *)
wav=Import["C:\\WINDOWS\\Media\\notify.wav"];
SetDirectory["C:\\Users\\ts2n15\\Dropbox\\Promotion\\Experimental\\Measurements\\Ye
ar_2\\EQCM\\041918"];
fileIn0="0_Cal1.dat"; (* AIR DATA *)
fileIn1="1_Pol.dat"; (* LIQ/DEP DATA *)
fileIn2="2_Cycl1.dat"; (* CHAR. DATA *)
(* fileIn3 and fileIn4 are defined online *)

(* YOU MAY NEED TO CHANGE THE DEP START CRITERIA AND b-FACTOR RANGE IN THE
SECTIONS BELOW !!! *)
dims=-1 (* output dimensions for G: 0 dyn/cm² (calc.),-1 Pa, -5 N/cm^2 *);

If[dims===0, Gs="G' / dyn/cm²";Gl="G\" / dyn/cm²"];
If[dims===-1,Gs="G' / Pa";Gl="G\" / Pa"];
If[dims===-5,Gs="G' / N/cm²";Gl="G\" / N/cm²"];
(* 0. IN ARGON DATA CALCULATIONS *)
dataIn0=Import[fileIn0];
(* get first data row *)
j=1; While[j<= Length[dataIn0],
isComment=StringMatchQ[dataIn0[[j,1]],"time"];
```

```
j++;
If[isComment===True,Break[];]; ]

(* dataAir = { t/s, f/Hz, w/Hz Subscript[}, n] *)
(* ARRAY *) datat0=Table[dataIn0[[i,1]],{i,j,Length[dataIn0]}]
(* ARRAY *) dataf0=Table[dataIn0[[i,5]],{i,j,Length[dataIn0]}]
(* ARRAY *) dataw0=Table[dataIn0[[i,6]],{i,j,Length[dataIn0]}]
(* check for outliers *)
fInt=SetPrecision[Sort[{Median[dataf0]-
5MedianDeviation[dataf0],Median[dataf0]+5MedianDeviation[dataf0]}],10];
wInt=Sort[{Median[dataw0]-
5MedianDeviation[dataw0],Median[dataw0]+5MedianDeviation[dataw0]}];
For[i=1,i<=Length[datat0],i++,
If[fInt[[1]]<=dataf0[[i]]<=fInt[[2]] || wInt[[1]]<=dataw0[[i]]<=wInt[[2]],(*  do nothing *),
datat0=Delete[datat0,i];
dataf0=Delete[dataf0,i];
dataw0=Delete[dataw0,i];
i--; ]; ];

(* SKALAR *) f0=SetPrecision[Mean[dataf0],10];
(* SKALAR *) w0=Mean[dataw0];
{f0,w0}
(* SKALAR *) R1=2  π L1 w0 (* sH = sV/sA = Ω *)

(* GRAPHS *)
gfx01=ListPlot[Partition[Riffle[datat0,dataf0-dataf0[[1]]],2], PlotStyle->Blue,PlotRange->All];
gfx02=ListPlot[Partition[Riffle[datat0,dataw0-dataw0[[1]]],2], PlotStyle->Red];
Show[gfx01,gfx02, PlotRange->All, ImageSize->Small]

(* some clean up *)
ClearAll[j,i, isComment];
Remove[dataIn0,dataAir,"gfx0@"];
```

```
(* 1.a DEP DATA - LIQUID *)
dataIn1=Import[fileIn1];
(* get first data row *)
j=1; While[j<= Length[dataIn1],
isComment=StringMatchQ[dataIn1[[j,1]],"time"];
j++;
If[isComment===True,Break[];]; ]

(* ARRAY *) datat1=Table[dataIn1[[i,1]],{i,j,Length[dataIn1]}];
(* ARRAY *) dataE1=Table[dataIn1[[i,3]],{i,j,Length[dataIn1]}];
(* ARRAY *) dataf1=Table[dataIn1[[i,5]],{i,j,Length[dataIn1]}];
(* ARRAY *) dataw1=Table[dataIn1[[i,6]],{i,j,Length[dataIn1]}];

(* get first data point of electrochemistry, n - you may need to change the criteria *)
E0=0.0014; (* V *)
n=1; While[Abs[dataE1[[n]]-E0]<=0.01,n++]; n--;
n++
(* SKALAR *) R2s(* =Rs-R1 *)= 2  π L1 dataw1[[n]]-R1 (* Ω *)
(* SKALAR *) C0=Sqrt[(ρl ηl  π)/f0] 1/(8 Zq K2 R2s)  (* Sqrt[(g^2s)/(cm^4s)](cm^2sA)/gV = F
*)
(* SKALAR *) M=Nh/(8 K2 f0 C0) /.Nh->1 (* sV/As = Ω *)
(* SKALAR *) Xl=Sqrt[2 π f0 ρl ηl] (* Sqrt[1/s g/cm³ g/cms] = g/cm²s *)

ClearAll[j,isComment];
Remove[dataIn1,Nh];
0
1081.98
4.31948*10^-12
375626.
3604.64
dataw1[[n]]
19639.3
```

```
(* 1.b DEP DATA - FILM *)
(* ARRAY *) df0=dataf1-f0; (* 1/s *)
(* SKALAR *) fs=dataf1[[n]];
(* SKALAR *) ws=dataw1[[n]];
(* ARRAY *) dfs=dataf1-fs; (* 1/s *)
(* ARRAY *) dws=dataw1-ws; (* 1/s *)

(* ARRAY *) hfSB1=-(dfs/ρf) Zq/(2f0^2); (* cm *)
(* ARRAY *) Zfm=2 π f0 ρf hfSB1; (* 1/s g/cm³ cm = g/cm²s *)
(* ARRAY *) X2 (* =ω0L2 *)=-4 π L1 df0; (* H/s = Vs/As = Ω *)
(* ARRAY *) R2 (* =R-R1 *)= 2  π L1 dataw1-R1; (* Ω *)
(* SKALAR *) Xtr=Zq/M (-4 π L1 df0[[n]]-R2s) (* g/cm²s *)
(* ARRAY *) RE=Zq/M  R2/Xl;(* Ω/Ω(g/cm²s)/(g/cm²s) = 1 *)
(* ARRAY *) IM=(Zq/M X2/Xl-Xtr/Xl);(* Ω/Ω-(g/cm²s)/(g/cm²s) = 1 *)

(* GRAPHS *)
gfx1b1=ListLinePlot[Partition[Riffle[datat1,dfs],2],  AxesLabel->"df, dw",  PlotStyle-
>Red,ImageSize->Small,AxesOrigin->{0,0}];
gfx1b2=ListLinePlot[Partition[Riffle[datat1,dws],2],  AxesLabel->"dw", PlotStyle-
>Blue,ImageSize->Small,AxesOrigin->{0,0}];
gfx1b3=ListLinePlot[Partition[Riffle[datat1,Zfm],2], AxesLabel->"Zfm", PlotStyle-
>Black,ImageSize->Small,AxesOrigin->{0,0}];
gfx1b4=ListLinePlot[Partition[Riffle[datat1,R2],2],  AxesLabel->"R2, X2", PlotStyle-
>Red,ImageSize->Small,AxesOrigin->{0,0}];
gfx1b5=ListLinePlot[Partition[Riffle[datat1,X2],2],  AxesLabel->"X2", PlotStyle-
>Blue,ImageSize->Small,AxesOrigin->{0,0}];
gfx1b6=ListLinePlot[Partition[Riffle[datat1,RE],2],  AxesLabel->"RE, IM", PlotStyle-
>Red,ImageSize->Small, AxesOrigin->{0,0}];
gfx1b7=ListLinePlot[Partition[Riffle[datat1,IM],2],   AxesLabel->"IM", PlotStyle-
>Blue,ImageSize->Small,AxesOrigin->{0,0}];
```

```
GraphicsRow[{Show[gfx1b1,gfx1b2,PlotRange->All],gfx1b3, Show[gfx1b4,gfx1b5,PlotRange-
>All],Show[gfx1b6,gfx1b7,PlotRange->All]}]
-524.637

(* 1.c REVERSE SERIES FIT - b-MAXIMIZE *)
(* ARRAY *) dataG1={}; (* g/cms² = dyn/cm² = 10^5 N/cm² *)
(* ARRAY *) datab={}; (* b, stretch factor of hfSB, [b] = 1 *)
(* ARRAY *) bb={0.5,5.5}; (* range of b *)

Clear[dataGp]; dataGp={}; (* debug *)

(* SKALAR *) gs1=2800+400I; (* start value for FindRoot[] *)
fn1[g_]:=(Sqrt[I]+g/Xl Tanh[I ( b Zfm[[j]])/g])/(1+Sqrt[I] Xl/g Tanh[I ( b Zfm[[j]])/g])-(RE[[j]]+I
IM[[j]])

j=Length[datat1];While[j>=1,

run=1;While[run<=2,
(* Set b range *)
ClearAll[databb]; databb={}; (* helper array *)
If[run===1,
databb=Table[b,{b,bb[[1]],bb[[2]],0.05}],
databb=Table[b,{b,b1,b2,0.001}]; ];

(* Calculate g(b)-values *)
ClearAll[datagb];datagb={}; (* helper array *)
For[i=1,i<=Length[databb],i++,
rg1=Quiet[FindRoot[fn1[g] /.b->databb[[i]],{g,gs1}]];
AppendTo[datagb,g /.rg1]; ];

(* check for negatives and outliers *)
Glist=datagb^2/ρf;
```

```
(* For[i=1,i≤Length[databb],i++, (* remove negatives in pre-run only ... *)
If[run===1 && Re[Glist[[i]]]<0,   (* this may result in empty lists ... *)
databb=Delete[databb,i];              (* b1,b2 will then be the ones used previously *)
datagb=Delete[datagb,i];
Glist=Delete[Glist,i];
i--; ]; ]; *)

GInt=Quiet[Sort[{Median[Re[Glist]]-
5MedianDeviation[Re[Glist]],Median[Re[Glist]]+5MedianDeviation[Re[Glist]]}]];
(* For[i=1,i≤Length[databb],i++,
If[GInt[[1]]≤Re[Glist[[i]]]≤GInt[[2]] ,(*  do nothing *),
databb=Delete[databb,i];
datagb=Delete[datagb,i];
Glist=Delete[Glist,i];
i--; ]; ]; *)

(* Check for max G'(b) value *)
ClearAll[maxGp];
maxGp=Quiet[First[First[Position[Re[Glist],Max[Re[Glist]]]]]]; (* returns an index *)
(* gs1=datagb[[maxGp]]; ** results in scatter for fine run / start value issue *)
If[run===1,
AppendTo[dataGp,{maxGp,databb[maxGp],Length[Glist]}];
Which[bb[[1]]+0.1<databb[[maxGp]]<bb[[2]]-0.1,b1=databb[[maxGp]]-
0.1;b2=databb[[maxGp]]+0.1,
databb[[maxGp]]<=bb[[1]]+0.1,b1=bb[[1]];b2=bb[[1]]+0.2;,
databb[[maxGp]]>=bb[[2]]-0.1,b1=bb[[2]]-0.2;b2=bb[[2]];];
i++;,
(* else *)
G=Glist[[maxGp]];(* = gs1^2/ρf; ** see maxGp above *)
If[Re[G]>0&&Im[G]>0,AppendTo[dataG1,G];,AppendTo[dataG1,0];];
AppendTo[datab,databb[[maxGp]]];];
```

```
run++;];

(* store first and last g(b)-set for display *)
If[j===Length[datat1],databb2=databb;datagb2=datagb];
If[j===1,databb1=databb;datagb1=datagb];

j--;];
(* Fiting was done from end to start, thus: *)
dataG1=10^dims Reverse[dataG1];
datab=Reverse[datab];

(* get film properties *)
hf1=hfSB1 datab;
mf=A  ρf hf1;

(* GRAPHS *)
gfx1c1=ListLinePlot[Partition[Riffle[databb1,Re[datagb1^2/ρf]],2],AxesLabel-
>"G'(b)",PlotStyle->Green,ImageSize->Small,AxesOrigin->{bb[[1]],0}];
gfx1c2=ListLinePlot[Partition[Riffle[databb2,Re[datagb2^2/ρf]],2],PlotStyle->Red,ImageSize-
>Small];
gfx1c3=ListLinePlot[Partition[Riffle[datat1,datab],2],AxesLabel->"b",PlotStyle-
>Black,ImageSize->Small];
gfx1c4=ListLinePlot[Partition[Riffle[datat1,Re[dataG1]],2],AxesLabel->"G', G\"",PlotStyle-
>Red,ImageSize->Small];
gfx1c5=ListLinePlot[Partition[Riffle[datat1,Im[dataG1]],2],AxesLabel->"G\"",PlotStyle-
>Blue,ImageSize->Small];
GraphicsRow[{Show[gfx1c1,gfx1c2,PlotRange->{{bb[[1]],bb[[2]]},{-5
10^6,Automatic}}],gfx1c3,Show[gfx1c4,gfx1c5,PlotRange->{Automatic,{0,3*10^6}}]}]
(*
ClearAll[j,i,run,(**)E0,n,(**)Zfm,X2,R2,RE,IM,(**)gs1,rg1,maxGp,b,databb,databb1,databb2,
datagb,datagb1,datagb2,G,Glist,GInt,b1,b2];
Remove[dataE1,dataf1,dataw1,(**)df0,hfSB1,"gfx1@"]; *)
```

```
EmitSound[wav]

(* 1.d EXPORT RESULTS OF FITTING *)
fileOut=StringSplit[fileIn0,"."];
fileOut=fileOut[[1]]<>"_inf."<>fileOut[[2]];
tableOut={{"ηl",ηl},{"ρl",ρl},{"ρf",ρf},
{"f0",f0},{"w0",w0},
{"C0",C0},{"R1",R1},{"R2s",R2s},{"Xl",Xl},{"Xtr",Xtr},
{"fs",fs},{"ws",ws},{"b",bb}};
Export[fileOut,tableOut];
Remove[fileOut,tableOut];

fileOut=StringSplit[fileIn1,"."];
fileOut=fileOut[[1]]<>"_fit."<>fileOut[[2]];
tableHead={"df","dw","hf / m","b","mf / g",Gs,Gl};
tableOut=Table[{dfs[[i]],dws[[i]],hf1[[i]]/100,datab[[i]],mf[[i]],Re[dataG1[[i]]],Im[dataG1[[i]]]
},{i,1,Length[datat1]}];
tableOut=Prepend[tableOut,tableHead];
Export[fileOut,tableOut]
ClearAll[dfs,dws,hf1,mf,datab,dataG1];
Remove[fileOut,tableHead,tableOut,datat1];
1_Pol_fit.dat
ClearAll[i]
(* memory: *){ρq,μq,Zq,K2,L1,A,ηl,ρl,ρf,dims,(**) R2s,C0,M,Xl,Xtr,(**) fs,ws,(**)fn1,(**)
Gs,Gl, i};
?Global`*
 Global`

(* 2.a Cycling in monomer-free IL *)
(* !!! TROUBLE IN PARADISE if solvent (e.g. ρf and ηf) changes !!! *)
(* fileIn2="070110a01b.dat"; *)
dataIn2=Import[fileIn2];
```

```
(* get first data row *)
j=1; While[j<= Length[dataIn2],
isComment=StringMatchQ[dataIn2[[j,1]],"time"];
j++;
If[isComment===True,Break[];]; ]

(* ARRAY *) datat2=Table[dataIn2[[i,1]],{i,j,Length[dataIn2]}];
(* ARRAY *) dataE2=Table[dataIn2[[i,3]],{i,j,Length[dataIn2]}];
(* ARRAY *) dataf2=Table[dataIn2[[i,5]],{i,j,Length[dataIn2]}];
(* ARRAY *) dataw2=Table[dataIn2[[i,6]],{i,j,Length[dataIn2]}];

(* start evaluation right from the beginning - no n specification needed here *)
(* ARRAY *) dff0=dataf2-f0; (* 1/s *)
(* ARRAY *) dffs=dataf2-fs; (* 1/s *)
(* ARRAY *) dwfs=dataw2-ws ;(* 1/s *)

(* ARRAY *) hfSB2=-(dffs/ρf) Zq/(2f0^2); (* cm *)
(* ARRAY *) Zfm=2 π f0 ρf hfSB2 ;(* 1/s g/cm³ cm = g/cm²s *)
(* ARRAY *) X2 (* =ω0L2 *)=-4 π L1 dff0 ;(* H/s = Vs/As = Ω *)

(* ARRAY *) R2 (* =R-R1 *)= 2  π L1 dataw2-R1; (* Ω *)
(* ARRAY *) RE=Zq/M R2/Xl;(* Ω/Ω(g/cm²s)/(g/cm²s)=1 *)
(* ARRAY *) IM=(Zq/M 1/Xl (X2-Xtr));(* Ω/Ω-(g/cm²s)/(g/cm²s) = 1 *)

(* GRAPHS *)
gfx2a1=ListLinePlot[Partition[Riffle[datat2,dffs],2],  AxesLabel->"df, dw",  PlotStyle-
>Red,ImageSize->Small,AxesOrigin->{0,0}];
gfx2a2=ListLinePlot[Partition[Riffle[datat2,dwfs],2],  AxesLabel->"dw", PlotStyle-
>Blue,ImageSize->Small,AxesOrigin->{0,0}];
gfx2a3=ListLinePlot[Partition[Riffle[datat2,Zfm],2], AxesLabel->"Zfm", PlotStyle-
>Black,ImageSize->Small,AxesOrigin->{0,0}];
```

```
gfx2a4=ListLinePlot[Partition[Riffle[datat2,R2],2],  AxesLabel->"R2, X2", PlotStyle-
>Red,ImageSize->Small,AxesOrigin->{0,0}];
gfx2a5=ListLinePlot[Partition[Riffle[datat2,X2],2],  AxesLabel->"X2", PlotStyle-
>Blue,ImageSize->Small,AxesOrigin->{0,0}];
gfx2a6=ListLinePlot[Partition[Riffle[datat2,RE],2],  AxesLabel->"RE, IM", PlotStyle-
>Red,ImageSize->Small, AxesOrigin->{0,0}];
gfx2a7=ListLinePlot[Partition[Riffle[datat2,IM],2],   AxesLabel->"IM", PlotStyle-
>Blue,ImageSize->Small,AxesOrigin->{0,0}];
GraphicsGrid[{{Show[gfx2a1,gfx2a2,PlotRange->All],gfx2a3, Show[gfx2a4,gfx2a5,PlotRange-
>All],Show[gfx2a6,gfx2a7,PlotRange->All]}}]
ClearAll[j,isComment];
Remove[dataIn2];

(* 2.b REVERSE SERIES FIT - b-MAXIMIZE *)
(* ARRAY *) dataG1={};
(* ARRAY *) datab={};
(* ARRAY *)(* bb={0.5,1.5}; *)(* range of b *)

(* SKALAR *) gs1=2400+800I; (* start value for FindRoot[] *)

j=Length[datat2];While[j>=1,
run=1;While[run<=2,
(* Set b range *)
ClearAll[databb];
If[run===1,
databb=Table[b,{b,bb[[1]],bb[[2]],0.025}],
databb=Table[b,{b,b1,b2,0.001}]; ];

(* Calculate g(b)-values *)
ClearAll[datagb];datagb={};
For[i=1,i<=Length[databb],i++,
rg1=Quiet[FindRoot[fn1[g] /.b->databb[[i]],{g,gs1}]];
```

```
AppendTo[datagb,g /.rg1]; ];

(* check for outliers *)
Glist=datagb^2/ρf;
(* GInt=Sort[{Median[Re[Glist]]-
5MedianDeviation[Re[Glist]],Median[Re[Glist]]+5MedianDeviation[Re[Glist]]}];
For[i=1,i≤Length[databb],i++,
If[GInt[[1]]≤Re[Glist[[i]]]≤GInt[[2]],(*  do nothing *),
databb=Delete[databb,i];
datagb=Delete[datagb,i];
Glist=Delete[Glist,i];
i--; ]; ]; *)

(* Check for max G'(b) value *)
maxGp=First[First[Position[Re[Glist],Max[Re[Glist]]]]]; (* returns an index *)
(* gs1=datagb[[maxGp]]; ** results in scatter for fine run / start value issue *)

If[run===1,
Which[bb[[1]]+0.1<databb[[maxGp]]<bb[[2]]-0.1,b1=databb[[maxGp]]-
0.1;b2=databb[[maxGp]]+0.1,
databb[[maxGp]]<=bb[[1]]+0.1,b1=bb[[1]];b2=bb[[1]]+0.2;,
databb[[maxGp]]>=bb[[2]]-0.1,b1=bb[[2]]-0.2;b2=bb[[2]];];
i++;,
(* else *)
G=Glist[[maxGp]];(* = gs1^2/ρf; ** see maxGp above *)
If[Re[G]>0&&Im[G]>0,AppendTo[dataG1,G];,AppendTo[dataG1,0];];
AppendTo[datab,databb[[maxGp]]];];

run++;];

(* store first and last g(b)-set for display *)
If[j===Length[datat2],databb2=databb;datagb2=datagb];
```

```
If[j===1,databb1=databb;datagb1=datagb];

j--;];

(* Fiting was done from end to start, thus: *)
dataG1=10^dims Reverse[dataG1];
datab=Reverse[datab];

(* mass loss of the film [inserted mass] *)
hf2=hfSB2 datab;
mf=A  ρf hfSB2*datab;

(* GRAPHS *)
gfx2b1=ListLinePlot[Partition[Riffle[databb1,Re[datagb1^2/ρf]],2],AxesLabel-
>"G'(b)",PlotStyle->Green,ImageSize->Small];
gfx2b2=ListLinePlot[Partition[Riffle[databb2,Re[datagb2^2/ρf]],2],PlotStyle->Red,ImageSize-
>Small];
gfx2b3=ListLinePlot[Partition[Riffle[datat2,datab],2],AxesLabel->"b",PlotRange-
>{Automatic,{bb[[1]],bb[[2]]}},ImageSize->Small];
gfx2b4=ListLinePlot[Partition[Riffle[datat2,Re[dataG1]],2],AxesLabel->"G', G\"",PlotStyle-
>Red,ImageSize->Small];
gfx2b5=ListLinePlot[Partition[Riffle[datat2,Im[dataG1]],2],AxesLabel->"G\"",PlotStyle-
>Blue,ImageSize->Small];
GraphicsRow[{Show[gfx2b1,gfx2b2,PlotRange->All],gfx2b3,Show[gfx2b4,gfx2b5,PlotRange-
>Automatic]}]
(*ClearAll[j,i,run,(**)Zfm,X2,R2,RE,IM,(**)gs1,rg1,maxGp,b,databb,databb1,databb2,datagb,
datagb1,datagb2,G,Glist,GInt,b1,b2];
Remove[dataE2,dataf2,dataw2,(**)dff0,hfSB2,"gfx2@"]; *)
EmitSound[wav]

(* 2.c EXPORT RESULTS OF FITTING *)
fileOut=StringSplit[fileIn2,"."];
```

```
fileOut=fileOut[[1]]<>"_fit."<>fileOut[[2]];
tableHead={"df","dw","hf / m","b","mf / g",Gs,Gl};
tableOut=Table[{dffs[[i]],dwfs[[i]],hf2[[i]]/100,datab[[i]],mf[[i]]
,Re[dataG1[[i]]],Im[dataG1[[i]]]},{i,1,Length[datat2]}];
tableOut=Prepend[tableOut,tableHead];
Export[fileOut,tableOut]
(*ClearAll[dffs,dwfs,hf2,mf,datab,dataG1];*)
Remove[fileOut,tableHead,tableOut,datat2];
2_Cycl1_fit.dat
(* memory: *){ρq,μq,Zq,K2,L1,A,ηl,ρl,ρf,dims,(**)R2s,C0,M,Xl,(**) fs,ws,Xtr,(**)fn1,(**)
Gs,Gl};
?Global`*
```

8.2 In-Operando Atomic Force Microscopy Movie of PEDOT

A movie combining the AFM images of PEDOT in monomer-free Lewis EMImCl-$AlCl_3$ obtained at every step of the charge/discharge cycles (5.3.1.4.2) is available at the supplementary information material of DOI:10.1039/C8TA06757K. [36]

References

1. T. Schoetz, C. Ponce de Leon, A. Bund & M. Ueda. Preparation and characterization of a rechargeable battery based on poly-(3,4-ethylenedioxythiophene) and aluminum in ionic liquids. *Journal of Solid State Electrochemistry* **21,** 3237–3246 (2017).

2. T. Schoetz, C. Ponce de Leon, M. Ueda & A. Bund. State of the art of rechargeable aluminium batteries in non-aqueous systems. *Journal of the Electrochemical Society* **164,** A1–A4 (2017).

3. R. Korthauer. Handbook lithium-ion-batteries. *Springer-Verlag Berlin Heidelberg* (2013).

4. N. Nitta, F. Wu, J.T. Lee & G. Yushin. Li-ion battery materials: present and future. *Materials Today* **18,** 252–264 (2015).

5. B. Scrosati. Recent advances in lithium ion battery materials. *Electrochimica Acta* **45,** 2461–2466 (2000).

6. B. Scrosati & J. Garche. Lithium batteries: status, prospects and future. *Journal of Power Sources* **195,** 2419–2430 (2010).

7. J.W. Fergus. Recent developments in cathode materials for lithium ion batteries. *Journal of Power Sources* **195,** 939–954 (2010).

8. H.D. Yoo, E. Markevich, G. Salitra, D. Sharon & D. Aurbach. On the challenge of developing advanced technologies for electrochemical energy storage and conversion. *Materials Today* **17,** 110–121 (2014).

9. G.A. Elia, I. Hasa, G. Greco, T. Diemant, K. Marquardt, K. Hoeppner, R.J. Behm, A. Hoell, S. Passerini & R. Hahn. Insights into the reversibility of aluminum graphite batteries. *Journal of Materials Chemistry A* **5,** 9682–9690 (2017).

10. P.R. Gifford & J.B. Palmisano. An aluminum/chlorine rechargeable cell employing a room temperature molten salt electrolyte. *Journal of the Electrochemical Society* **135,** 650–654 (1988).

11. J.V. Rani, V. Kanakaiah, T. Dadmal, M. Srinivasa Rao & S. Bhavanarushi. Fluorinated natural graphite cathode for rechargeable ionic liquid based aluminium-ion battery. *Journal of the Electrochemical Society* **160,** A1781–A1784 (2013).

12. M.C. Lin, M. Gong, B. Lu, Y. Wu, D.Y. Wang, M. Guan, M. Angell, C. Chen, J. Yang, B.J. Hwang & H. Dai. An ultrafast rechargeable aluminium-ion battery. *Nature, Letter* **520,** 325–328 (2015).

13. K.V. Kravchyk, S. Wang, L. Piveteau & M.V. Kovalenko. Efficient aluminum chloride−natural graphite battery. *Chemistry of Materials* **29,** 4484–4492 (2017).

14. S. Ahmad, M. Deepa & S. Singh. Electrochemical synthesis and surface characterization of poly(3,4-ethylenedioxythiophene) films grown in an ionic liquid. *Langmuir* **23,** 11430–11433 (2007).

15. N. Jayaprakash, S.K. Das & L.A. Archer. The rechargeable aluminium-ion battery. *The Royal Society of Chemistry, Chemical Communications* **47,** 12610–12612 (2011).

16. W. Wang, B. Jiang, W. Xiong, H. Sun, Z. Lin, L. Hu, J. Tu, J. Hou, H. Zhu & S. Jiao. A new cathode material for super-valent battery based on aluminium ion intercalation and deintercalation. *Nature, Scientific Reports* **3,** 3–6 (2013).

17. L.D. Reed & E. Menke. The roles of V2O5 and stainless steel in rechargeable Al-ion batteries. *Journal of the Electrochemical Society* **160,** A915–A917 (2013).

18. M. Chiku, H. Takeda, S. Matsumura, E. Higuchi & H. Inoue. Amorphous vanadium oxide/carbon composite positive electrode for rechargeable aluminum battery. *ACS Applied Materials and Interfaces* **7,** 24385–24389 (2015).

19. H. Wang, Y. Bai, S. Chen, X. Luo, C. Wu, F. Wu, J. Lu & K. Amine. Binder-free V2O5 cathode for greener rechargeable aluminum battery. *ACS Applied Materials and Interfaces* **7,** 80–84 (2015).

20. T. Mori, Y. Orikasa, K. Nakanishi, C. Kezheng, M. Hattori, T. Ohta & Y. Uchimoto. Discharge/charge reaction mechanisms of FeS2 cathode material for aluminum rechargeable batteries at 55 °C. **313,** 9–14 (2016).

21. T. Gao, X. Li, X. Wang, J. Hu, F. Han, X. Fan, L. Suo, A.J. Pearse, S. Bok Lee, G.W. Rubloff, K.J. Gaskell, M. Noked & C. Wang. A rechargeable Al/S battery with an ionic-liquid electrolyte. *Angewandte Chemie* **128,** 10052–10055 (2016).

22. N.S. Hudak. Choroaluminate-doped conducting polymers as positive electrodes in rechargeable aluminium batteries. *The Journal of Physical Chemistry* **118,** 5203–5215 (2014).

23. J.N. Rauch. Global mapping of Al, Cu, Fe and Zn in-use stocks and in-ground resources. *U.S. Geological Survey; Reston VA* (2009).

24. R. Revel, T. Audichon & S. Gonzalez. Non-aqueous aluminium-air battery based on ionic liquid electrolyte. *Journal of Power Sources* **272,** 415–421 (2014).

25. E. Budevski, I. Iliev & A. Kaisheva. Investigations of a large-capacity medium-power saline aluminium-air battery. *Journal of Applied Electrochemistry* **19,** 323–330 (1989).

26. D. Egan, C. Ponce de Leon, R.J.K. Wood, R.L. Jones, K.R. Stokes & F.C. Walsh. Developments in electrode materials and electrolytes for aluminium-air batteries. *Journal of Power Sources* **236,** 293–310 (2013).

27. Q. Li & N.J. Bjerrum. Aluminium as anode for energy storage and conversion: a review. *Journal of Power Sources* **110,** 1–10 (2002).

28. W. Lu, A.G. Fadeev, B. Qi, E. Smela, B.R. Mattes, J. Ding, G.M. Spinks, J. Mazurkiewicz, D. Zhou, G.G. Wallace, D.R. MacFarlane, S.A. Forsyth & M. Forsyth. Use of ionic liquids for pi-conjugated polymer electrochemical devices. *Science* **297,** 983–987 (2002).

29. F. Endres & S.Z. El Abedin. Air and water stable ionic liquids in physical chemistry. *Physical Chemistry Chemical Physics* **8,** 2101–2116 (2006).

30. N.P. Stadie, S. Wang, K.V. Kravchyk & M.V. Kovalenko. Zeolite-templated carbon as an ordered microporous electrode for aluminum batteries. *ACS Nano* **11,** 1911–1919 (2017).

31. S. Choi, H. Go, G. Lee & Y. Tak. Electrochemical properties of an aluminum anode in an ionic liquid electrolyte for rechargeable aluminum-ion batteries. *Physical Chemistry Chemical Physics* **19,** 8653–8656 (2017).

32. L. Geng, G. Lv, X. Xing & J. Guo. Reversible electrochemical intercalation of aluminum in Mo6S8. *Chemistry of Materials* **27,** 4926–4929 (2015).

33. N. Koura, H. Ejiri & K. Takeishi. Polyaniline secondary cells with ambient temperature molten salt electrolyte. *Journal of the Electrochemical Society* **140,** 602–605 (1993).

34. J. Ding, D. Zhou & G. Wallace. Use of ionic liquids as electrolytes in electromechanical actuator systems based on inherently conducting polymers. *Chemistry of Materials* **15,** 2392–2398 (2003).

35. K. Wagner, J.M. Pringle, S.B. Hall, M. Forsyth, D.R. MacFarlane & D.L. Officer. Investigation of the electropolymerisation of EDOT in ionic liquids. *Synthetic Materials* **153,** 257–260 (2005).

36. T. Schoetz, M. Kurniawan, M. Stich, R. Peipmann, I. Efimov, A. Ispas, A. Bund, C. Ponce de Leon & M. Ueda. Understanding the charge storage mechanism of conductive polymers as hybrid battery-capacitor materials in ionic liquids by in-situ atomic force microscopy and

electrochemical quartz crystal microbalance studies. *Journal of Materials Chemistry A* **6,** 17787–17799 (2018).

37. Q.X. Liu, S. Zein El Abedin & F. Endres. Electroplating of mild steel by aluminium in a first generation ionic liquid: A green alternative to commercial Al-plating in organic solvents. *Surface and Coatings Technology* **201,** 1352–1356 (2006).

38. D. Pradhan & R.G. Reddy. Mechanistic study of Al electrodeposition from EMIC–AlCl3 and BMIC–AlCl3 electrolytes at low temperature. *Materials Chemistry and Physics* **143,** 564–569 (2014).

39. J.-J. Lee, I.T. Bae, D.A. Scherson, B. Miller & K.A. Wheeler. Underpotential Deposition of Aluminum and Alloy Formation on Polycrystalline Gold Electrodes from AlCl3 / EMIC Room-Temperature Molten Salts. *Journal of the Electrochemical Society* **147,** 562–566 (2000).

40. T. Jiang & M.J. Chollier Brym. Electrodeposition of aluminium from ionic liquids: Part I—electrodeposition and surface morphology of aluminium from aluminium chloride (AlCl3)–1-ethyl-3-methylimidazolium chloride ([EMIm]Cl) ionic liquids.

41. J.S. Wilkes, J.A. Levisky, R.A. Wilson & C.L. Hussey. Dialkylimidazolium chloroaluminate melts: a new class of room-temperature ionic liquids for electrochemistry, spectroscopy and synthesis. *Inorganic Chemistry* **21,** 1263–1264 (1982).

42. M. Ueda, S. Hariyama & T. Ohtsuka. Al electroplating on the AZ121 Mg alloy in an EMIC-AlCl3 ionic liquid containing ethylene glycol. *Journal of Solid State Electrochemistry* **16,** 3423–3427 (2012).

43. C. Peng, S. Zhang, D. Jewell & G.Z. Chen. Carbon nanotube and conducting polymer composites for supercapacitors. *Progress in Natural Science* **18,** 777–788 (2008).

44. G.A. Snook, P. Kao & A.S. Best. Conducting-polymer-based supercapacitor devices and electrodes. *Journal of Power Sources* **196,** 1–12 (2011).

45. T. Schoetz, C. Ponce de Leon, A. Bund & M. Ueda. Electro-polymerisation of 3,4-ethylenedioxythiophene on reticulated vitreous carbon in imidazolium-based chloroaluminate ionic liquid as energy storage material. *Electrochemistry Communications* **89,** 52–56 (2018).

46. J.H. Park & O.O. Park. Hybrid electrochemical capacitors based on polyaniline and activated carbon electrodes. *Journal of Power Sources* 185–190 (2002).

47. P. Damlin, C. Kvarnström & A. Ivaska. Electrochemical synthesis and in situ spectroelectrochemical characterization of poly(3,4-ethylenedioxythiophene) (PEDOT) in room temperature ionic liquids. *Journal of Electroanalytical Chemistry* **570,** 113–122 (2004).

48. T. Schoetz, C. Ponce de Leon, A. Bund & M. Ueda. Electro-polymerisation and characterisation of PEDOT in Lewis basic, neutral and acidic EMImCl-AlCl3 ionic liquid. *Electrochimica Acta* **263,** 176–183 (2018).

49. J. Heinze, B.A. Frontana-Uribe & S. Ludwigs. Electrochemistry of conducting polymers-persistent models and new concepts. *Chemical Reviews* 4724–4771 (2010).

50. S. Senthil Kumar, J. Mathiyarasu, K.L.N. Phani & V. Yegnaraman. Simultaneous determination of dopamine and ascorbic acid on poly (3,4-ethylenedioxythiophene) modified glassy carbon electrode. *Journal of Solid State Electrochemistry* **10,** 905–913 (2006).

51. J.L. Bredas & G.B. Street. Polarons, Bipolarons, and Solitons in Conducting Polymers. *Accounts of Chemical Research* **18,** 309–315 (1985).

52. D.P. Dubal, O. Ayyad, V. Ruiz & P. Gomez-Romero. Hybrid energy storage: the merging of battery and supercapacitor chemistries. *Chemical Society Reviews* **44,** 1777–1790 (2015).

53. T. Brousse, D. Belanger & J.W. Long. To Be or Not To Be Pseudocapacitive? *Journal of the Electrochemical Society* **162,** A5185–A5189 (2015).

54. B.E. Conway & W.G. Pell. Double-layer and pseudocapacitance types of electrochemical capacitors and their applications to the development of hybrid devices. *Journal of Solid State Electrochemistry* **7,** 637–644 (2003).

55. M.E. Abdelhamid, A.P. O'Mullane & G.A. Snook. Storing energy in plastics: a review on conducting polymers & their role in electrochemical energy storage. *RSC Advances* **5,** 11611–11626 (2015).

56. R. Peipmann. In situ Charakterisierung der viskoelastischen und elektrochemischen Eigenschaften von Poly(3,4-ethylendioxythiophen). *Dissertation* (2011).

57. L.T.T. Kim, C. Gabrielli, A. Pailleret & H. Perrot. Ions/Solvent Exchanges and Electromechanical Processes in Hexasulfonated Calix[6]Arene Doped Polypyrrole Films: Towards a Relaxation Mechanism. *Electrochemical and Solid-State Letters* **14,** F9–F11 (2011).

58. J.D. Holbrey & K.R. Seddon. Ionic liquids. *Clean Products and Processes* **1,** 223–236 (1999).

59. S.A. Forsyth, J.M. Pringle & D.R. MacFarlane. Ionic liquids-an overview. *Australian Journal of Chemistry* **57,** 113–119 (2004).

60. C. Dai, J. Zhang, C. Huang & Z. Lei. Ionic Liquids in Selective Oxidation: Catalysts and Solvents. *Chemical Reviews* **117,** 6929–6983 (2017).

61. P. Kubisa. Ionic Liquids in the Synthesis and Modification of Polymers. *Journal of Polymer Science: Part A: Polymer Chemistry* **43,** 4675–4683 (2005).

62. D.R. MacFarlane, N. Tachikawa, M. Forsyth, J.M. Pringle, P.C. Howlett, G.D. Elliott, J.H. Davis Jr., M. Watanabe, P. Simon & C. Austen Angell. Energy applications of ionic liquids. *Energy and Environmental Science* **7,** 232–250 (2014).

63. J.F. Wishart. Energy applications of ionic liquids. *Energy and Environmental Science* **2,** 956–961 (2009).

64. H. Ohno. Electrochemical aspects of ionic liquids. *John Wiley & Sons, Hoboken, New Jersey* (2005).

65. E.I. Izgorodina, Z. L. Seeger, D.L.A. Scarborough & S.Y.S. Tan. Quantum Chemical Methods for the Prediction of Energetic, Physical, and Spectroscopic Properties of Ionic Liquids. *Chemical Reviews* **117,** 6696–6754 (2017).

66. M.J. Earle & K.R. Seddon. Ionic liquids. Green solvents for the future. *Pure and Applied Chemistry* **72,** 1391–1398 (2000).

67. B. Wang, L. Qin, T. Mu, Z. Xue & G. Gao. Are Ionic Liquids Chemically Stable? *Chemical Reviews* **117,** 7113–7131 (2017).

68. T. Welton. Ionic liquids: a brief history. *Biophysical Reviews* **10,** 691–706 (2018).

69. J. Dupont. On the Solid, Liquid and Solution Structural Organization of Imidazolium Ionic Liquids. *Journal of the Brazilian Chemical Society* **15,** 341–350 (2004).

70. V. Strehmel, S. Berdzinski & H. Rexhausen. Interactions between ionic liquids and radicals. *Journal of Molecular Liquids* **192,** 153–170 (2014).

71. J. Le Bideau, L. Viau & A. Vioux. Ionogels, ionic liquid based hybrid materials. *Chemical Society Reviews* **40,** 907–925 (2011).

72. H. Tokuda, K. Hayamizu, K. Ishii, M.A.B.H. Susan & M. Watanabe. Physicochemical Properties and Structures of Room Temperature Ionic Liquids. 1. Variation of Anionic Species. *Journal of Physical Chemistry B* **108,** 16593–16600 (2004).

73. M. Armand, F. Endres & B. Scrosati. Ionic-liquid materials for the electrochemical challenges of the future. *Nature Materials* **8,** 621–629 (2009).

74. M. Galiński, A. Lewandowski & I. Stępniak. Ionic liquids as electrolytes. *Electrochimica Acta* **51,** 5567–5580 (2006).

75. K.R. Seddon. Ionic Liquids for Clean Technology. *Journal of Chemical Technology and Biotechnology* **68,** 351–356 (1997).

76. T. Tsuda, G.R. Stafford & C.L. Hussey. Review—Electrochemical Surface Finishing and Energy Storage Technology with Room-Temperature Haloaluminate Ionic Liquids and Mixtures. *Journal of the Electrochemical Society* **164,** H5007–H5017 (2017).

77. A.P. Abbott & K.J. McKenzie. Application of ionic liquids to the electrodeposition of metals. *Physical Chemistry Chemical Physics* **8,** 4265–4279 (2006).

78. A.A. Fannin Jr., D.A. Floreani, L.A. King, J.S. Landers, B.J. Piersma, D.J. Stech, R.L. Vaughn, J.S. Wilkes & J.L. Williams. Properties of 1,3-dialkylimidazolium chloride-aluminum chloride ionic liquids. 2. phase transitions, densities, electrical conductivities and viscosities. *Journal of Physical Chemistry* **12,** 2614–2621 (1984).

79. H.L. Bandey, S.J. Martin, R.W. Cernosek & A.R. Hillman. Modeling the responses of thickness-shear mode resonators under various loading conditions. *Analytical Chemistry* **71,** 2205–2214 (1999).

80. G. Sauerbrey. Verwendung von Schwingquarzen zur Wägung dünner Schichten und zur Mikrowägung. *Zeitschrift für Physik* **155,** 206–222 (1959).

81. S.J. Martin, H.L. Bandey, R.W. Cernosek, A.R. Hillman & M.J. Brown. Equivalent-circuit model for the thickness-shear mode resonator with a viscoelastic film near film resonance. *Analytical Chemistry* **72,** 141–149 (2000).

82. V. Edwards Granstaff & S.J. Martin. Characterization of a thickness-shear mode quartz resonator with multiple nonpiezoelectric layers. *Journal of Applied Physics* **75,** 1319–1329 (1994).

83. H.L. Bandey, A.R. Hillman, M.J. Brown & S.J. Martin. Viscoelastic characterization of electroactive polymer films at the electrode/solution interface. *Faraday Discussions* **107,** 105–121 (1997).

84. R. Lucklum, C. Behling, P. Hauptmann, R.W. Cernosek & S.J. Martin. Error analysis of material parameter determination with quartz-crystal resonators. *Sensors and Actuators A: Physical* **66,** 184–192 (1998).

85. A.R. Hillman, A. Jackson & S.J. Martin. The Problem of Uniqueness of Fit for Viscoelastic Films on Thickness-Shear Mode Resonator Surfaces. *Analytical Chemistry* **73,** 540–549 (2001).

86. E.J. Calvo & R. Etchenique. Viscoelastic Changes in Os-Containing Poly(allylamine) Based Redox Hydrogels for Amperometric Enzyme Electrodes: An EQCM Study. *Journal of Physical Chemistry B* **103,** 8944–8950 (1999).

87. A. Ispas, R. Peipmann, A. Bund & I. Efimov. On the p-doping of PEDOT layers in various ionic liquids studied by EQCM and acoustic impedance. *Electrochimica Acta* **54,** 4668–4675 (2009).

88. I. Efimov, A. Ispas & A. Bund. Taking into account of surface roughness for the calculation of elastic moduli of polymer films from acoustic impedance data. *Electrochimica Acta* **122,** 16–20 (2014).

89. V.-T. Gruia, A. Ispas, M. Wilke, I. Efimov & A.Bund. Application of acoustic impedance method to monitoring of sensors:Metal deposition on viscoelastic polymer substrate. *Electrochimica Acta* **118,** 88–91 (2014).

90. S. Koehler, A. Bund & I. Efimov. Shear moduli of anion and cation exchanging polypyrrole films. *Journal of Electroanalytical Chemistry* **589,** 82–86 (2006).

91. I. Efimov, S. Koehler & A.Bund. Temperature dependence of the complex shear modulus of cation and anion exchanging poly(pyrrole) films. *Journal of Electroanalytical Chemistry* **605,** 61–67 (2007).

92. A. Ispas, E. Wolff & A.Bund. An Electrochemical Quartz Crystal Microbalance Study on Electrodeposition of Aluminum and Aluminum-Manganese Alloys. *Journal of the Electrochemical Society* **164,** 5263–5270 (2017).

93. L. Daikhin, E. Gileadi, G. Katz, V. Tsionsky, M. Urbakh & D. Zagidulin. Influence of Roughness on the Admittance of the Quartz Crystal Microbalance Immersed in Liquids. *Analytical Chemistry* **74,** 554–561 (2002).

94. M. Urbakh & L. Daikhin. Roughness effect on the frequency of a quartz-crystal resonator in contact with a liquid. *Physical Review B* **49,** 4866–4870 (1994).

95. S. Wang, K.V. Kravchyk, F. Krumeich & M.V. Kovalenko. Kish Graphite Flakes as a Cathode Material for an Aluminum Chloride-Graphite Battery. *ACS Applied Materials and Interfaces* **9,** 28478–28485 (2017).

96. D.-Y. Wang, C.-Y. Wei, M.-C. Lin, C.-J. Pan, H.-L. Chou, H.-A. Chen, M. Gong, Y. Wu, C. Yuan, M. Angell, Y.-J. Hsieh, Y.-H. Chen, C.-Y. Wen, C.-W. Chen, B.-J. Hwang, C.-C. Chen & H. Dai. Advanced rechargeable aluminium ion battery with a high-quality natural graphite cathode. *Nature Communications* **8,** 14283 (2017).

97. J.M. Friedrich, C. Ponce de Leon, G.W. Reade & F.C. Walsh. Reticulated vitreous carbon as an electrode material. *Journal of Electroanalytical Chemistry* **561,** 203–217 (2004).

98. F.C. Walsh, L.F. Arenas, C. Ponce de Leon, G.W. Reade, I. Whyte & B.G. Mellor. The continued development of reticulated vitreous carbon as a versatile electrode material: Structure, properties and applications. *Electrochimica Acta* **215,** 566–591 (2016).

99. L. Janiszewska & R.A. Osteryoung. Electrochemistry of polythiophene and polybithiophene films in ambient temperature molten salts. *Journal of the Electrochemical Society* **134,** 2787–2794 (1987).

100. K. Liu, Z. Hu, R. Xue, J. Zhang & J. Zhu. Electropolymerization of high stable poly(3,4-ethylenedioxythiophene) in ionic liquids and its potential applications in electrochemical capacitor. *Journal of Power Sources* **179,** 858–862 (2008).

101. P. Wasserscheid & T. Welton. *Ionic liquids in synthesis*. **2,** (WILEY-VCH, 2008).

102. T. Jiang, M.J. Chollier Brym, G. Dubé, A. Lasia & G.M. Brisard. Electrodeposition of aluminium from ionic liquids: Part I—electrodeposition and surface morphology of aluminium from aluminium chloride (AlCl3)–1-ethyl-3-methylimidazolium chloride ([EMIm]Cl) ionic liquids. *Surface and Coatings Technology* **201,** 1–9 (2006).

103. F. Endres. Ionic Liquids: solvents for the electrodeposition of metals and semiconductors. *Journal of Chemical Physics and Physical Chemistry* **3,** 144–154 (2002).

104. R. Van Noorden. A better battery. *Nature* **507,** 26–28 (2014).

105. M. Armand & J. Tarascon. Building better batteries. *Nature* **451,** 652–657 (2008).

106. C.P. Grey & J.M. Tarascon. Sustainability and in situ monitoring in battery development. *Nature Materials* **16,** 45–56 (2017).

107. D.W. Murphy & P.A. Christian. Solid State Electrodes for High Energy Batteries. *Science* **205,** 651–656 (1979).

108. E. Serrano, G. Rus & J. Garcia-Martinez. Nanotechnology for sustainable energy. *Renewable and Sustainable Energy Reviews* **13,** 2373–2384 (2009).

109. C. Liu, E.I. Gillette, X. Chen, A.J. Pearse, A.C. Kozen, M.A. Schroeder, K.E. Gregorczyk, S.B. Lee & G.W. Rubloff. An all-in-one nanopore battery array. *Nature Nanotechnology* **9,** 1031–1039 (2014).

110. B. Scrosati. Paper powers battery breakthrough. *Nature Nanotechnology* **2,** 598–599 (2007).

111. K. Takada. Progress and prospective of solid-state lithium batteries. *Acta Materialia* **61,** 759–770 (2013).

112. P.H.L. Notten, F. Roozeboom, R.A.H. Niessen & L. Baggetto. 3-D Integrated All-Solid-State Rechargeable Batteries. *Advanced Materials* **19,** 4564–4567 (2007).

113. L. Baggetto, R.A.H. Niessen, F. Roozeboom & P.H.L. Notten. High Energy Density All-Solid-State Batteries: A ChallengingConcept Towards 3D Integration. *Advanced Functional Materials* **18,** 1057–1066 (2008).

114. J.G. Werner, G.G. Rodriguez-Calero, H.D. Abruna & U. Wiesner. Block copolymer derived 3-D interpenetrating multifunctional gyroidal nanohybrids for electrical energy storage. *Energy and Environmental Science* **11,** 1261–1270 (2018).

115. D. Wei. Electrochemical Nanofabrication. *Pan Stanford Publishing* **2,** (2016).

116. V. Kirchner, X. Xia & R. Schuster. Electrochemical Nanostructuring with Ultrashort Voltage Pulses. *Accounts of Chemical Research* **34,** 371–377 (2001).

117. P.L. Schilardi, P. Dip, P.C. dos Santos Claro, G.A. Benitez, M.H. Fonticelli, O. Azzaroni & R.C. Salvarezza. Electrochemical Deposition onto Self-Assembled Monolayers: New Insights into Micro- and Nanofabrication. *Chemistry A European Journal* **12,** (2006).

118. S.-W. Kim, T.H. Han, J. Kim, H. Gwon, H.-S. Moon, S.-W. Kang, S.O. Kim & K. Kang. Fabrication and Electrochemical Characterization of TiO2 Three- Dimensional Nanonetwork Based on Peptide Assembly. *ACS Nano* **3,** 1085–1090 (2009).

119. D.B. Allred, M. Sarikaya, F. Baneyx & D.T. Schwartz. Bacterial surface-layer proteins for electrochemical nanofabrication. *Electrochimica Acta* **53,** 193–199 (2007).

120. E. Tamburri, F. Toschi, V. Guglielmotti, E. Scatena, S. Orlanducci & M.L. Terranova. Nanofabrication by electrochemical routes of Ni-coated ordered arrays of carbon nanotubes. *Journal of Nanoparticle Research* **11,** 1311–1319 (2009).

121. A.P. Suryavanshi & M.-F. Yu. Electrochemical fountain pen nanofabrication of vertically grown platinum nanowires. *Nanotechnology* **18,** 105305 (2007).

List of Figures

Figure 1: Specific power and energy of state-of-the-art rechargeable batteries vanadium-redox-flow (V-redox-flow), lead-acid (Pb-acid), cadmium-nickel (Cd-Ni), nickel-metal-hydride (Ni-metal-hydride) and lithium-ion (Li-ion) batteries in relation to sustainability [3]. [2] 2

Figure 2: Schematic illustration of a rechargeable aluminium-conductive polymer battery with chloroaluminate ionic liquid electrolyte. adapted from [1] 10

Figure 3: Structure of poly-(3,4-ethylenedioxythiophene) (PEDOT) with highlighted monomer unit 3,4-ethylenedioxythiophene (EDOT). 12

Figure 4: Illustration of two PEDOT chains (A) in the uncharged state, (B) during charging/oxidation and (C) in a fully charged state. The interchain distance x increases during charging of PEDOT (faradaic charge transfer) and insertion of anions (non-faradaic charge transfer). 14

Figure 5: Structure of the cation $EMIm^+$ and the anions $Al_2Cl_7^-$, $AlCl_4^-$ and Cl^-. 16

Figure 6: (A) Synthesis of EMImCl-$AlCl_3$ ionic liquid in a cooling bath. (B) Resulting Lewis basic, neutral and acidic solution. (C) Addition of 0.1 mol dm^{-3} EDOT and resulting Lewis basic, neutral and acidic solutions for electropolymerisation. [48] 20

Figure 7: Schematic illustration of the experimental set-up of the quartz crystal microbalance adapted from [56]. [36] 23

Figure 8: Schematic illustration of a cross-section of a rough and planar polymer film in fluid adapted from [56]. 25

Figure 9: (A) Illustration of the complex shear modulus G*and (B) real G' (red) and imaginary G'' (blue) part depending on the correction factor b adapted from [56] 27

Figure 10: Schematic illustration of the in-operando AFM cell with PEDOT on vitreous carbon covered in Lewis neutral EMImCl-$AlCl_3$ ionic liquid. [36] 28

Figure 11: Schematic illustration of the battery test cell. 31

Figure 12: Schematic illustration of an aluminium-PEDOT battery with a gradient in Lewis acidity of the chloroaluminate ionic liquid. 32

Figure 13: SEM images of (A) aluminium electrode surface after ~20 charge/discharge cycles in Lewis acidic EMImCl-$AlCl_3$, (B) porous glass electrolyte support in the dry state and (C) PEDOT electropolymerised at 1.2 V vs. Ag/AgCl for 30 min on planar vitreous carbon in 0.01 mol dm^{-3} EDOT and 0.1 mol dm^{-3} KCl aqueous solution. [adapted from 1] 37

Figure 14: Stability potential windows of monomer-free Lewis acidic, neutral and basic EMImCl-$AlCl_3$ at 25 °C with vitreous carbon as working and counter electrode and aluminium as a reference electrode. 39

Figure 15: Cyclic voltammograms of a monomer-free Lewis acidic (dashed line, cycle 15) and with 0.1 mol dm^{-3} EDOT (solid line, cycle 15) EMImCl-$AlCl_3$ ionic liquid at 100 mV s^{-1} and 25 °C. [48] 40

Figure 16 Cyclic voltammograms of a monomer-free Lewis basic (dashed line, cycle 3) and with 0.1 mol dm^{-3} EDOT (solid line, cycle 3) EMImCl-$AlCl_3$ ionic liquid at 100 mVs^{-1} and 25 °C. [48].....42

Figure 17: Cyclic voltammograms of a monomer-free Lewis neutral (inset CV, cycle 3) and with 0.1 mol dm^{-3} EDOT (main CV, 20 cycles) EMImCl-$AlCl_3$ ionic liquid at 100 mVs^{-1} and 25 °C. [48] 43

Figure 18: SEM images of PEDOT surfaces at (A-C) increasing magnification obtained in Lewis neutral EMImCl-$AlCl_3$ with 0.1 mol dm^{-3} EDOT from -0.5 V to 2.6 V vs. Al|Al(III) at 100 mV s^{-1}, 20 cycles and 25 °C. [adapted from 48] 44

Figure 19: Schematic illustration of the three-dimensional RVC-PEDOT composite with inserting $AlCl_4^-$ ions of a Lewis neutral chloroaluminate ionic liquid. [adapted from 45] 45

Figure 20: SEM images of PEDOT on reticulated vitreous carbon after electropolymerisation over 200 pulses in Lewis neutral EMImCl-$AlCl_3$ containing 0.1 mol dm^{-3} EDOT by RNPV (A) top view, (B) cross-sectional view and by DPA (C) cross-sectional view lower part RVC substrate and (D) zoom on polymerised edge of the RVC backbone. [45] 46

Figure 21: SEM images of (A) bare reticulated vitreous carbon, (B) and (C) PEDOT on reticulated vitreous carbon surface, (D) and (E) cross-sectional area after electropolymerisation by cyclic voltammetry in Lewis neutral EMImCl-$AlCl_3$ containing 0.1 mol dm^{-3} EDOT and (F-H) after 250 cycles in monomer-free Lewis neutral EMImCl-$AlCl_3$. [45] .47

Figure 22: Cyclic voltammograms of PEDOT films in monomer-free Lewis (A) acidic (cycle 7), (B) neutral (cycle 15) and (C) basic (cycle 7) EMImCl-$AlCl_3$ at 100 mV s^{-1} and 25 °C. [48] 49

Figure 23: Cyclic voltammograms of PEDOT films polymerised from -0.5 V to (A) 1.5 V, (B) 2.0 V and (C) 2.6 V vs. Al|Al(III) in Lewis neutral EMImCl-$AlCl_3$ with 0.1 mol dm^{-3} EDOT at 20 cycles. Cyclic voltammograms of PEDOT films polymerised to (D) 1.5 V, cycle 15, (E) 2.0 V, cycle 7 and (F) 2.6 V, cycle 15 in monomer-free Lewis neutral EMImCl-$AlCl_3$ from -0.5 V to 2.6 V vs. Al|Al(III) at 100 mV s^{-1} and 25 °C. [adapted from 48] 52

Figure 24: SEM images of PEDOT surfaces at (A,B,C) 1000-fold and (D,E,F) 5000-fold magnification obtained in Lewis neutral EMImCl-$AlCl_3$ with 0.1 mol dm^{-3} EDOT from -0.5 V to (A,D) 1.5 V, (B,E) 2.0 V and (C,F) 2.6 V vs. Al|Al(III) at 100 mV s^{-1}, 20 cycles and 25 °C. [48] 54

Figure 25: Cyclic voltammogram of a PEDOT film on a 0.8 cm^2 area vitreous carbon disc, from 0 V to 2.5 V vs. Al|Al(III) at 100 mV s^{-1}. Cycles: 2nd (black line), 100th (red line), 200th (blue line), 300th (violet line), 400th (green line) and 500th (orange line) cycle in monomer-free Lewis neutral EMImCl-$AlCl_3$. The PEDOT film was previously polymerised in Lewis neutral EMImCl-$AlCl_3$ containing 0.1 mol dm^{-3} EDOT from -0.5 V to 2.5 V vs. Al|Al(IIII) at 100 mV s^{-1}, during 20 cycles and 25 °C. [45].....55

Figure 26: Cyclic voltammogram of PEDOT films from 0 V to 2.5 V vs. Al|Al(III) with 100 mV s^{-1} at 2nd cycle and 25 °C in monomer-free Lewis neutral EMImCl-$AlCl_3$. PEDOT films polymerised on planar vitreous carbon (VC) by cyclic voltammetry (solid line) and on reticulated vitreous carbon (RVC) by cyclic voltammetry (dashed line). [45].....56

Figure 27: (A) Frequency (black line) and damping (red line) change of a gold-coated quartz crystal, (B) calculated shear modulus (real part), (C) polymer film thickness (black line) and mass (red line) and (D) correction factor during the cycling of PEDOT in monomer-free Lewis neutral EMImCl-$AlCl_3$ from 0 V to 2.5 V vs. Al|Al(III), 100 mV s^{-1}, 25 °C. [36].....58

Figure 28: (A) Cyclic voltammogram, (B) frequency change of a gold-coated quartz crystal, (C) calculated shear modulus (real part) of the polymer film during charging (a; black lines) and discharging (b; red lines) of PEDOT in monomer-free Lewis neutral EMImCl-$AlCl_3$ from 0 V to 2.5 V vs. Al|Al(III) at cycle 10, 100 mV s^{-1} at 25 °C. [36] 61

Figure 29: Initial state AFM image of uncharged PEDOT in monomer-free Lewis neutral EMImCl-$AlCl_3$. PEDOT was polymerised by CV from -0.5 V to 2.5 V vs. Al|Al(III) in Lewis neutral EMImCl-$AlCl_3$ with 0.1 mol dm^{-3} EDOT at 100 mV s^{-1}, 20 cycles and 25 °C. [36] 62

Figure 30: AFM images showing differences in (A) height and (B) deformability of uncharged PEDOT in monomer-free Lewis neutral EMImCl-$AlCl_3$. [36] 63

Figure 31: AFM images at different states of charge (A-E) and discharge (F-J). The squared areas (a-d) show morphological surface changes of the PEDOT in detail. [36] 64

Figure 32: Nyquist plots with increasing magnification from (A) to (D) of PEDOT in monomer-free Lewis neutral EMImCl-$AlCl_3$ depending on the state of charge from 0 V to 2.5 V vs. Al|Al(III) at a frequency range from 1 mHz to 500 kHz and 25 °C. 66

Figure 33: 3D Bode plots of PEDOT in monomer-free Lewis neutral EMImCl-$AlCl_3$ depending on the state of charge from 0 V to 2.5 V vs. Al|Al(III) at a frequency range from 1 mHz to 1 MHz and 25 °C. 67

Figure 34: AFM images of PEDOT in monomer-free Lewis neutral EMImCl-$AlCl_3$ in the fully (A) charged and (B) discharged state and (C) schematic model of the morphological changes of a conductive polymer in ionic liquid during charging (oxidation, anion insertion) and discharging (reduction, anion removal). [adapted from 36] 70

Figure 35: Cyclic voltammogram of the aluminium deposition and dissolution on vitreous carbon in Lewis acidic EMImCl-$AlCl_3$ ionic liquid at cycle 3, 100 mV s^{-1} and 25 °C. 72

Figure 36: In-operando AFM images of the aluminium deposition on (A) bare vitreous carbon at (B) -0.2 V, (C) -0.4 V, (D) -0.5 V, (E) -0.6 V and (F) -1.0 V vs. Al|Al(III) in Lewis acidic EMImCl-$AlCl_3$ at 25 °C. The white rectangles indicate the same position on the surface. 73

Figure 37: Changes in colour of EMImCl-$AlCl_3$ from Lewis neutral to ultra-acidic. (A) 50 mol-%:50 mol-% (neutral), (B) 45 mol-%:55 mol-%, (C) 40 mol-%:60 mol-%, (D) 35 mol-%:65 mol-% (acidic) and (E) 30 mol-%:70 mol-% (ultra-acidic). 74

Figure 38: Cyclic voltammograms of the aluminium deposition and dissolution on vitreous carbon in EMImCl-$AlCl_3$ (black line; a) 50 mol-%:50 mol-% (neutral), (red line; b) 45 mol-%: 55 mol-%, (green line; c) 40 mol-%:60 mol-%, (blue line; d) 35 mol-%:65 mol-% (acidic) and (pink line; e) 30 mol-%:70 mol-% (ultra-acidic) at cycle 3, 100 mV s^{-1} and 25 °C. 75

Figure 39: SEM images of (A) bare aluminium surface and aluminium deposit obtained at -1.0 mA for 30 min at 25 °C in EMImCl-$AlCl_3$ (B) 50 mol-%:50 mol-% (neutral), (C) 45 mol-%:55 mol-%, (D) 40 mol-%:60 mol-%, (E) 35 mol-%:65 mol-% (acidic) and (F) 30 mol-%:70 mol-% (ultra-acidic). 76

Figure 40: Characteristic charge and discharge cycle of an aluminium-PEDOT battery charged at 0.1 mA (0.8C) until 2.2 V and discharged at -0.1 mA (0.8C) until 0.5 V at 25 °C. 77

Figure 41: Charge and discharge curves of an aluminium-PEDOT battery charged at 0.1 mA (0.8C, black line), 0.5 mA (4C, red line), 1.0 mA (8C, green line), 5.0 mA (40C, blue line) and 10 mA (80C, pink line) until 2.2 V, held at a constant potential of 2.2 V until 0.15 mA (end of charge marked by arrows) and discharged at -0.1 mA (0.8C) until 0.5 V at 25 °C. 79

Figure 42: Charge and discharge curves of an aluminium-PEDOT battery charged at 1.0 mA (8C) (until 2.2 V, held at a constant potential of 2.2 V until 0.15 mA and discharged at -0.1 mA (0.8), -0.5 mA (4C) and -1.0 mA (8C) until 0.5 V at 25 °C. 80

Figure 43: Coulombic efficiency of the charge and discharge reaction of an aluminium-PEDOT battery depending on the cycle number at 25 °C. Battery charged at 0.1 mA (0.8C) until 2.2 V and discharged at -0.1 mA (0.8C) until 0.5 V at 25 °C. 81

Figure 44: PEDOT: SEM images of (A) bare RVC. (B) PEDOT on RVC, before battery cycling. (C) PEDOT on RVC, after battery cycling (charge CCCV: 1 mA (8C) until 2.2 V, 2.2 V until 0.15 mA; discharge CC -0.1 mA (0.8C) until 0.5 V) for 100 cycles. 82

Figure 45: SEM images of (A) pure aluminium surface before and (B-D) after battery cycling (charge CCCV: 1 mA (8C) until 2.2 V, 2.2 V until 0.15 mA; discharge CC -0.1 mA (0.8C) until 0.5 V; 100 cycles) with aluminium deposit. 83

Figure 46: Cyclic voltammograms of Lewis neutral EMImCl-$AlCl_3$ liquid (blue curve, c) and ionogel (black, b and red, a curve) with vitreous carbon as working and counter electrode and aluminium as reference electrode at 100 mV s^{-1} and 25 °C. The inset photo shows synthesised Lewis neutral ionogel. 87

Figure 47: Redesign of today's conventional battery architecture to efficient EEC-batteries in the future. The drawings are adapted and reproduced with permission of The Royal Society of Chemistry [114]. 94

List of Tables

Table 1: Battery components (positive/negative electrodes and electrolyte) and characteristic battery values (measured average cell potential E, specific capacity Q_{spec} and energy E_{spec}) for rechargeable aluminium batteries with a charge-storage material as positive electrode. [2] 5

Table 2: Molar ratio χ and mass m of EMImCl to $AlCl_3$ for 25 mL EMImCl-$AlCl_3$ ionic liquids with different Lewis acidity and dominant anion species, respectively [64]. [48].....18

Table 3: Density of EMImCl-$AlCl_3$ ionic liquid mixture ρ depending on the acidity at 30 °C [78]. [48] 19

Table 4: Comparison of charge/discharge capacity Q_{charge} and $Q_{discharge}$, specific energy E_{spec} and power P_{spec} of the initial aluminium-PEDOT battery in Lewis acidic EMImCl-$AlCl_3$ with and without electrolyte support. [1] 37

Table 5: Calculated active mass m_a, specific capacity Q_{spec}, energy E_{spec} and power P_{spec} for an aluminium-PEDOT battery at a charge and discharge rate of ± 0.1 mA (0.8C) (Figure 40).....84